12-2016

Microstructural evolution during the homogenization heat treatment of 6XXX and 7XXX aluminum alloys

Pikee Priya
Purdue University

Graduate School Form
30 Updated 12/26/2015

PURDUE UNIVERSITY
GRADUATE SCHOOL
Thesis/Dissertation Acceptance

This is to certify that the thesis/dissertation prepared

By PIKEE PRIYA

Entitled

MICROSTRUCTURAL EVOLUTION DURING THE HOMOGENIZATION HEAT TREATMENT OF 6XXX AND 7XXX ALUMINUM ALLOYS

For the degree of Doctor of Philosophy

Is approved by the final examining committee:

DAVID R. JOHNSON
Co-chair

MATTHEW J. M. KRANE
Co-chair

KEVIN P. TRUMBLE

MYSORE A. DAYANANDA

To the best of my knowledge and as understood by the student in the Thesis/Dissertation Agreement, Publication Delay, and Certification Disclaimer (Graduate School Form 32), this thesis/dissertation adheres to the provisions of Purdue University's "Policy of Integrity in Research" and the use of copyright material.

Approved by Major Professor(s): DAVID JOHNSON

Approved by: DAVID BAHR 10/11/2016

Head of the Departmental Graduate Program Date

MICROSTRUCTURAL EVOLUTION DURING THE HOMOGENIZATION HEAT TREATMENT OF 6XXX AND 7XXX ALUMINUM ALLOYS

A Dissertation

Submitted to the Faculty

of

Purdue University

by

Pikee Priya

In Partial Fulfillment of the

Requirements for the Degree

of

Doctor of Philosophy

December 2016

Purdue University

West Lafayette, Indiana

Dedicated to my family.

ACKNOWLEDGEMENTS

I, first acknowledge the support of my family members and my husband, Debashish, which made my graduate life a memorable and enjoyable experience. I thank my advisors, Prof. Matthew Krane and Prof. David Johnson, for supervising this work and having an unshakable belief in me, even though there were setbacks. I acknowledge, contributions to this research work from my committee members, Prof. Kevin Trumble and Prof. Mysore Dayananda.

My experiments in MSE labs would not have been possible without instructional and technical support from Patricia Metcalf, David Meyer, Jameson Root and Tim Vanmeter. I also thank Gamini Mendis for helping me with the Differential Scanning Calorimetry.

I gratefully acknowledge financial support from Shandong Nanshan Aluminum Co., Beijing Nanshan Institute of Aeronautical Materials for this research work.

Finally, I thank Sailei Zhang, whose previous contributions and discussions helped in the work. I thank Yiwei Sun, for her experiments which helped me validate my numerical results. I also thank Jeff Yanke, Alex Plotkowski, Kyle Fezi, Daniel Klenosky and John Coleman who were always available for discussions and made the lab an enjoyable place to work in.

TABLE OF CONTENTS

Page

Page

Page

Page

LIST OF TABLES

Table Page

Appendix Table Page

LIST OF FIGURES

Figure Page

Figure Page

Figure Page

Figure Page

Figure Page

LIST OF SYMBOLS

Latin Symbols

A	Aspect ratio
A_{eq}	Aspect ratio at nucleation
c_p	Specific heat capacity
$\bar{C}$	Mean composition of the matrix
C_e	Equilibrium composition of the matrix
C^i	Composition of component i
C_i^k	Composition of component k in phase i
C_{ij}^k	Composition of component k in phase i in the jth neighbor
C_i^{k*}	Equilibrium composition of component k in phase i
D_0	Diffusion constant
D_i	Diffusion coefficient of component i
D_{ij}^k	Diffusion coefficient of component i due to composition gradient of j in k
f_i	Mass fraction of phase i
Δf_i	Change in mass fraction of phase i
$\Delta f_{i/j}$	Change in mass fraction of phase i to phase j
ΔG	Driving force for nucleation
ΔG_{df}	Driving force for phase transformation
ΔG_{diff}	Free energy dissipated in diffusional processes
ΔG_{fric}	Free energy dissipated in overcoming interfacial friction
ΔG_N	Mean driving force for nucleation
ΔG_σ	Standard deviation of driving force for nucleation
h	Heat transfer coefficient
$\overline{H'}$	Mean projected area of a precipitate

Latin symbols

j_0	Nucleation rate pre-factor
j^j	Nucleation rate for jth phase
k_B	Boltzmann constant
k_c	Thermal conductivity
M	Mobility
M_0	Mobility constant
N	Number of nucleation sites
N_A	Number of precipitates per unit area
N_{Av}	Avagadro number
N^j	Number of precipitates of phase j
N_{max}	Maximum number of nucleation sites
N_{tot}	Total number of precipitates
N_V	Number of precipitates per unit volume
$(N_A)_i$	Number of precipitates per unit area for the ith size class
$(N_V)_i$	Number of precipitates per unit volume for the ith size class
P_Z	Zener pressure
Q_d	Activation energy for diffusion
Q_m	Activation energy for interface mobility
r	Radius, radial co-ordinate
r_c	Critical radius of the nuclei
R_0	Radius of the billet
t	Time
t_f	Local solidification time
Δt	Time step
v	Velocity of the precipitate/matrix interface
v^j	Velocity of the jth phase/matrix interface
$v_{i/j}$	Velocity of the ith and jth phase interface
V_i	Molar volume of ith precipitate phase
x_i	Molar composition of component i

Latin symbols

x_j^i	Molar composition of component i in phase j
Δx	Grid size in x-direction
$y(i)$	y-height for the ith column
Z	Zeldovich constant

Greek symbols

α_i	Weighing constant for bin class i
Δ	Bin size
ε	Emissivity
γ	Interfacial energy
γ^j	Interfacial energy of phase j with the matrix
κ	Curvature
λ_2	Secondary dendrite arm spacing
σ	Stefan-Boltzmann constant
θ	Wetting angle

Subscripts and superscripts

het	Pertaining to heterogeneous nucleation
hom	Pertaining to homogeneous nucleation
m	Matrix
$neighbor$	Neighboring cells
new	In current time step
old	In previous time step
p	Precipitate
∞	Position distant from the precipitate/matrix interface

ABSTRACT

Priya, Pikee. Ph.D., Purdue University, December 2016. Microstructural Evolution during Homogenization Heat Treatment of 6XXX and 7XXX Aluminum Alloys. Major Professors: Matthew John M. Krane and David R. Johnson

Homogenization heat treatment of as-cast billets is an important step in the processing of aluminum extrusions. Microstructural evolution during homogenization involves elimination of the eutectic morphology by spheroidisation of the interdendritic phases, minimization of the microsegregation across the grains through diffusion, dissolution of the low-melting phases, which enhances the surface finish of the extrusions, and precipitation of nano-sized dispersoids (for Cr-, Zr-, Mn-, Sc-containing alloys), which inhibit grain boundary motion to prevent recrystallization. Post-homogenization cooling reprecipitates some of the phases, changing the flow stress required for subsequent extrusion. These precipitates, however, are deleterious for the mechanical properties of the alloy and also hamper the age-hardenability and are hence dissolved during solution heat treatment.

Microstructural development during homogenization and subsequent cooling occurs both at the length scale of the Secondary Dendrite Arm Spacing (SDAS) in micrometers and dispersoids in nanometers. Numerical tools to simulate microstructural development at both the length scales have been developed and validated against experiments. These tools provide easy and convenient means to study the process.

A Cellular Automaton-Finite Volume-based model for evolution of interdendritic phases is coupled with a Particle Size Distribution-based model for precipitation of dispersoids across the grain. This comprehensive model has been used to study the effect of temperature, composition, as-cast microstructure, and cooling rates during post-homogenization quenching on microstructural evolution. The numerical study has been complimented with experiments involving Scanning Electron Microscopy, Energy Dispersive Spectroscopy, X-Ray Diffraction and Differential Scanning Calorimetry and a good agreement has with numerical results has been found.

The current work aims to study the microstructural evolution during homogenization heat treatment at both length scales which include the (i) dissolution and transformation of the as-cast secondary phases; (ii) precipitation of dispersoids; and (iii) reprecipitation of some of the secondary phases during post-homogenization cooling. The kinetics of the phase transformations are mostly diffusion controlled except for the η to S phase transformation in 7XXX alloys which is interface reaction rate controlled which has been implemented using a novel approach. Recommendations for homogenization temperature, time, cooling rates and compositions are made for Al-Si-Mg-Fe-Mn and Al-Zn-Cu-Mg-Zr alloys. The numerical model developed has been applied for a through process solidification-homogenization modeling of a Direct-Chill cast AA7050 cylindrical billet to study the radial variation of microstructure after solidification, homogenization and post-homogenization cooling.

CHAPTER 1. INTRODUCTION

1.1 Processing Stages of a Heat Treatable Aluminum Alloy

Aluminum alloys of 6XXX (Al-Si-Mg) and 7XXX (Al-Zn-Cu-Mg) series are the most commonly used alloys for extrusions. They fall in the category of "heat-treatable" alloys which can be heat treated for strength from precipitation strengthening. They find application in architectural, automobile and aircraft (7XXX) industry. The 6XXX and 7XXX alloys are characterized as the "soft" and "hard" alloys with yield strength of <375 MPa and >550 MPa respectively. The various processing stages of a heat treatable aluminum alloy like the 6XXX and 7XXX series alloys, undergoing extrusion are:

(i) Casting: The alloys are cast usually by Direct-Chill casting using grain refiners for a finer microstructure.

(ii) Homogenization: The alloys are homogenized at a temperature high enough to dissolve the coarse interdendritic phases at the grain boundaries. Post-homogenization cooling follows holding at the homogenization temperature.

(iii) Pre-heating: Pre-heat is done to dissolve any precipitates formed during quenching and to reduce the flow stress during extrusion.

(iv) Extrusion: The alloy billet is extruded through a die to the desired size and shape.

(v) Solution-treatment: The component is then, heated at a high temperature to result in a supersaturated solid solution on quenching.

(vi) Age-hardening: The component is heated at an intermediate temperature to precipitate strengthening particles.

A typical processing lifecycle of a 6XXX series alloy extrusion along with the temperature range for each stage is shown in Figure 1.1.

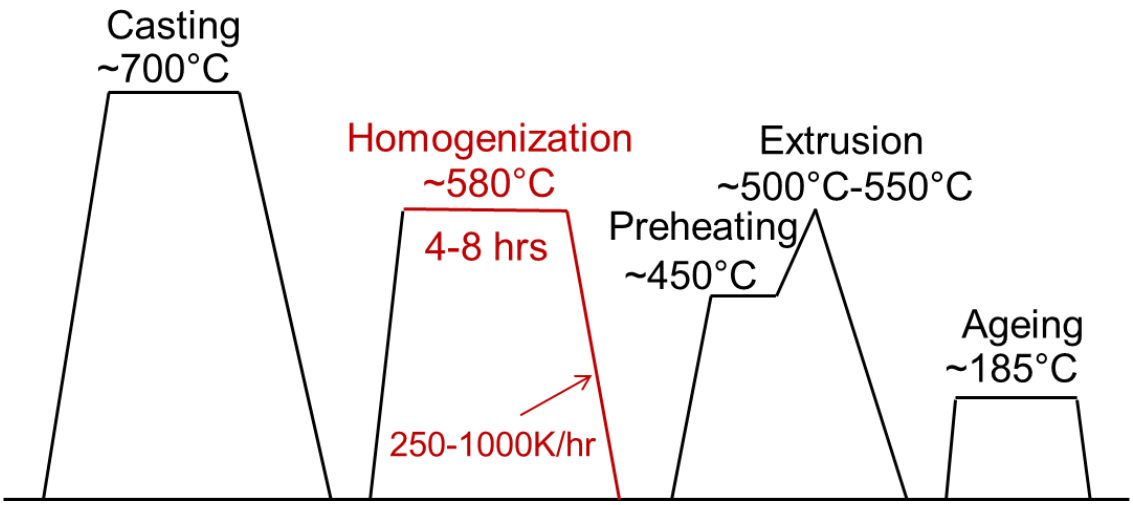

Figure 1.1: Schematic showing the various processing stages for a typical 6XXX alloy extrusion. The stages in red indicate the processes studied in this work.

1.2 Homogenization of As-cast Aluminum Alloys

Homogenization of as-cast alloys refers to the heat treatment provided to these alloys to eliminate the as-cast eutectic morphology and compositional inhomogeneity which are undesirable during downstream thermo-mechanical processing such as hot-rolling, extrusion, forging etc. Homogenization after casting of aluminum based alloys is an important process step which (i) reduces microsegregation leading to homogeneous properties across the secondary dendrite arm spacing; (ii) dissolves the eutectic phases formed during casting which have low melting point and may melt during subsequent processing; (iii) helps in spherodization of non-soluble phases to reduce stress

concentrators in the alloy improving the fracture toughness and enhances surface finish; and (iv) facilitates precipitation of dispersoids which pin grain boundaries inhibiting recrystallization during extrusion (for alloys containing Mn, Cr, Zr and Sc). Post-homogenization cooling conditions determines the nature and amount of secondary phases precipitated which determines the processing parameters during the thermo-mechanical processing that follows. These precipitates may also affect the age-hardenability of the alloy reducing the much desired mechanical strength of the component.

Microstructural evolution during homogenization is of immense importance as it determines the processing parameters during downstream processing and the resulting mechanical properties of the component. Microstructural development during homogenization and subsequent cooling occurs both at the length scale of the Secondary Dendrite Arm Spacing (SDAS) in μm and dispersoids in nm. This makes the problem complex, requiring characterization at both the length scales. Numerical tools to simulate microstructural development at both these length scales, which have been validated against experiments, provide a simple and convenient means to study homogenization. These numerical tools can be used for process optimization. They also provide insight into the mechanisms controlling phase transformations and morphological evolution during homogenization with lesser number of experiments. The phase transformation kinetics determines the time and energy consumed in homogenizing these alloys which may be as long as 48 hours for 7XXX alloys.

The aim of this work is to study the microstructural evolution during homogenization heat treatment at both the above mentioned length scales, which include the (i) dissolution and transformation of the secondary phases formed during casting; (ii)

precipitation of dispersoids and (iii) re-precipitation of some of the secondary phases during post-homogenization cooling. The numerical study has been complimented with experiments. The numerical model developed has been applied for a through process solidification-homogenization modeling of a Direct-Chill cast AA7050 cylindrical billet to study the radial variation of microstructure after solidification, homogenization and post-homogenization cooling.

1.2.1 Alloy chemistries

Both the 6XXX and 7XXX aluminum alloys may have Fe as an impurity which is difficult to eliminate during extraction and which produces undesirable phases such as the β-AlFeSi and α-Al(Fe,Mn)Si for 6XXX alloys[1] and Al_7Cu_2Fe in 7XXX series alloys[2].

Manganese is added to 6XXX alloys to mitigate the deleterious effects of acicular β-AlFeSi by transforming it to the more favorable globular α-Al(Fe,Mn)Si[3]. It may also have other elements such as Cr, Ti, Li, Zr and Sc in traces, some of which form dispersoids during homogenization and post homogenization quenching[4]. The alloy chemistry studied in this work is Al-Si-Mg-Fe-Mn alloy.

The Fe-containing Al_7Cu_2Fe phase in 7XXX series alloys remains after homogenization and is difficult to eliminate[2]. The alloy chemistry studied in this work is Al-Zn-Cu-Mg-Zr which is devoid of impurities like Fe, Mn and Ti which may otherwise be present in 7XXX alloys. Zirconium and scandium are added to 7XXX alloys to precipitate nano-sized coherent L_{12} precipitates which are very stable and inhibit grain boundary movement during recrystallization at high temperatures [5].

1.2.2 As-cast and as-homogenization microstructures

1.2.2.1 *Al-Si-Mg-Fe-Mn alloys*

As-cast Al-Si-Mg-Fe-Mn alloys are mostly α-Al with a eutectic morphology consisting of acicular β-AlFeSi (monoclinic crystal structure) and globular α-Al(FeMn)Si (cubic crystal structure) precipitates. The interdendritic regions may also have irregular Mg_2Si or Si particles depending on the composition[1]. The acicular β-AlFeSi are detrimental to the hot ductility of the extrusions due to their low melting points and their ability to act as stress concentrators[6]. They also degrade surface finish during extrusion[7]. The presence of Mn in the alloy enhances extrudability by changing the morphology of the interdendritic phases through the transformation of acicular β-AlFeSi to globular α-Al(FeMn)Si during homogenization[3].

Mg_2Si phase precipitates during post-homogenization quenching, depending on the Mg composition of the alloy [8]. The amount of Mg_2Si precipitated determines the amount of residual Mg in solid solution, which affect the flow stress during extrusion[9]. It lowers the flow stress during extrusion but also reduces the age-hardenability of the alloy as it requires Mg for precipitation of strengthening particles during the age-hardening heat treatment. The as-cast and homogenized microstructures for Al-Si-Mg-Fe-Mn alloys are shown in Figure 1.2 (a) and (b) respectively.

1.2.2.2 *Al-Zn-Cu-Mg-Zr alloys*

As-cast Al-Zn-Cu-Mg-Zr alloys are mostly α-Al consisting of a eutectic morphology of compositional variants of the η ($MgZn_2$) or the T ($Al_2Mg_3Zn_3$) as coarse interdendritic particles[10–12]. Deng at al.[2] reports Cu and Mg rich aluminides instead of the η or T phases in as-cast AA7050. They also reported traces of S (Al_2CuMg) phase. The

coarse η, Cu- and Mg-rich non-equilibrium aluminides, and the T phases, all of which are detrimental for the mechanical properties[12], transform to the more globular S phase during homogenization which in turn gradually dissolves at higher temperatures.

Along with the dissolution and transformation of the secondary phases, precipitation of nano-sized coherent L_{12} Al_3Zr dispersoids occurs across the grains. These dispersoids inhibit recrystallization by pinning grain boundaries during high temperature thermo-mechanical processing and the solution heat treatment[5].

Post-homogenization quenching reprecipitates some of the S, η/M, and T phases at various temperatures depending on their solvus[13]. This nucleation occurs at different nucleation sites including previously precipitated dispersoids, dislocations and grain boundaries[14]. These reprecipitated particles may act as nucleation sites for recrystallized grains, affect the mechanical properties, and reduce the age-hardenability of the alloy[15,16]. The as-cast and homogenized microstructures for Al-Zn-Cu-Mg-Zr alloys are shown in Figure 1.2 (c) and (d) respectively.

1.3 Research Objectives

1.3.1 Study of Microstructural Evolution in Al-Si-Mg-Fe-Mn Alloys during Homogenization and Post-homogenization Quenching

Microstructural evolution during homogenization of Al-Si-Mg-Fe-Mn alloys occurs in two stages at different length scales: while holding at the homogenization temperature and during quenching to room temperature. During holding at the homogenization temperature diffusion on the scale of the secondary dendrite arm spacing (SDAS) (in case of dendritic or grain size in case of a cellular microstructure), in micrometers occurs accompanied by phase transformations of the interdendritic phases at

the grain boundaries. The β-AlFeSi at the grain boundaries transforms to the α-Al(Fe,Mn)Si. On the other hand, post-homogenization quenching leads to Mg_2Si phase dispersoid precipitation at the nanometer to submicron scale. In this work, a numerical model has been developed that estimates microstructural changes during both the stages.

Numerical modeling of homogenization gives insight into transient microstructural behavior at both length scales, including factors affecting the phase transformations, allowing better control of the process and alloy chemistry and selection of homogenization temperature and quench rate to improve the process. In the current study, two different models have been used to study microstructural changes at the two length scales. A diffusion-based 2D finite volume-cellular automaton model simulates microstructural changes at the SDAS scale during homogenization and the Mg concentration distribution obtained is used as the starting point for a 1D finite difference model of precipitation at the dispersoid length scale during post-homogenization cooling. The models are thus "loosely" coupled to give a comprehensive picture of microstructural changes. The model development and validation is explained in detail in CHAPTER 2. This study is discussed in detail in CHAPTER 3.

This study aims to:

- model microstructural changes at both length scales during homogenization and post homogenization cooling;
- study the effect of processing parameters (temperature, time, and cooling rates) on microstructural evolution to obtain an optimum homogenization schedule;
- study the effect of composition on microstructure to obtain optimum composition ranges for minimum homogenization times, low flow stress during extrusion, and good

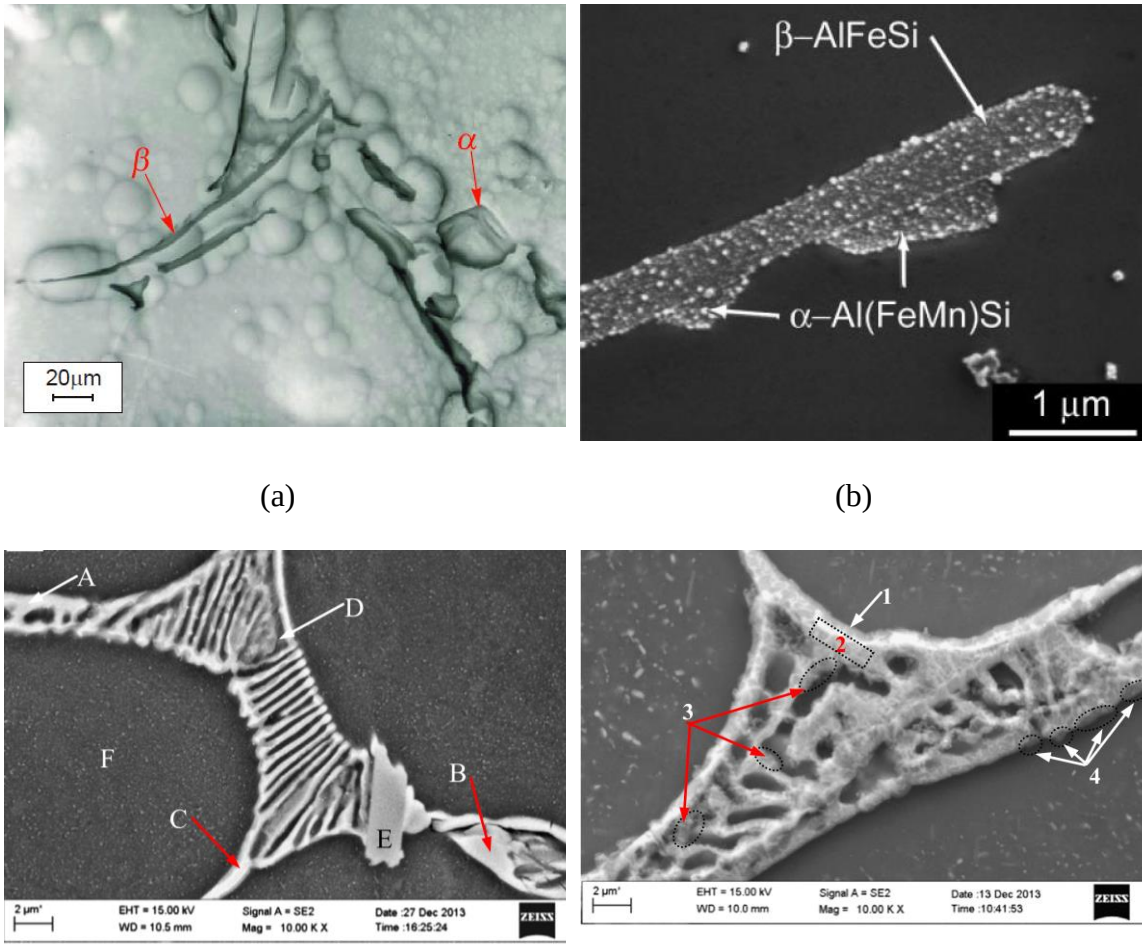

Figure 1.2: (a) As-cast Al-1.2Si-0.78Mg-0.33Fe-0.5Mn-0.14Cr alloy showing needle shaped β-AlFeSi and globular α-Al(Fe,Mn)Si phases[1] (Mrówka-Nowotnik et al.) (b) Nucleation of α-Al(Fe,Mn)Si on β-AlFeSi needles in AA6005 after homogenization for 2 hrs at 540°C[17] (Kuijpers et al.) (c) The solidification phases in as-cast AA7050 alloy[12] (Jia et al.) A/B/C: T phase, D: S phase, E: Al_7Cu_2Fe, F: α-Al matrix (d) Diffusion networks formed during homogenization showing nucleation of S phase after 2 hrs at 380°C[12] (Jia et al.) 1/2: T phase, 3/4: S phase.

age-hardenability, are based on Mg composition distributions after homogenization and cooling; and

- study the effect of as-cast microstructural features during casting on homogenization times to adjust the casting process to minimize time and energy spent on homogenization.

One reason to start with the study of microstructural evolution of a 6XXX alloy was that these alloys are important commercially and have been extensively studied experimentally. There exist reports of the experimental observations of microstructure during homogenization of a number of 6XXX alloys in literature. The alloy chosen in this study as the baseline case was AA6005 alloy. The numerical results have been compared with the experimental results in literature[17] and a close match has been found. The model developed for Al-Si-Mg-Fe-Mn system was the foundation on which the model for microstructural evolution in 7XXX alloys was developed.

1.3.2 Study of Microstructural Evolution in Al-Zn-Cu-Mg-Zr Alloys during Homogenization

As mentioned earlier the coarse interdendritic η to S phase transformation at the grain boundaries is accompanied with precipitation of nano-sized coherent metastable Al_3Zr dispersoids across the grains during homogenization of Al-Zn-Cu-Mg-Zr alloys. The microstructure gradually varies from the center of the grain to the grain boundary because of microsegregation making the problem complex. The alloy is fully homogenized when the interdendritic volume of remnant η, S and T phases is minimized and numerous fine Al_3Zr dispersoids precipitate across the grain.

Homogenization is a costly affair as the sluggish nature of these phase transformations requires a large amount of time[2,10]. For example, homogenization times for a given SDAS are underestimated even if the analysis is based on diffusion of Cu, the slowest diffusing major element[10]. For a diffusion-controlled phase transformation, diffusion is the slowest step and the dissolution of the secondary phases occurs before the Cu distribution across the SDAS becomes uniform. However, this is not the case for homogenization of some AA7XXX alloys, where an interface reaction rate-controlled kinetics for the phase transformation of secondary phases may be the rate-limiting phenomenon. Conversely, precipitation of Al_3Zr dispersoids is diffusion controlled and has been successfully modeled using the Kampmann Wagner Neumann (KWN) approach in the past[18], which predicts nucleation and growth of precipitates based on evolution of particle size distribution function. In this study a complete homogenization model has been used to consider both effects.

In the present study, a comprehensive model has been developed to predict microstructural changes simultaneously occurring at the two different length scales for a multicomponent Al-Zn-Cu-Mg-Zr alloy system. The phase transformation of η to S phase and the dissolution of both in the interdendritic regions is modeled using a cellular-automaton finite volume approach as used for Al-Si-Mg-Fe-Mn alloys, incorporating interface reaction-controlled kinetics, while the diffusion-controlled Al_3Zr precipitation in the grains is modeled using a finite difference Particle Size Distribution (PSD) model. The models are coupled together to predict changes in composition profiles in the primary α, which are gradually levelled by diffusion. The model is validated against experimental observations from electron microscopy, Energy Dispersive Spectroscopy (EDS), X-Ray

Diffraction (XRD) and Differential Scanning Calorimetry (DSC) conducted on as-cast and homogenized alloy samples. Composition profiles, volume fraction of the interdendritic phases, dispersoid number density and their radii have been compared. Based on the numerical results and experiments, an optimized homogenization schedule has been proposed for AA7050 which compares favorably with optimized experimental schedules in the literature. The advantage of the current model is that it can also be easily extended to optimize homogenization schedules for other 7XXX compositions. The numerical model is discussed in CHAPTER 2 and the study can be found in CHAPTER 4.

This study aims to:

- study microstructural changes at both length scales during holding at homogenization temperature; numerical results are validated through experiments involving EDS, XRD and DSC;
- study the effect of processing parameters (temperature and time) on microstructural evolution to obtain an optimum multi-stage homogenization schedule that minimizes time and energy consumption; and
- study the effect of composition on microstructure to obtain optimum composition ranges for minimum homogenization times, minimized recrystallization during extrusion and improved mechanical properties. The effect of compositions is discussed in CHAPTER 5.

1.3.3 Study of Reprecipitation of Secondary Phases in Al-Zn-Cu-Mg-Zr alloys during Post-homogenization Quenching

Post-homogenization quenching is important as larger precipitated particles may act as nucleation sites for particle-stimulated nucleation of recrystallization, which is

undesirable for mechanical properties of the alloy[15,16]. These particles may also remain undissolved during preheating and melt during thermo-mechanical processing, affecting the mechanical properties of the component[6]. Because 7XXX alloys are quench sensitive, it is very difficult to control precipitation during cooling after solution heat treatment before aging (more so at lower cooling rates), which reduces the age hardenability of the alloy by reducing the solute available for hardening precipitates[19].

Owing to the importance of cooling, in this work we aim to do a comprehensive study of precipitation during cooling over a range of cooling rates relevant to the industrial practice and a range of compositions belonging to the 7XXX alloys. We choose a numerical approach in this work first, validating our initial results with experiments (EDS, XRD, DSC). We have developed a Particle Size Distribution (PSD) based numerical approach to model precipitation of multiple phases of plate-like morphology during cooling from homogenization temperature of 7XXX alloys.

Time Temperature Transformation (TTT) and Continuous Cooling Curves (CCC) for aluminum alloys are difficult to construct using the traditional dilatometric methods owing to the small volume fraction of precipitates in these alloys. These have been constructed for some of the 7XXX alloys using resistivity and differential scanning calorimetry techniques. However, while these curves are necessary to optimize the age hardening heat treatment of these alloys, they do not exist for AA7050, a commercially important alloy. In this work, we use our numerical results to predict TTT and CCC for AA7050.

This study aims to:

- develop a model to study precipitation of multiple phases during post-homogenization quenching considering the experimentally observed plate-like morphology;
- study the effect of cooling rate on microstructural evolution to obtain an optimum cooling rate with optimum precipitation to have low flow stress and complete dissolution of the precipitates during extrusion and solution heat treatment to improve age-hardenability;
- study the effect of composition on microstructure to obtain optimum composition ranges for improved processability and age-hardenability; and
- predict CCC and TTT curves for AA7050 to help optimize the aging heat treatment.

This study has been discussed including the experiments performed to validate the numerical studies in detail in CHAPTER 6.

1.3.4 Study of Radial Variation of Microstructure after Homogenization across a DC-Cast AA7050 Billet

The models developed in this work are a part of the larger through-process modeling effort of the various processing stages for aluminum alloy extrusions such as casting, homogenization, extrusion and aging, discussed in section 1.1. This involves multiscale modeling to capture the keylinks among processing, structure and properties of heat treatable aluminum alloys. It involves modeling across different time and length scales. This forms the basis for Integrated Computational Material Engineering (ICME). ICME has been gaining importance in recent times owing to its contributions to enhancing performance and productivity of materials.[20,21]

This work studies the effect of homogenization heat treatment on the microstructure across the diameter of a DC-cast AA7050 cylindrical billet. The DC-cast billet has microstructure and macrosegregation as predicted by the DC casting solidification model by Fezi et al[22]. The solidification time as a function of radial positions predicted by this model and used to find the SDAS from an empirical relationship. These compositions and SDAS lengths are used as the initial microstructure for the homogenization and cooling models developed in this work. A heat transfer model for the billet predicts the temperatures at different radial positions during the heating and cooling cycles. All modes of heat transfer (conduction within the billets, convection and radiation at the surface) are considered. This work has been described in detail in CHAPTER 7.

This work is an example for the practical application of the models developed in this work. The heat treatment process causes a variation of microstructure across the radius of the billet due first to differences in initial compositions and SDAS which are produced during casting and also because temperature history is different at different radial positions. This study aims to:

- apply the solidification and homogenization models to a simulated DC-cast AA7050 cylindrical billet;
- predict the radial difference in microstructure based on the predictions of the DC-cast solidification model;
- study the effect of homogenization and post-homogenization cooling on microstructure across the radius; and
- design a homogenization heat treatment for the entire billet.

This work helps us understand the homogenization heat treatment for 6XXX and 7XXX alloys in a special reference to the phase transformations which occur at different length and time scales. The study enhances the understanding about the phase transformations, helping us design improved homogenization heat treatments. The computational tools developed in this work can be instrumental in prediction of microstructure during homogenization and post homogenization cooling. The tools are capable of both qualitative and quantitative prediction of morphology and microstructure. With modifications, these tools can also be used for prediction of microstructure during thermomechanical processing and aging heat treatments. The future recommended works are described in CHAPTER 8.

CHAPTER 2. NUMERICAL DESCRIPTION

2.1 Literature Review

Owing to the importance of the homogenization heat treatment, a number of attempts have been made to study it both experimentally and numerically in a wide variety of alloy systems. The emphases of these studies are: (i) microstructural evolution – dissolution, phase transformations, precipitation and the changes they bring to microstructure and properties; and (ii) transformation kinetics - factors affecting it which helps in process optimization. With growing advancement in computational capabilities, numerical modeling is increasingly being used to study homogenization. It is a cost effective means to gain insights into the factors controlling the kinetics and microstructure and to help fine-tune the process parameters to optimize the process.

Modeling homogenization requires knowledge of the as-cast microstructure, phase diagram information of the alloy system, diffusion coefficients, and parameters relating to nucleation and surface tension. A reasonable knowledge of the phase diagrams restricted the initial efforts to model homogenization. The initial attempts were basically particle dissolution based models in binary systems. But with the coming of reasonably accurate thermodynamic and kinetic databases through CALPHAD based softwares such as Thermo-Calc^{TM}, the homogenization models today provide more information. This section is a comprehensive attempt to review works in the past that modeled homogenization,

including their predictions and limitations. The numerical techniques used and major contributions of these studies have been highlighted. We start with the early studies in binary alloy systems and then move on to studies in multicomponent alloy systems.

2.1.1 Early Studies on Modeling Dissolution and Growth of Particles

Analytical models for particle dissolution in 1D were the first attempts to model homogenization and related processes such as aging. Aaron[23] and Whelan[24] produced the first analytical solutions for particle radius at various times during dissolution based on super-saturation and diffusivity. Tanzilli and Heckel[25] proposed a model for diffusion controlled, moving interface for spherical, planar and cylindrical geometries of precipitates. Aaron and Kotler[26] and Nolfi et al.[27] considered the varying effects of diffusion, interface reaction and curvature on dissolution or growth kinetics. Tundal and Ryum[28] studied the effect of size distribution of particles on dissolution kinetics in binary alloys and found it to have a significant effect. Nojiri and Enomoto[29] used Green's function method to model dissolution kinetics for spherical precipitates and showed that the same method can be used for growth of non-zero radius particles. This model was used to study the effect of curvature by Enomoto and Nojiri[30] again, who found that the dissolution rate was faster for smaller precipitates. Sinder and Pelleg[31] considered homogenization after dissolution of precipitates in a planar and spherical geometry and found homogenization to be much slower for the planar case.

2.2 Studies in Multicomponent Multiphase Systems

Vermolen et al.[32] formulated a mathematical model to study dissolution of stoichiometric Mg_2Si particles in Al-Si-Mg alloys. It was a 1D diffusion problem with a moving boundary, which is also known as a Stefan problem. The model considered a

simple geometry but took grain size distribution into consideration. It was assumed that the concentrations at the interface had a constant solubility product at that temperature. The evolution of second phase fraction and matrix inhomogeneity with time were studied. Although lab-scale experimental validation was not done, the homogenization times predicted matched the industrial practice. In a different study using the same methodology, a Finite Element model was used to simulate phase transformation of β-AlFeSi to α-Al(FeMn)Si in Al-Mg-Si alloys[17]. The interfacial concentrations were determined from solubility product information from Thermo-Calc™. The geometry of the computational domain consisting of the two phases was inspired from experimental observations. The model could predict the transformed volume fractions up to 50% transformation when compared to experimental values.

The Alstruc homogenization model[33] was developed in 2001 in an attempt to semiquantitatively estimate microstructural changes in 3XXX, 5XXX, 6XXX wrought alloys and Al-Si foundry alloys during homogenization and cooling. It has separate sub-routines for each alloy. The program incorporates a multiparticle model to deal with particle nucleation, coarsening and growth during heating and cooling cycles and one-particle dissolution model to deal with dissolution, transformation and spheroidization of the interdendritic particles during holding. The phase diagram information is incorporated from sources in literature. The model results compared well with experiments and the existing discrepancies were attributed to inaccurate phase diagram information.

A diffusion-based 1D model was used to simulate homogenization in binary and ternary Mg-Al-Zn alloys by Das et al.[34] The 1D model consisted of the matrix phase and the second phase with dissolution occurring at the moving boundary. Local equilibrium

was maintained at the interface, based on thermodynamic data from FactSage FTlite database. The phase fraction evolution for the binary Mg-Al was found to match the experiments. The model was extended to ternary alloys. The model did not predict phase transformations, precipitation and partial melting at grain boundaries during homogenization.

Phase field is a widely used methodology to predict microstructural evolution. A minimization of Gibbs free energy which has an interfacial and chemical component is used to determine the morphology and the local phase fractions and concentrations. Warnken et al.[35] modeled as-cast microstructure in Ni-based superalloys using phase field and extended the study to homogenization heat treatment. The free energy and mobility data was procured from CALPHAD databases published by NIST. A multiphase field method was used to study phase evolution in as-cast Aluminum alloys by Bottger et al.[36] and was extended to homogenization. This model was able to predict evolution of multiple phases and concentration profiles with time during homogenization.

Eivani et al.[37,38] modeled different aspects of homogenization in Al-Zn-Mg alloys using different models. They predicted the dissolution of Al-Fe-Mn-Si particles through the Thinning Discontinuation and Full Dissolution mechanism[37] and verified the results experimentally. They considered a diffusion-based 2D model to simulate dissolution of cylindrical precipitates with round edges and surface perturbations. The volume fractions and thickness of the precipitates matched well with experiments. However, they found that the dissolution of the low melting phases was an interface reaction controlled (transfer of elements across the interface was the slowest step controlling the dissolution rate) rather than a diffusion controlled process. He calibrated the kinetic coefficient for the interface

reaction from the experimental results and was able to reproduce the dissolution rates better than the diffusion controlled model.

Development of the commercial software, DICTRA™ (Diffusion Induced Transformations), which could simulate diffusion induced transformations in 1D led to various studies in the field of homogenization of alloys. Samaras and Haidemenopoulos [39] and Haidemenopoulos et al.[40] studied homogenization in 6XXX series Aluminum alloys using DICTRA™ which includes multicomponent diffusion. They used composition profiles after casting as predicted by Thermo-Calc™, as initial conditions. They could predict dissolution of Mg_2Si and transformation of β-AlFeSi to α-Al(FeMn)Si during homogenization of these alloys. The transformed volume fractions were compared to experimental results from Kuijpers et al.[17] The model however, underestimated the homogenization times when compared to experiments which may be because of the 1D nature of the model.

Many numerical studies have focused on simulation and optimization of the nucleation of dispersoids[4,38,41,42] during homogenization considering the importance of dispersoids in inhibiting the recrystallization during later thermomechanical processing. This involves length scales much smaller than that considered for dissolution and phase transformation simulation. In one of the earlier studies, Robson and Prangnell[18] modeled nucleation, growth and coarsening of the Al_3Zr precipitates in AA7050 based on an approach by Kampmann and Wagner[43]. The model predicted number densities and precipitate radii distributions which compared well with the experiments. Based on the model predictions, they proposed a two-step homogenization process which would considerably increase the dispersoid number density in low Zr containing areas of the

grains and thereby reduce the recrystallized fraction. This practice is currently used in industrial homogenization of AA7050. A similar model was proposed by Eivani et al.[38] for Al-4.5Zn-1Mg and they were able to make predictions of number densities and radii which matched experiments. The effect of homogenization temperature, time and Zr composition was also evaluated.

In a more recent work by Du et al.[42], they have coupled numerical models at the two length scales to predict microstructural evolution in Al-Mn-Fe-Si alloys during homogenization. They have used a 1D Pseudo-Front Tracking (PFT) model based on work by Gandin and Jacot[4] to simulate the dissolution of the interdendritic phase and a Kampmann and Wagner[43] approach to model dispersoid nucleation, growth, and coarsening. Both the models use Thermo-Calc^{TM}. The two models are coupled using the splitting method adopted by Pope[44] in combustion modeling where the spatial distribution of a component is affected by both rate of reaction such as precipitation or combustion and change due to mixing such as diffusion or convection. The predicted composition profiles, volume fraction of the interdendritic phases, size distribution of dispersoids, and width of the dispersoid free zones at different temperatures compared well with experimental results.

The numerical model of phase nucleation, growth and coarsening in the current work is derived from the early studies with modifications for a multicomponent system coupled with Thermo-Calc^{TM} for thermodynamic data. It incorporates the effects of curvature on the morphology. The microstructural evolution during homogenization occurs at two different length scales: the coarse interdendritic particles dissolve and transform to globular intermetallics, while fine dispersoids are precipitated during homogenization and post-homogenization cooling. These changes are modeled using a cellular automaton finite

volume model and a particle size distribution finite difference model, respectively. These models have been coupled together for the two alloy systems studied.

2.3 Cellular-Automaton Finite Volume Model

The microstructural changes occurring at the grain boundaries where the coarse interdendritic particles formed during casting dissolve and transform to the more favourable globular intermetallics are modelled using a cellular automaton finite volume model. This model simulates:

(i) dissolution of coarse interdendritic paticles;

(ii) transformation to globular interdendritic

(iii) redistribution of alloying elements across the grain through diffusion

The 2D finite volume-cellular automaton model predicts microstructural evolution in a simple and computationally efficient manner, based on the solidification model of Krane et al.[45] and Shao et al.[46], as modified as below for solid-solid phase transformations. The model predicts multicomponent diffusion-controlled, interface reaction controlled and mixed controlled dissolution and growth of solid phases depending on local temperature and curvature.

2.3.1 Growth and Dissolution Algorithm

The computational domain is divided into a uniform Cartesian grid of cells, each of which is the α phase (matrix), β phase, γ phase or an interface including more than one phase. In each interface cell, the volume fraction of phases $\beta+\gamma$ is between 0 and 1, with the remainder being α-Al. The rejection and absorption of solute near the phase boundaries

sets up composition gradients in the α-Al matrix and the multicomponent diffusion of those elements is found from the solution to the species conservation equations,

$$\frac{\partial C^i}{\partial t} = \sum_j D_{ij}^k \left[\frac{\partial^2 C^j}{\partial x^2} + \frac{\partial^2 C^j}{\partial y^2} \right], \tag{2.1}$$

in which interaction of different element gradients is modeled with cross diffusion terms ($i \neq j$). The diffusion equations (2.1) are discretized using an implicit finite volume method and solved using Gauss-Siedel with successive over-relaxation[47]. Each simulation time step consists of first the growth algorithm followed by the solution of the diffusion equation (2.1). The grid spacing used was capable of resolving the microstructural features at the SDAS length scale. This grid size was chosen after calculations at smaller grid sizes showed no significant dependence on Δx.

The growth algorithm is different depending on the kinetic rate controlling step during the phase transformation. Two processes run in series to complete the transformation: the diffusion of alloying elements across the grain and the exchange of atoms at the interface of the interdendritic particles. The rate controlling step is the slowest of the two. The kinetics is diffusion controlled when diffusion across the grains is the slowest step or the interface reaction rate controlled when exchange of atoms at the interface is the slowest step.

2.3.1.1 *Diffusion Controlled Kinetics*

The change in fraction of the precipitate phases is calculated by exchanging solute with the neighboring cells to keep all phases in interface and neighboring cells at their

equilibrium values, as calculated by Thermo-Calc™ and adjusted for interface curvature. The changes in phase fractions (e.g., Δf_β or Δf_γ, which may be positive or negative) are found from a mass balance of each component, *k*, before and after the movement of the phase boundary:

$$\left(1-f_\beta-f_\gamma\right)C_\alpha^k+f_\beta C_\beta^k+f_\gamma C_\gamma^k+\sum_{i=1}^{n}\sum_{j=1}^{3}C_{ji}^k=\left(f_\beta+\Delta f_\beta\right)C_\beta^{k*}+ \left(f_\gamma+\Delta f_\gamma\right)C_\gamma^{k*}+\left(1-f_\beta-f_\gamma-\Delta f_\beta-\Delta f_\gamma\right)C_\alpha^{k*}+\sum_{i=1}^{n}\sum_{j=1}^{3}C_{ij}^{k*} \tag{2.2}$$

$$\Delta f_\beta\left(C_\beta^{k*}-C_\alpha^{k*}\right)+\Delta f_\gamma\left(C_\gamma^{k*}-C_\alpha^{k*}\right)=\left(1-f_\beta-f_\gamma\right)\left(C_\alpha^k-C_\alpha^{k*}\right) +f_\beta\left(C_\beta^k-C_\beta^{k*}\right)+f_\gamma\left(C_\gamma^k-C_\gamma^{k*}\right)+\sum_{i=1}^{n}\sum_{j=1}^{3}\left(C_{ji}^k-C_j^{k*}\right) \tag{2.3}$$

On the right side, the first 3 terms refer to the changes in composition of 3 phases in the interface cell, while the last term is the rejection or pick-up from *n* neighboring cells. Each interface cell is updated with the new volume fractions and phase concentrations and the solute absorbed or rejected is distributed among the neighboring cells as described in Krane et al.[45] modified for multicomponent and multiphase system.

2.3.1.2 *Interface Reaction Rate-controlled Kinetics*

The driving force for phase transformations at the interface cell is dissipated by the diffusional processes or work against "frictional" forces of the interface expressed as[48]:

$$\Delta G_{df}=\Delta G_{diff}+\Delta G_{fric} \tag{2.4}$$

For diffusion controlled phase transformations, the "friction" offered by the interface is negligible. Diffusion in the matrix is slower than the exchange of atoms at the interface leading to local equilibrium at the interface. However, for interface reaction rate controlled phase transformations exchange of atoms at the interface is slower than diffusion in the matrix leading to off-equilibrium conditions at the interface. The friction at the interface determines its velocity, expressed as[48]:

$$v = M\Delta G_{fric} \tag{2.5}$$

where, mobility of the interface, *M* has a dependence on temperature, *T* similar to diffusion coefficient.

$$M = M_0 \exp(\frac{-Q_m}{RT}) \tag{2.6}$$

In the present study, phase fraction changes for the precipitate phases (η and S phases) in the interface cell are calculated with the assumption of both diffusion-controlled and interface reaction rate-controlled phase transformations. For the latter, ΔG_{df} is calculated from Thermo-Calc™ and the TCAL1 database using the TQ-Interface. For interface reaction rate controlled process, ΔG_{diff} is assumed to be small compared to ΔG_{fric} leading to the assumption:

$$\Delta G_{df} \cong \Delta G_{fric} \tag{2.7}$$

Equation (2.6) is used in (2.4) to calculate the velocity of the different interfaces which for a 1D case transforms to the phase fraction change for different phases according to:

$$\Delta f_{\beta/\alpha} = \frac{v_{\beta/\alpha}\Delta t}{\Delta x} \tag{2.8}$$

The interfaces of different phases are assumed to be parallel to each other and the cell boundary with their velocities perpendicular to the interfaces. The total volume fraction change of any given phase, *j*, is the sum of volume fraction of all other phases transforming to phase *j*.

An important aspect of an interface reaction rate controlled process is the off equilibrium concentrations of the phases at the interface. The precipitate phases are assumed to be at equilibrium concentrations which seems to be a valid assumption owing to the limited solubility and very slow diffusivities of intermetallic phases. The concentration of component k in the α–Al matrix is calculated by mass conservation of the component before and after phase change in the interdendritic cell expressed as equation (2.9) giving the value for the new off equilibrium matrix composition for a 1D case where cell 1 is the interface cell and cell 2 its neighbor.

$$[(1-f_\beta-f_\gamma-\Delta f_\beta-\Delta f_\gamma)C_\alpha^{k\,new}+\ (f_\beta+\Delta f_\beta)C_\beta^{k*}+(f_\gamma+\Delta f_\gamma)C_\gamma^{k*}]+ \qquad (2.9)$$

$$C_\alpha^{k\,new}=[(1-f_\beta-f_\gamma)C_\alpha^{k\,old}+f_\beta C_\beta^{k\,old}+f_\gamma C_\gamma^{k\,old}]+C_\alpha^{k\,neighbor}$$

$$C_\alpha^{k\,new}=\frac{\sum_{j=1}^{2} f_j\left(C_j^{k\,old}-C_j^{k*}\right)+(1-f_\beta-f_\gamma)C_\alpha^{k\,old}+C_\alpha^{k\,neighbor}-\Delta f_\beta C_\beta^{k*}-\Delta f_\gamma C_\gamma^{k*}}{2-f_\beta-f_\gamma-\Delta f_\beta-\Delta f_\gamma} \qquad (2.10)$$

On both sides of equation (2.9), the first 3 terms denote the solute in three phases in the interface/interdendritic cell 1; whereas, the fourth term is for the neighboring cell 2.

After the phase fractions from diffusion controlled and interface reaction rate controlled processes are calculated, they are compared and the smaller of the two is chosen as the phase fraction change. This assumption is realistic as there is a competition between

the thermodynamic driving force leading to equilibrium conditions and the kinetic restraint offered by the interface which determines the extent of phase change.

In every time step, phase fraction changes are calculated. The amount of solute rejected or absorbed in the process is distributed in the neighboring cells described by Krane et al.[45] with modifications for multicomponent and multiphase systems. The concentrations developed at the interface are then levelled by the diffusion process in each time step.

2.3.2 Thermodynamic and Kinetic Data

Commercial software for thermodynamic calculations (Thermo-Calc™, using the TQ-Interface and TCAL1 database) calculates the equilibrium concentrations. Software for diffusion-controlled phase transformations (DICTRA™) generates diffusion coefficients of component *i* in the presence of component *j in* the α-Al matrix ($D_{ij}^{\alpha-\mathrm{Al}}$) as a function of temperature using the aluminum-based mobility database (MOBAL2).

$$D_{ij}^{\alpha-\mathrm{Al}} = D_0 \exp\left(-\frac{Q_d}{RT}\right) \tag{2.11}$$

The constants, D_0 and Q, are found for each element in the matrix and are listed in Appendix A. The diffusion coefficients are assumed to be independent of composition over the range studied. Diffusion coefficients in intermetallic phases are negligible compared to those in the matrix.

2.3.3 Nucleation Model

The nucleation of α-Al(FeMn)Si on β-AlFeSi needles for Al-Si-Mg-Fe-Mn alloys is predicted using the model of Thevoz et al.[49] This model assumes a continuous, Gaussian

distribution of $\frac{dN}{d(\Delta G)}$ over possible values of the driving force for nucleation, ΔG, which depends on supersaturation.

$$\frac{dN}{d(\Delta G)} = \frac{N_{max}}{\Delta G_\sigma \sqrt{2\pi}} e^{-\left[\frac{\Delta G - \Delta G_N}{\sqrt{2}\Delta G_\sigma}\right]^2} \tag{2.12}$$

There exists no reference for the values of nucleation constants for this model for 6XXX alloys. The value n_{max} determines the size of the plot of the Gaussian distribution of dn/d(ΔG) over possible values of the driving force for nucleation and does not affect the nucleation probability. The driving force, ΔG_N, for transformation of β-AlFeSi to α-Al(FeMn)Si has been calculated from Thermo-Calc and this value has been used as a reference around which the values have been varied to match model predictions to the experimental initial β-AlFeSi to Al(FeMn)Si transformation rates in Kuijpers et al[17]. The fitted distribution is defined by its amplitude (n_{max} = 1000), the value of the mean driving force for nucleation (ΔG_N = 8000 J/mole), and the distribution's standard deviation (ΔG_σ = 1500 J/mole). A sensitivity test has been performed, and the results vary less as compared to the variation in the constants as seen in Figure 2.1. The area under the curve in equation (2.12), represents the cumulative probability for nucleation (*n*) in the interface cell of interest as a function of undercooling.

$$n(\Delta G) = \int_0^{\Delta G} \frac{dn}{d(\Delta G)} .\, d(\Delta G) \tag{2.13}$$

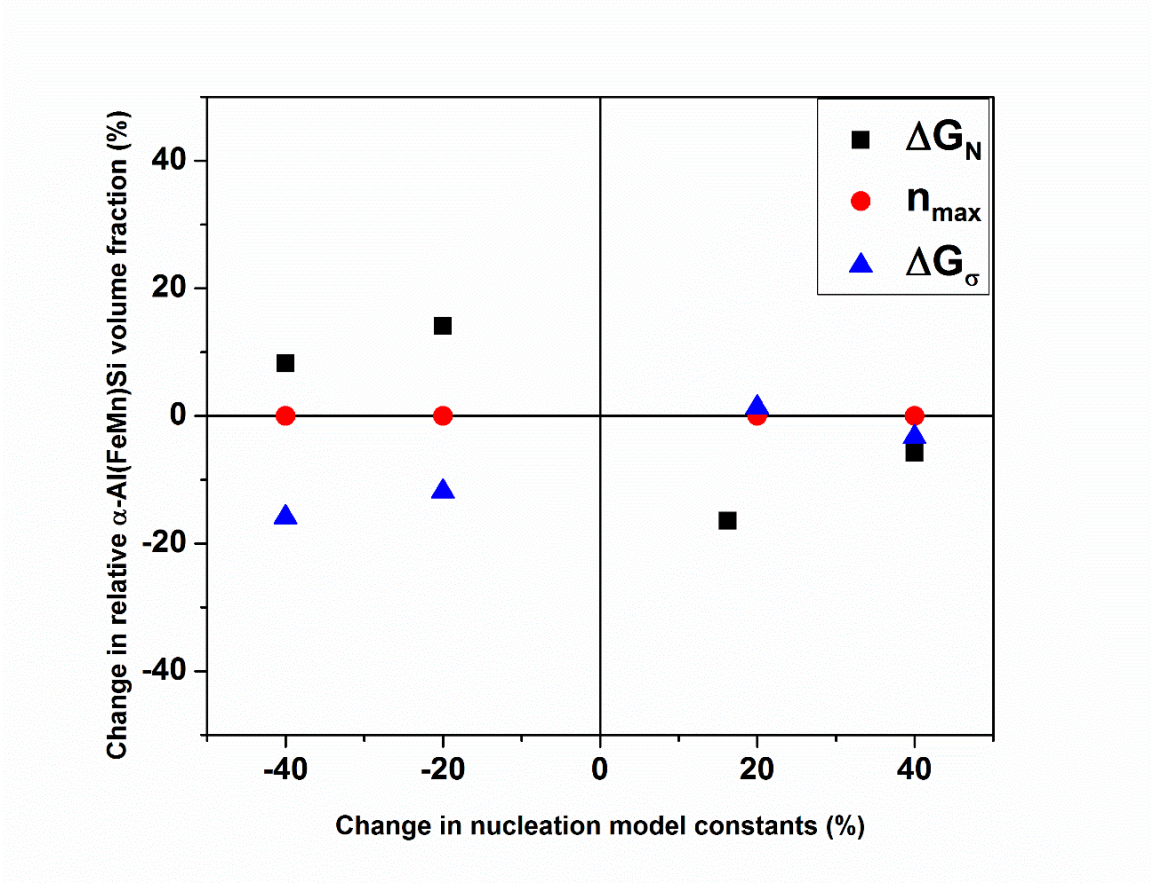

Figure 2.1: Sensitivity of constants in the nucleation model

The driving force for nucleation is calculated as a function of local concentration and temperature in Thermo-Calc™. This probability of nucleation is compared to a random number between 0 and 1 to determine if the α-Al(FeMn)Si phase nucleates in a given interface cell. If nucleation occurs, the volume fraction of the new phase and composition redistribution is found from the growth algorithm discussed above.

2.3.4 Curvature Model

The equilibrium concentration calculations from the thermodynamic databases do not account for interface curvature, which does influence morphological evolution. The matrix

equilibrium concentration including curvature is calculated using the Thomson-Freundlich equation[50],

$$ln\frac{C_\alpha^{i*}}{C_\alpha^i} = \frac{2\gamma\kappa V_\beta}{RT} \tag{2.14}$$

The calculation of curvature is important as it guides the morphological evolution of the precipitates. Curvature in equation (2.13) is calculated using the height function method developed by Cummins et al.[51] for Volume Of Fluid (VOF) interfaces. The first step is the determination of the normal to the phase boundary, as described in Yanke et al.[52] If the normal is more vertical, then a 3×7 array of control volumes around the interface cell of interest is used to find κ. The curvature of a 2D line can be found from

$$\kappa = \frac{d^2y}{dx^2}\left[1+\left(\frac{dy}{dx}\right)^2\right]^{-3/2}, \tag{2.15}$$

where the derivatives are approximated by the finite differences

$$\frac{dy}{dx} = \frac{y(3)-y(1)}{2\Delta x} \quad \text{and} \quad \frac{d^2y}{dx^2} = \frac{y(3)-2y(2)+y(1)}{\Delta x^2}. \tag{2.16}$$

The estimated positions of the interface in each of the three columns ($y(i)$, i = 1,2,3) are used to evaluate the differences in equation (2.16). Examples of these calculations are found in Figure 2.2. The number in each cell represents the volume fraction of the different phases which sum to give y-values during curvature calculation. If the normal is more horizontal, the same procedure is applied to a 7×3 array of cells where the height function is taken in the x direction in the 3 rows.

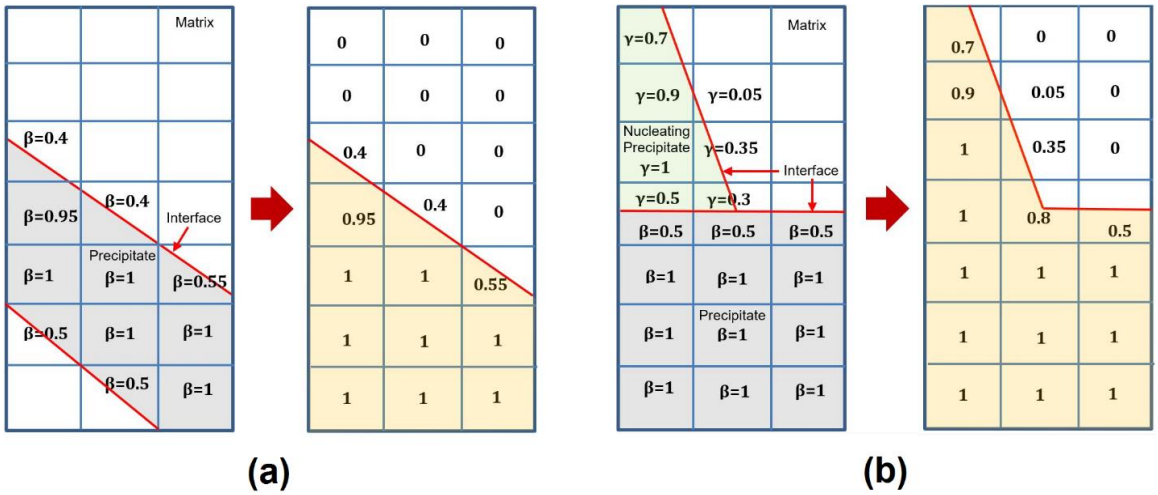

Figure 2.2: Height function calculations for curvature of center cell in 3X7 array. (a) microstructure with stray interface: y(1) = 4.35, y(2) = 3.4, y(3) = 2.55. (b) microstructure with nucleating phase, γ, on an existing phase, β: y(1) = 6.6, y(2) = 4.2, y(3) = 3.5.

2.3.5 Model Validation

2.3.5.1 *1D and 2D Binary Model*

The model has been developed in stages starting from a 1D binary two-phase model and moving on to 2D multicomponent three-phase model. The 1D binary homogenization model has been validated against the analytical solution[53]. A 2-phase Al-Al_2Cu diffusion couple is chosen for the validation, where the position of the interface changes due to difference in equilibrium concentrations of both the phases. The initial and final concentrations of the two phases and the diffusion coefficient chosen for the validation test are shown in Figure 2.3(a). A grid dependence study has also been done. (Figure 2.3(b)). The solutions are found to closely match the analytical solution for grid size of 1×10^{-8} m.

Also, the binary and ternary models have been validated with well-known transformations from DICTRA, such as austenite to ferrite.

The 2D validation of the model involved comparing the dissolution rate of a circular precipitate in a uniform matrix with the approximate solution for smaller times from Whelan[24]. A grid size of 10^{-7} m is used. The analytical and numerical solution for a binary system is shown in Figure 2.3(d). The numerical solution differs from the analytical solution by a maximum of 0.2 μm at 10 s.

2.3.5.2 *Homogenization of Al-Si-Mg (Ternary) Alloy*

Dissolution of Mg_2Si during homogenization of a ternary Al-1Si-1.6Mg alloy was studied for an initial validation of the work. The initial microstructure consisted of a matrix α-Al phase and a eutectic phase with an aggregate composition of α-Al-Mg_2Si eutectic. The morphology of the initial microstructure is shown in Figure 2.4(a). The homogenization process is simulated at four different temperatures: 487, 507, 527 and 547 °C. The equilibrium volume percentage of Mg_2Si phase predicted by Thermo-Calc^{TM} at these temperatures are 1.54%, 1.32%, 0.77% and 0.77% respectively. A eutectic structure treated numerically as one phase with an average composition of 6.4 wt% Si and 10.6 wt % Mg is used. Within the first few seconds, the region with eutectic composition breaks into globular Mg_2Si particles. The spheroidization is very fast owing to the large compositional differences between the eutectic structure and the equilibrium precipitate phase. The elongated precipitates are spheroidized with time as observed in Figure 2.4.

The predictions show that microsegregation developed during solidification is substantially reduced within the first 10-15 min of homogenization as the Mg_2Si volume

decays exponentially with time (Figure 2.5). This matches experiments by Cai et al.[54] The decay is slower for lower temperatures than at higher temperatures. The dissolution kinetics curve seems to have 2 stages with different rates. Initially, the dissolution is very rapid until the equilibrium volume fraction at that temperature is reached. At these early times, the rate of volume change is governed by large differences between the equilibrium and existing concentrations of the precipitates. The dissolution rate decreases as the precipitate dissolution is governed more by curvature and the concentration difference has decreased.

The equilibrium state of the precipitate and the matrix is governed by two factors: the equilibrium concentrations and the interface curvature. The rate of volume change of the precipitate phase is governed by diffusion near the interface. After the bulk of the precipitate and matrix away from the interface reach nearly equilibrium concentrations for a given temperature, the growth or dissolution of the precipitates is governed primarily by the curvature effects and larger precipitates grow at the expense of the smaller ones. This also validates the curvature model as it models the Oswald ripening.

2.3.5.3 *Homogenization of Multicomponent Multiphase Alloys*

For multicomponent three-phase model, the comparisons with current transformation rate predictions and the experimental data are found in CHAPTER 3 and 4 for Al-Si-Mg-Fe-Mn and Al-Zn-Cu-Mg-Zr alloys. To illustrate the ability of the model to maintain shape during curvature-dominated phase transformations, a planar coherent interface between β-AlFeSi and an α-Al matrix, with a third nucleating phase (α-Al(FeMn)Si) at the phase boundary, was simulated. This interface remains planar during dissolution of the β (Figure 2.6). A circular precipitate (θ-Al_2Cu) with an incoherent

interface to an α-Al matrix remains circular while dissolving. The same results are found for both cases during growth of the intermetallics.

2.4 Particle Size Distribution Finite Difference Model

During the quenching from the homogenization temperature, microstructural changes occur at a much finer length scale (1nm-1μm) than the dissolution of the as-cast structure during homogenization. Modeling the precipitation and growth of dispersoids at the scale of the secondary arm spacing (10-100μm) would be computationally very expensive, a particle size distribution based model based on work by Myhr and Grong[55] has been developed for two different morphologies: spherical and plate-shaped precipitates formed during homogenization of the alloys. The various assumptions in the model are:

(i) Precipitates of different phases of pre-assigned morphologies are allowed to nucleate and with overlapping growth and coarsening stages depending on supersaturation.

(ii) The interfacial energy is assumed to be constant all around the precipitate.

(iii) The precipitates are assumed to be nucleating heterogeneously on pre-existing dispersoids and dislocations in the alloy.

(iv) The growth of the precipitates is dependent on the supersaturation of the slowest diffusing element in the precipitate phase.

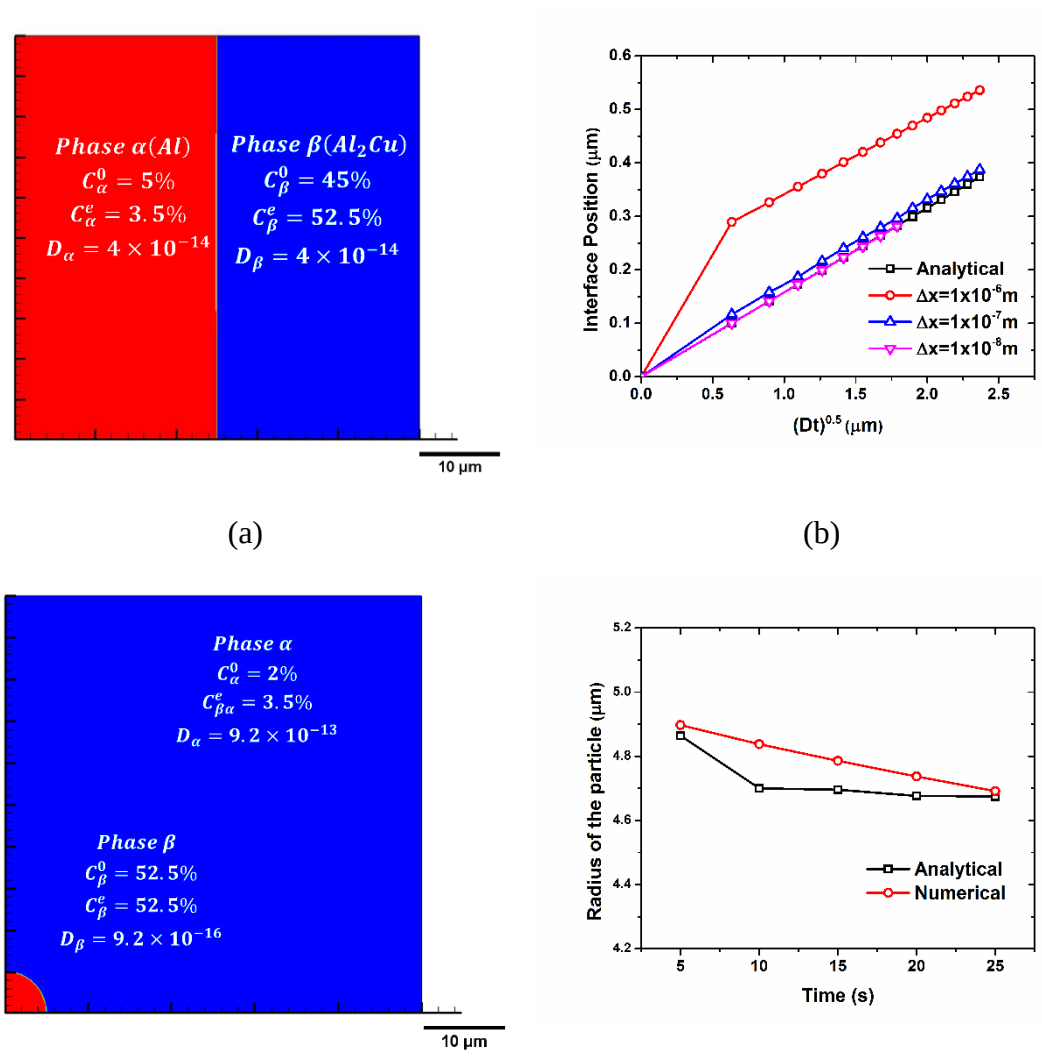

Figure 2.3: (a) Initial (5% for α and 45% for β); final concentrations (3.5% for α and 52.5% for β) and diffusion coefficients (4×10^{-14} m^2/s for both the phases) for the 2 phase 1D binary model validation experiment; (b) Grid dependent solutions for the binary model and its comparison with the analytical solution; (c) Initial (2% for α and 52.5% for β); final concentrations (3.5% for α and 52.5% for β) and diffusion coefficients (9.2×10^{-13} m^2/s and 9.2×10^{-16} m^2/s for α and β respectively) for the 2 phase 2D binary model validation experiment. (b) The analytical and numerical solutions for a grid size of 10^{-7}m.

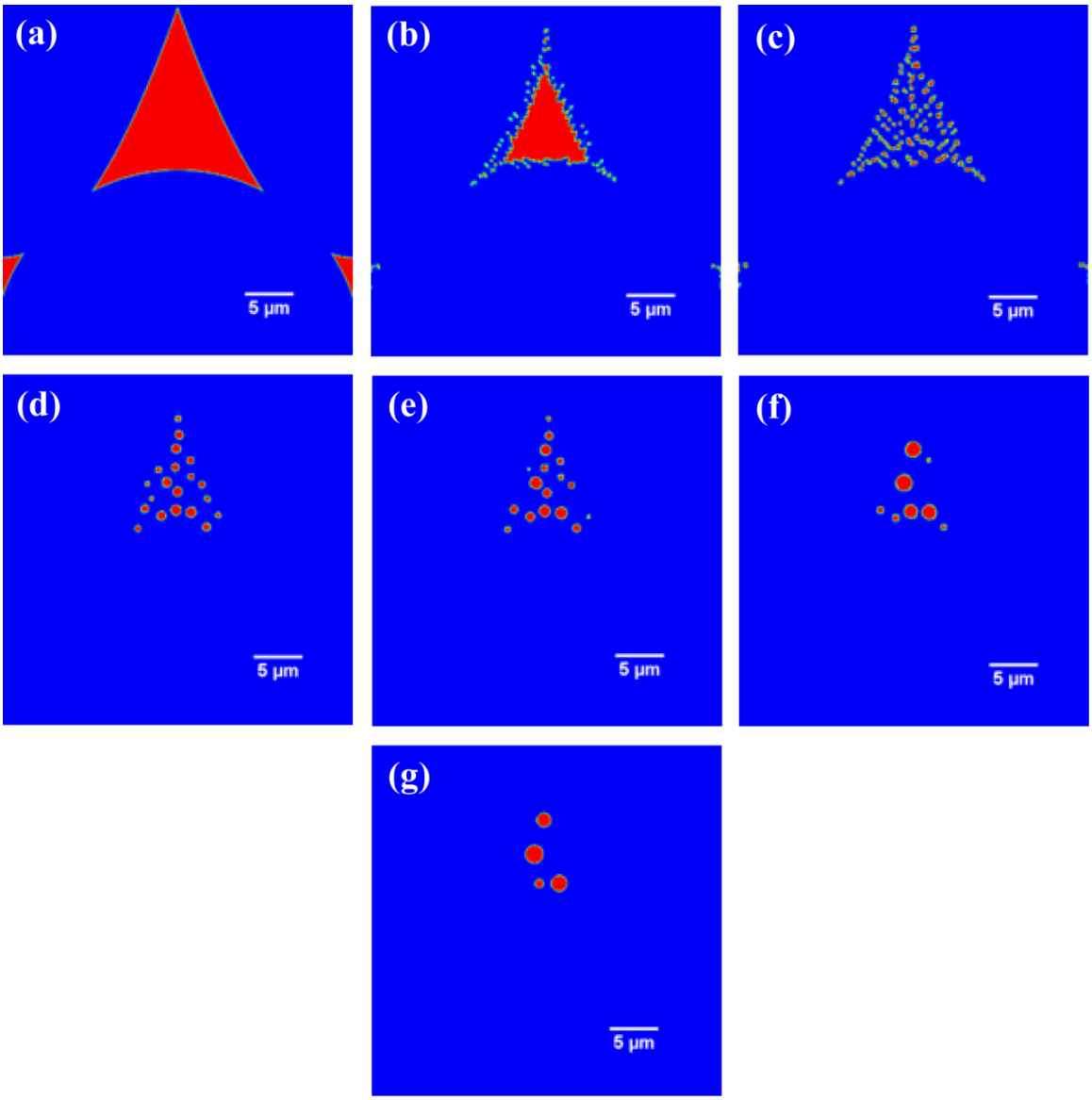

Figure 2.4: (a) Initial microstructure; and microstructures after (b) 0.05 s; (c)10 s; (d) 0.5 h; (e) 1 h; (f) 2 h; and (g) 4 h of homogenization at 820 K (547°C). The final volume fraction is lower than that predicted by Thermo-Calc^{TM} due to curvature effects.

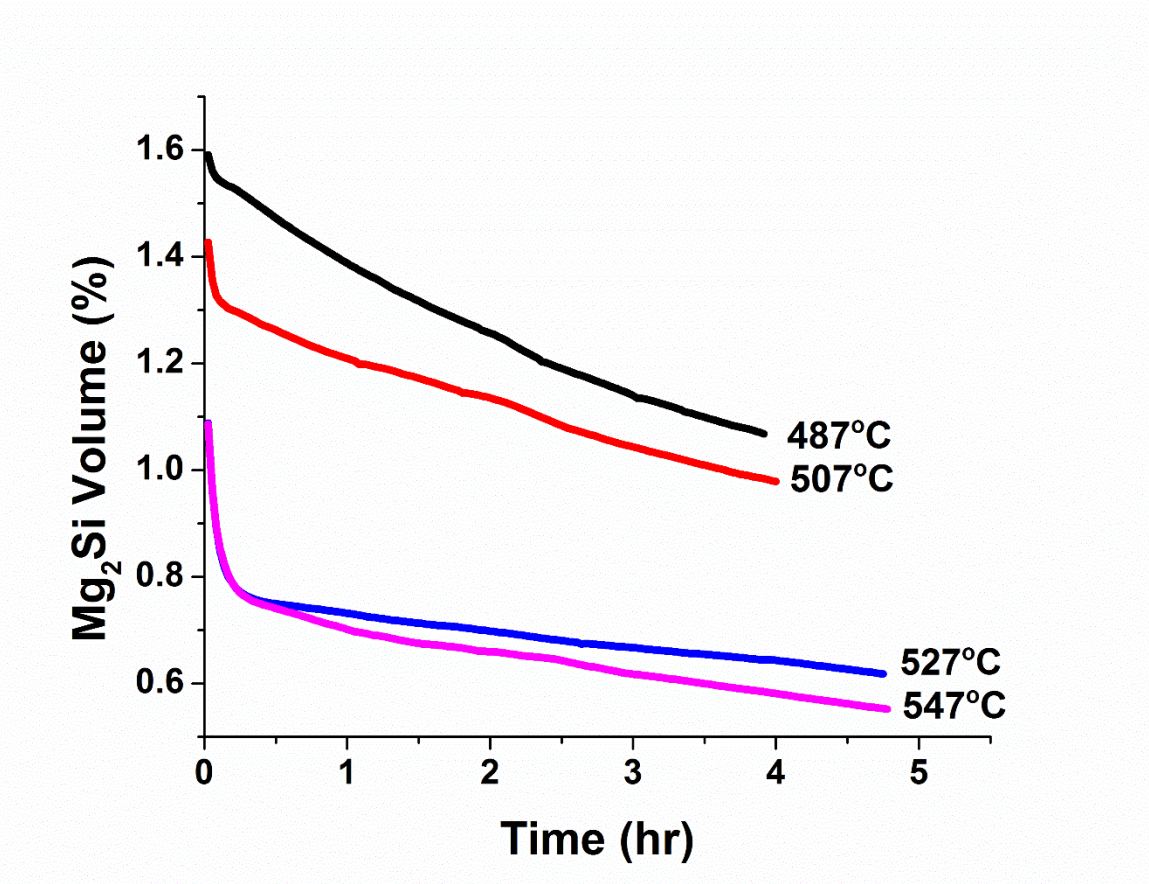

Figure 2.5: Simulated dissolution kinetics of the precipitates at different temperatures from the 2D homogenization model.

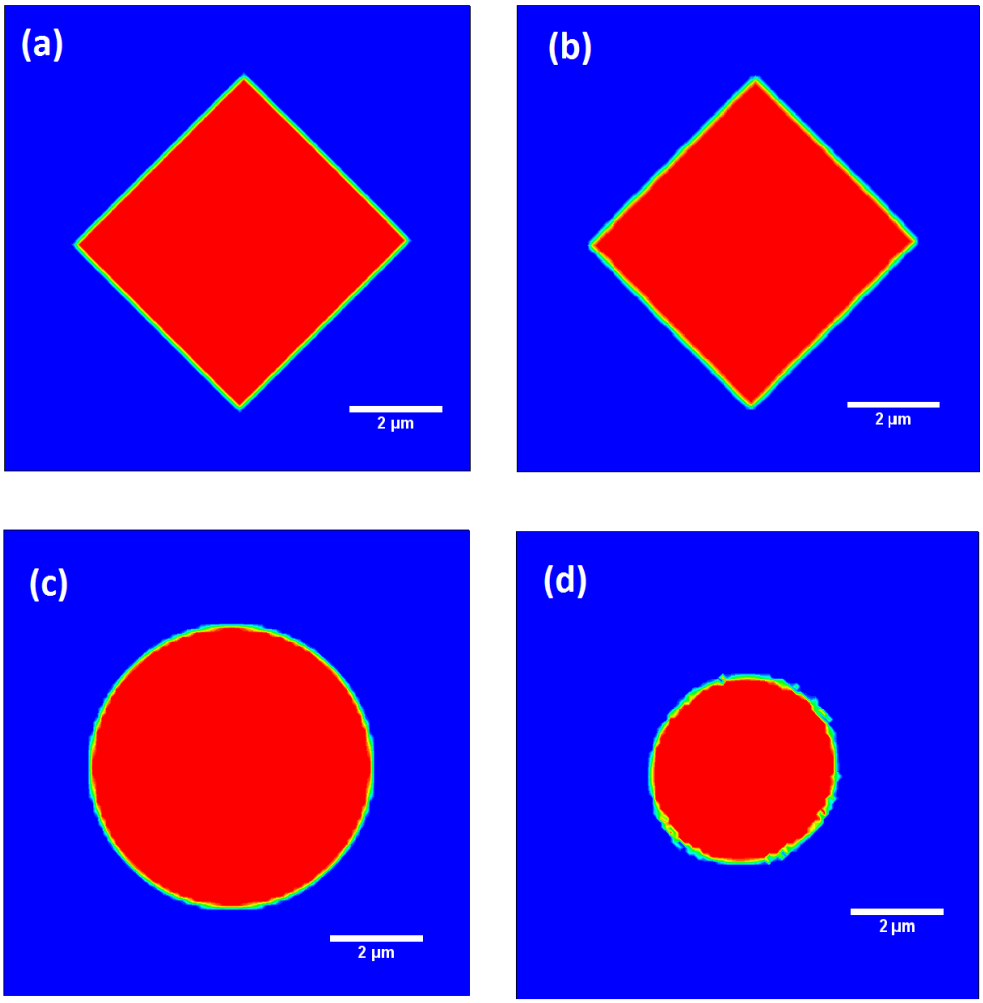

Figure 2.6: Curvature driven evolution of a dissolving square precipitate (a) initial (b) at 1 hr (β-AlFeSi in α-Al matrix) and of a circular precipitate (c) initial (d) at 1 hr (Al_2Cu in α-Al matrix) .

The governing equation for particle size distribution for a 1D radial domain where control volumes represent size classes can be written as[55]

$$\frac{\partial N^j}{\partial t} = -\frac{\partial (N^j v^j)}{\partial r} + j^j, \tag{2.17}$$

The first term in equation (2.17) is the flux of number densities across the size classes which are the control volumes, the second term is the convective term representing growth of dispersoids and the third term is the number density increase due to nucleation.

2.4.1 Nucleation Model

A classical model for heterogeneous nucleation is used in this work. Neglecting the incubation period, a steady-state heterogeneous precipitation rate for a binary system is used[55]:

$$j = j_0 \exp\left(-\frac{\Delta G^*_{het}}{RT}\right) \exp\left(-\frac{Q_d}{RT}\right), \tag{2.18}$$

Ignoring coherency strains, ΔG^*_{het} can be expressed as[55],

$$\Delta G^*_{het} = \frac{(A_0)^3}{(RT)^2 \left(ln(\bar{C}/C_e)\right)^2} \tag{2.19}$$

where A_0 is the potency of heterogeneous nucleation sites. The above nucleation model has been used for precipitation after cooling for Al-Si-Mg-Fe-Mn alloys considering that the nucleation and growth of the dispersoids only depend on the Mg composition for a pseudo-binary Al-Mg_2Si system.

The modified nucleation model in for a multicomponent Al-Zn-Cu-Mg-Zr alloy has been used for precipitation of Al_3Zr dispersoids during homogenization and precipitation of η ($MgZn_2$), S (Al_2CuMg), T ($Al_2Zn_3Mg_3$) and Θ (Al_2Cu) during post-homogenization

cooling. The source term, j, in eqn. (2.17) is modeled by classical nucleation theory for heterogeneous nucleation as[4]:

$$j = (N_{max} - N_{tot}) Z \beta exp\left[-\frac{\Delta G_{hom} f(\theta)}{k_B T}\right], \tag{2.20}$$

where N_{max} is the number of heterogeneous nucleation sites present in the alloy taken as $1.5\times10^{21}/m^3$ which is the estimated number of dislocation intersections, and N_{tot} is the total number of existing dispersoids. The factor Z, is the Zeldovitch's factor accounting for fluctuations in nucleus size due to exchange of atoms between the nucleus and the matrix $Z = \frac{\Delta G_N^2}{2\pi V_B \gamma^{3/2} \sqrt{N_{Av} RT}}$. The coefficient β in eqn. (2.20) is the rate of transfer of solute atoms from matrix to the nucleus expressed for a multicomponent alloy as $\beta = \frac{4\pi r_c^2}{a^4}\ Min(D_i x_i)$, where r_c is the critical radius of the dispersoids given by $r_c = \frac{2\gamma V_B}{\Delta G_N}$. In eqn (2.19), ΔG_{hom} is given by $\Delta G_{hom} = \frac{16\pi\gamma^3 V_B^2}{3\Delta G_N^2}$. Present work assumes heterogeneous nucleation. The wetting angle function, $f(\theta)$ in eqn. (2.20) is expressed as $f(\theta) = \frac{1}{4(2+cos\theta)(1-cos\theta)^2}$. The values of the parameters considered in this work have been taken from numerical studies from Gandin and Jacot in the literature[4]. The driving force for nucleation in a multicomponent alloy is calculated as[4]:

$$\Delta G_N = RT \sum_{i=1}^{n} x_p^i \ln\left(\frac{x_\infty^i}{x_m^i}\right), \tag{2.21}$$

2.4.2 Growth Model

Growth of the precipitates of phase *j* of radius *r* represented by v^j can be expressed as[55]

$$v^j = \frac{dr}{dt} = \frac{\bar{C} - C_i^j}{C_p^j - C_i^j} \frac{D_i}{r}, \tag{2.22}$$

for spherical precipitates and

$$v^j = \frac{dr}{dt} = \frac{1}{3} \left(\frac{\bar{C} - C_i^j}{C_p^j - C_i^j} \frac{AD_i}{pt}\right)^{-1/2}, \tag{2.23}$$

for plate-shaped precipitates[56]. That interface concentration, C_i^j, is calculated after taking account of interfacial curvature using the Thomson-Freundlich equation from the equilibrium composition given by the phase diagram, C_e^j. The interfacial concentration for the spherical[50] and plate-shaped precipitates[57] can be expressed as:

$$ln \frac{C_i^j}{C_e^j} = \frac{2\gamma^j \kappa V_j}{RT} \tag{2.24}$$

and

$$\frac{C_i^j}{C_e^j} = \left\{1 + \left(\frac{A_{eq} + A}{A_{eq}}\right) \frac{\gamma^j V_j}{rRT} \frac{1 - C_e^j}{C_p^j}\right\} \tag{2.25}$$

respectively.

The driving force for nucleation and the critical nuclei are calculated at each time step for a given concentration of the alloying elements. Taking into account size fluctuations[58], j^j nuclei are added to size class corresponding to $r_{eff} = r_c + 1/2\sqrt{\frac{k_B T}{\pi\gamma}}$ as shown in Figure 3.1(b). The size evolution in time is calculated using equation 2.16 for the desired homogenization schedules. The control volume size is $1 \times 10^{-10} m$ and time step Δt varies with temperature. The first control volume starts at $\Delta r/2$ and no dispersoids are

allowed in the last control volume to allow for the free growth of all the precipitated dispersoids. The governing equation (2.17) is discretized using an implicit time scheme and solved at each time step using the Tridiagonal Matrix Algorithm (TDMA)[47].

2.4.3 Model Validation

The results of the precipitation model are in good agreement with the experiments of Sun et al.[59] during post-homogenization cooling of Al-Si-Mg-Fe-Mn alloys. Predicted peaks in dispersoid size distributions from different post-homogenization cooling conditions (air-cooled, and furnace-cooled) fall in the range of $\pm 0.25\ \mu m$ of the experimental observations (Table 2.1). The mean dispersoid sizes for the different cooling rates are also compared and are seen to decrease with increasing cooling rates.

The experimental results in CHAPTER 4 (precipitation of Al_3Zr dispersoids) and CHAPTER 5 (precipitation during cooling) also show a reasonable match with the predicted results for Al-Zn-Cu-Mg-Zr alloys.

Table 2.1: Comparison of the peaks in the dispersoid size number density distributions from predictions of the current model and the experiments of Sun et al.[59]

Cooling rate	Numerical peak dispersoid size (μm)	Experimental peak dispersoid size (μm)	Experimental mean size (μm)
Furnace cooled (0.036 °C/s)	0.5	0.25	0.19±0.10
Air cooled (0.83°C/s)	0.1	0.25	0.18±0.09
Water quenched (140°C/s)	0.001	0.2	0.16±0.06

2.5 Coupling the Two Models

The models at the grain size or the SDAS length scale is coupled with the model at the dispersoid size length scale for both the alloy groups studied. While the end homogenized compositions predicted by one model serves as the initial composition for the second model to predict precipitation during cooling of Al-Si-Mg-Fe-Mn and Al-Zn-Cu-Mg-Zr alloys leading to a 'loose' coupling, for prediction of precipitation of Al_3Zr dispersoids during homogenization of Al-Zn-Cu-Mg-Zr alloys, both the models are 'tightly' coupled as the concentrations predicted by one model is used by the second model and vice-versa as will also be explained in CHAPTER 4.

CHAPTER 3. MICROSTRUCTURAL EVOLUTION DURING HOMOGENIZATION OF AL-SI-MG-FE-MN ALLOYS

3.1 Introduction

Microstructural evolution during homogenization and quenching of these alloys is complex, with changes occurring at two length scales:

(1) Secondary dendrite arm spacing (SDAS) length scale (10-100 μm): Dissolution and phase transformation of needle-like β-AlFeSi into globular α-Al(FeMn)Si (Kuijpers et al.[17]), and dissolution of Mg_2Si (Cai et al.[54]) occurs during homogenization. The evolution depends on the temperature and time of homogenization, composition of the alloy, and the size of microstructural features in the as-cast alloy.

(2) Dispersoid length scale (1 nm-1 μm): Precipitation of fine, spherical Mg_2Si occurs during post- homogenization quenching (Milkereit et al.[8]). More Mg left in the α-Al matrix after precipitation and growth of Mg_2Si increases the flow stress during extrusion, while less Mg decreases the age-hardenability of the alloy after extrusion. The microstructure at the dispersoid length scale depends on the rate of post-homogenization cooling and Mg content of the alloy.

Compositions and processing routes leading to easy-to-extrude microstructures are not obvious. While addition of Mn facilitates the transformation of needle-like β-AlFeSi into globular α-Al(FeMn)Si[3], addition of Mg and Si improves the age-hardenability[9] of the alloy. The β-AlFeSi is difficult to eliminate during casting due to very low solubility of Fe

in Al. However, this phase can be controlled by adopting measures during casting discussed later which affect the relative α-Al(FeMn)Si volume fraction and β-AlFeSi needle thickness. To what extent these features affect the time taken for homogenization when transformation from β-AlFeSi to α-Al(FeMn)Si is complete is examined here.

Homogenization of these alloys has been studied with both experiments and numerical models in the past. Birol[60–62] optimized the homogenization schedule for 6063, 6005 and 6060 by examining experimentally the microstructure, conductivity, and microhardness of these alloys. He proposed homogenizing long enough to transform all β-AlFeSi to α-Al(FeMn)Si and cooling the alloy in the range of 100-300ºC/hr, so dispersoids precipitate fine enough to dissolve during extrusion but remain undissolved during preheat, increasing extrudability and age hardening potential. The typical extrusion temperatures are 500-550ºC as compared to the preheat temperatures of 450°C and homogenization temperatures of 580°C[59].

Numerical modeling of homogenization gives insight into transient microstructural behavior at both length scales, including factors affecting the phase transformations, allowing better control of the process and alloy chemistry and selection of homogenization temperature and quench rate to improve the process. Numerical studies by Kuijpers et al.[17] and Haidemenopoulos et al.[40], simulated homogenization of 6000 series alloys using finite element modeling and DICTRA™, respectively. While their results predict the trends in the experiments, the models in Kuijpers et al.[17] and Haidemenopoulos et al.[40] underpredict measured homogenization times. Possible approaches to improve agreement are: (i) consideration of multi-component diffusion; (ii) use of 2D or 3D models; and (iii)

consideration of spatial distribution and scale of microstructural features such as thickness of β-AlFeSi needles.

In the current study, two different models have been used to study microstructural changes at the two length scales. A 2D finite volume-cellular automaton model simulates microstructural changes at the SDAS scale during homogenization and the Mg concentration distribution obtained is used as the starting point for a 1D finite difference model of precipitation at the dispersoid length scale during post-homogenization cooling.

3.2 Domain Description

Several sets of conditions were used in this study to simulate the effect of temperature, composition (Fe, Mn, Si), and microstructural features in the as-cast alloy on kinetics during isothermal homogenization. The baseline conditions for these studies were a composition of Al-0.83Si-0.7Mg-0.27Fe-0.18Mn (wt %), which falls within the composition specification of AA6005, and T = 580 ºC. The SDAS was taken as 24μm, with relative α-Al(FeMn)Si volume fraction of 0.10 and a β-AlFeSi plate thickness of 0.4 μm, all of which fall in the experimental ranges for as-cast AA6005[63]. This baseline condition consists of needle shaped β-AlFeSi and globular α-Al(FeMn)Si and Mg_2Si phases in the interdendritic region, as seen in Figure 3.1(a). To simulate the evolution of an α-Al(FeMn)Si seed on a β-AlFeSi needle during homogenization, a hemispherical seed is added on one of the needles. A composition gradient from the center of the dendrite to the interdendritic region is assumed, based on Scheil type[64] solidification calculated by Thermo-Calc™. The grid spacing used was $\Delta x = \Delta y = 10^{-7}$ m, which was capable of resolving the microstructural features at the SDAS length scale. This grid size was chosen

after calculations at smaller grid sizes showed no significant dependence on Δx below 10^{-7} m.

The Mg composition across the SDAS is homogenized after holding at the homogenization temperature, which is used as the initial condition for the precipitation model during quenching. The numerical domain for the smaller scale precipitation model is a 1D radial domain where dispersoid size classes are the control volumes as shown in Figure 3.1(b). The values of all the parameters are taken from Myhr and Grong[55], who simulated precipitation and growth in Al-Si-Mg alloys. The 1D radial domain is discretized with an implicit finite difference method. The number evolution in the 15000 control volumes corresponding to different size classes (0.1nm-3μm) is done using the nucleation and growth models as discussed in CHAPTER 2.

The first variation from the base case was lowering the homogenization temperature to 540ºC and 570ºC. The effect of initial alloy composition on homogenization kinetics was studied in ranges of C^{Si}, C^{Fe}, C^{Mn}, and C^{Mg} which cover the specification of most of the 6XXX alloys[65]. The SDAS was taken as 24μm with relative α-Al(FeMn)Si volume fraction of 0.1 and β-AlFeSi plate thickness of 0.4 μm. Table 3.1 shows the specific compositions for these cases. The effect of the relative sizes of as-cast microstructural features on homogenization behavior was also studied for variations of β-AlFeSi plate thickness and α-Al(FeMn)Si volume fraction. The specific values of these microstructural features, shown in Table 3.2, fall in the ranges experimentally observed by Sha et al[66].

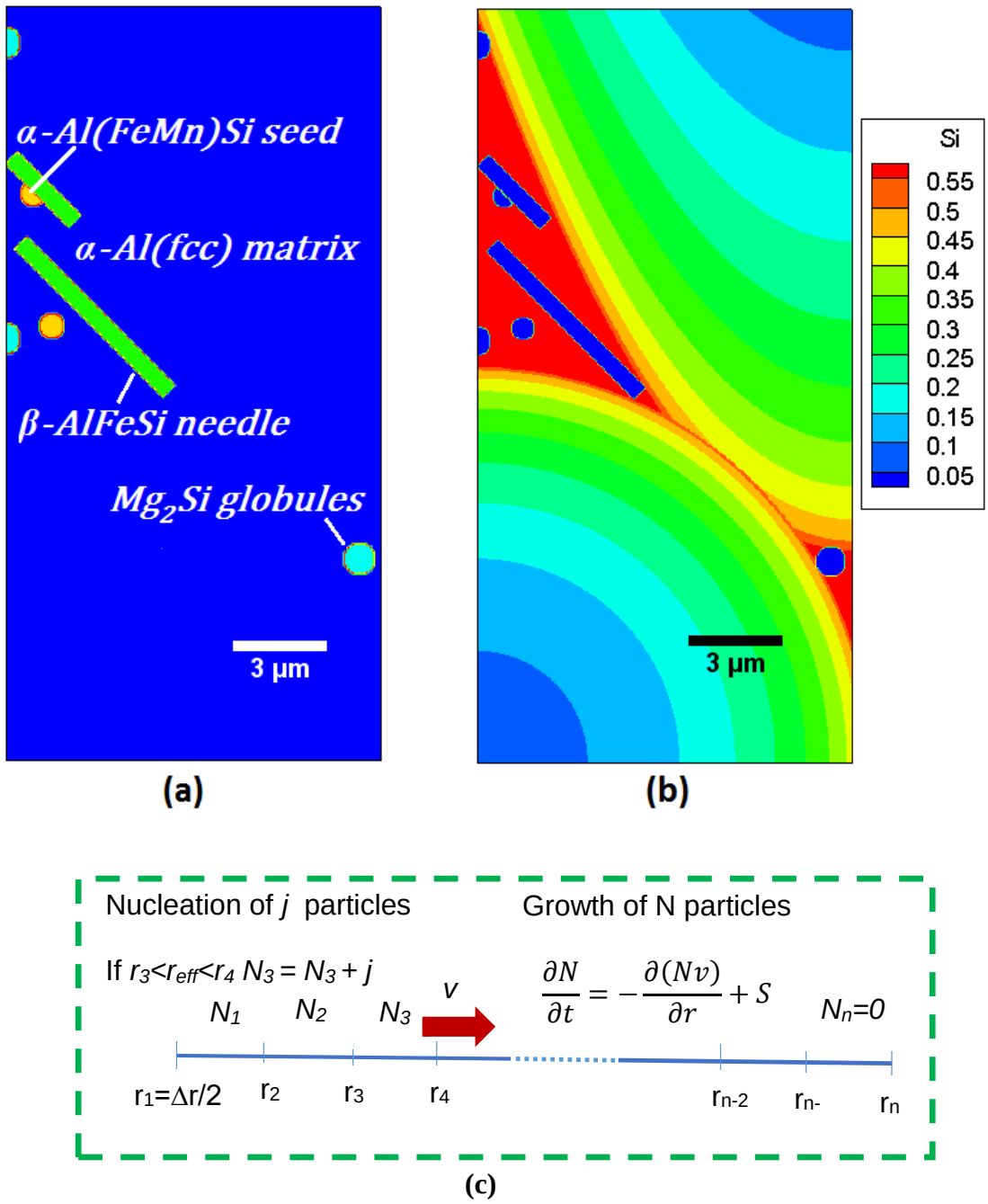

Figure 3.1: (a) Baseline initial microstructure for homogenization models. Colors indicate the different phases: green β-AlFeSi; orange α-Al(FeMn)Si; cyan Mg_2Si; and blue: α-Al matrix. (b) Baseline initial concentration field, based on non-equilibrium (Scheil) solidification. (c) The numerical radial domain for the precipitation model showing nucleation and growth of dispersoids.

The effect of Mg content on the precipitation behavior of Mg_2Si during post-homogenization cooling was studied for Mg composition in the range of 0.5-1.1%. At the homogenization temperature of 580°C, 0.7% Si is left in the alloy which does not form part of the of the remnant α-Al(FeMn)Si after holding for 8hrs from the calculations using the homogenization model for the base case of Al-0.83Si-0.7Mg-0.27Fe-0.18Mn. Thus for the composition of other elements (Fe and Mn), there is enough Si in the alloy for the entire range of Mg composition studied here considering Mg to Si ratio in Mg_2Si to be 2:1. From thermodynamic calculations in Thermo-Calc^{TM}, Mg does not form a part of the remnant α-Al(FeMn)Si and is responsible for the amount of Mg_2Si precipitated during post-homogenization cooling. The cooling rates chosen for the study were 1000, 500, 250and 150°C/hr which includes the industrially practiced cooling rate of 150°C/hr.

Table 3.1: Variation in alloy composition to study its effect on homogenization kinetics

Cases	Fe (wt %)	Mn (wt %)	Si (wt %)	Mg (wt %)
Fe1	0.07	0.18	0.83	0.7
Fe2	0.17	0.18	0.83	0.7
Fe3	0.27	0.18	0.83	0.7
Fe4	0.37	0.18	0.83	0.7
Mn1	0.27	0.01	0.83	0.7
Mn2	0.27	0.1	0.83	0.7
Mn3	0.27	0.2	0.83	0.7
Mn4	0.27	0.3	0.83	0.7
Si2	0.27	0.18	0.6	0.7
Si3	0.27	0.18	0.8	0.7
Si4	0.27	0.18	1.2	0.7

Table 3.2: Variation in as-cast microstructural features to study their effect on homogenization times.

Cases	SDAS (μm)	β-AlFeSi plate	Relative α-Al(FeMn)Si fraction (%)
Pt1/Ra1	24	0.4	10
Pt2	24	0.5	10
Ra2	24	0.4	30
Ra3	24	0.4	40

3.3 Microstructural Evolution during Homogenization

In this study, two phase transformations are simulated during the homogenization of the as-cast structure:

(i) Dissolution of Mg_2Si and

(ii) Transformation of β-AlFeSi to α-Al(FeMn)Si.

3.3.1 Baseline Behavior of Microstructure

The predicted microstructural evolution during homogenization of the baseline composition at 580^{o}C can be seen in Figure 3.2. These changes include the complete and rapid dissolution of globular Mg_2Si and the slower growth of globular α-Al(FeMn)Si from transformation of needle shaped β-AlFeSi and by the coarsening of the existing α-Al(FeMn)Si, consistent with published measurements by Cai et al.[54], Kuijpers[63], and Haidemenopoulos et al.[40] The needles of β-AlFeSi dissolve, forming α-Al(FeMn)Si at its interface with the α-Al. The needles thin and break into smaller needles. During dissolution, surface perturbations provide nucleation sites for α-Al(FeMn)Si, forming a necklace of growing precipitates in the interdendritic region. The initial α-Al(FeMn)Si globules

coarsen and maintain their shape. These predicted growth of the α-Al(FeMn)Si phase matches well with the experimental observations of Kuijper et al.[17], as seen in Figure 6. Here the relative volume fraction of α-Al(FeMn)Si is defined as ratio of the volume fraction of α-Al(FeMn)Si to the total volume fraction of α-Al(FeMn)Si and β-AlFeSi. The transformation of β-AlFeSi to α-Al(FeMn)Si is complete when the relative volume fraction reaches 1 which is referred to as the homogenization time. However, removal of microsegregation in α-Al may require more time.

For a more detailed examination of the microstructural evolution during baseline homogenization conditions, Figure 3.3 shows more of the transient behavior of the alloy. Figure 3.3(a) clearly shows two distinct stages of the process. In stage I, there is a rapid decrease in the β-AlFeSi volume fraction, which dissolves into α-Al matrix and transforms to α-Al(FeMn)Si. This stage continues until the local excess Mn in the matrix (indicated by the hump around X = 17-18 μm in Figure 3.3(b)) diffuses away into the matrix or is consumed by the growing α-Al(FeMn)Si. Once the excess Mn is gone between 25 and 30 minutes, a transition to stage II occurs. By this time, local excess of Fe concentration have also disappeared, as seen in Figure 3.3(c). In Stage II, the transformation rate is much less and gradually decreases with time. The dissolution of β-AlFeSi into the α-Al matrix is complete and the remaining β-AlFeSi transforms to α-Al(FeMn)Si, slowing down the overall transformation rate.

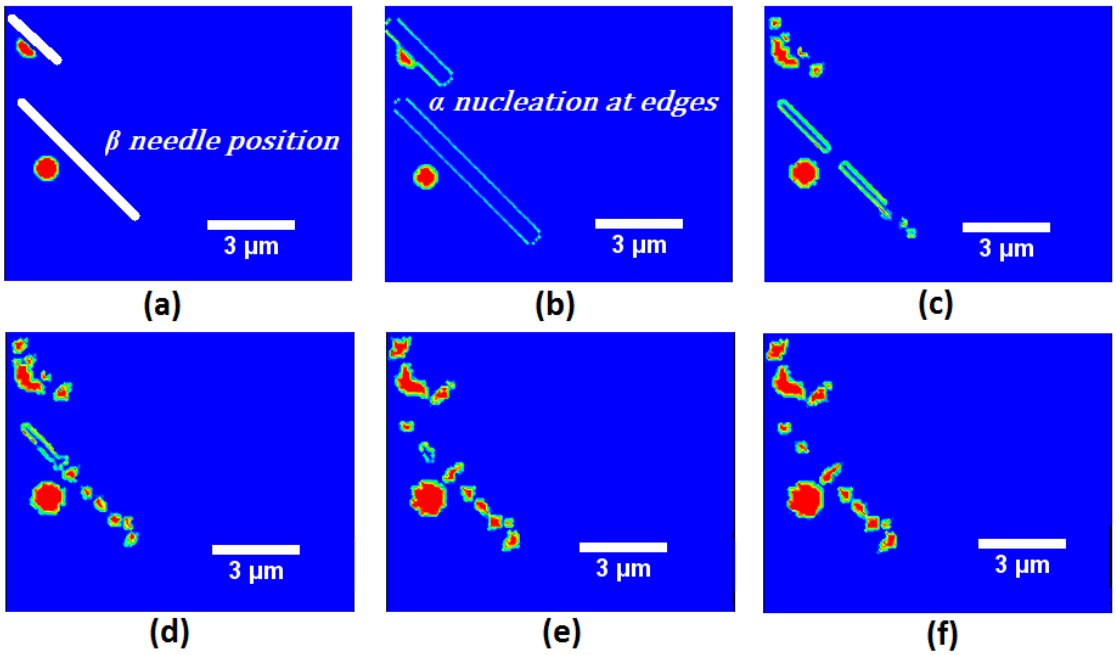

Figure 3.2: Microstructural evolution during homogenization at 580°C, showing only the α-Al(FeMn)Si (in red). (a) Initial microstructure with the position of the β–AlFeSi needles indicated by white lines; (b) at 10 mins, showing α-Al(FeMn)Si nucleation along the edges of needles of β–AlFeSi; (c) at 1 hour, showing thinning and separation of β into smaller needles; (d) at 3 hours, showing α-Al(FeMn)Si globules forming where the β dissolved; (e) at 6 hours, showing complete dissolution of β needles; and (f) at 8 hours, showing beads of α-Al(FeMn)Si where the two α-Al dendrites meet .

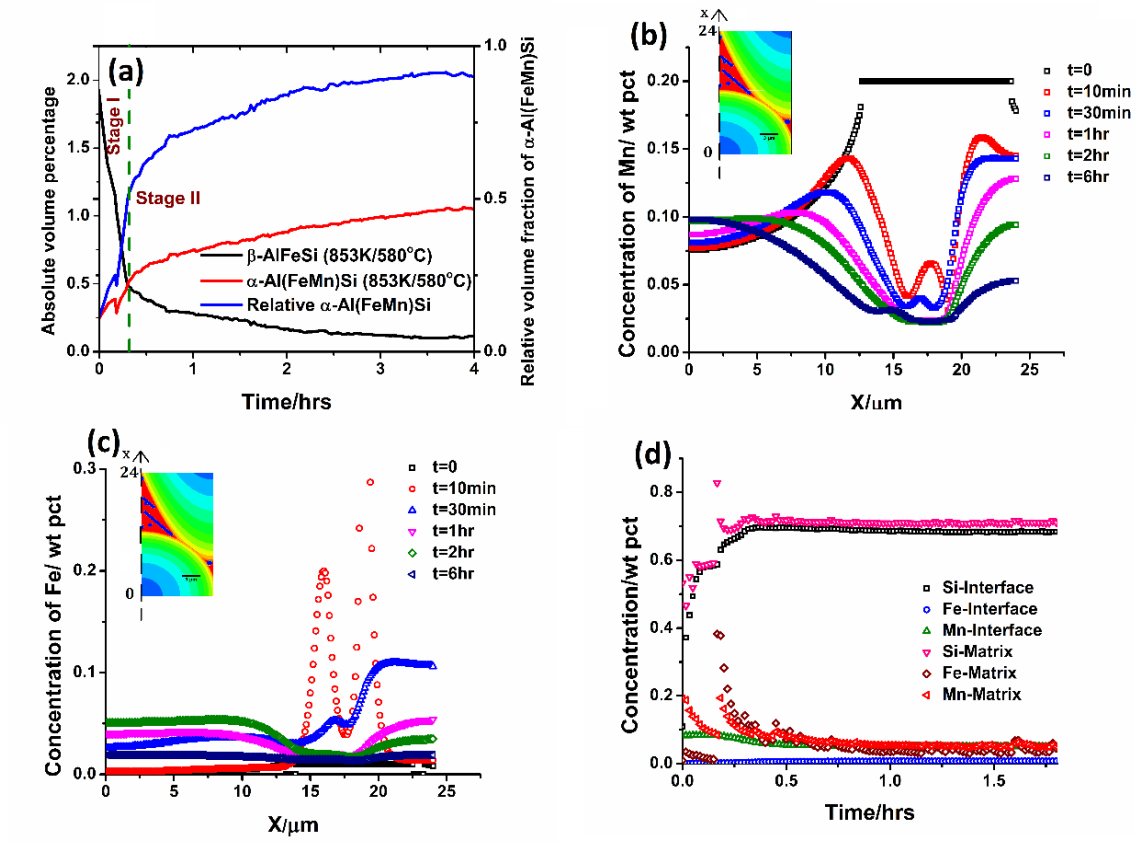

Figure 3.3: Microstructural evolution of baseline conditions. (a) Absolute volume fraction evolution of β-AlFeSi and α-Al(FeMn)Si with time, showing two stages of phase transformation. Relative α-Al(FeMn)Si volume fraction is also indicated (b) Mn and (c) Fe concentration profiles along the centerline of the microstructure (local increases at 10 minutes are due to dissolution of β-AlFeSi precipitates). (d) Compositions at the interface and matrix in the interdendritic region.

Figure 3.3(d) shows the transient compositions of Fe, Mn, and Si in the α-Al matrix, both at the interface and in the matrix locally in the interdendritic region. The fast Stage I transformation rate is driven by the initially large differences in Fe and Mn composition, while the Si composition is comparatively uniform because of faster Si diffusion. Discontinuities at 10 minutes are due to dissolution of the nucleated α-Al(FeMn)Si in partially filled cells when the β-AlFeSi phase dissolves and the partially filled cell is fully surrounded by α-Al matrix. This is a numerical artifact which can be minimized by using smaller grid sizes. The Mn and Fe compositions become more uniform around 20 min, at the transition from Stage I to II, after this time, the slow transformation rate is controlled by the small difference in Fe. The compositions tend to equilibrium concentrations at 580°C. A similar abrupt decrease in phase transformation rate has also been reported by McQueen et al.[9], which they attributed to site-saturation of nucleation (i.e., nucleation stops and transformation is driven only by the growth of the existing α-Al(FeMn)Si).

3.3.2 Effect of Temperature

In addition to the baseline at 580°C, the simulations are repeated at 540°C and 570°C, at which temperatures Thermo-Calc™ shows with lower equilibrium α-Al(FeMn)Si volume fractions and there is a strong temperature dependence of the homogenization rates. Dissolution of Mg_2Si is still fast, but slower at lower temperatures (15 minutes at 570°C and 42 minutes at 540°C compared to 10 minutes at 580°C, relative to the β-AlFeSi to α-Al(FeMn)Si transformation, consistent with previous results reported by Cai et al.[54], Kuijper[63], and Haidemenopoulos et al.[40] The rate of transformation from β-AlFeSi to α-Al(FeMn)Si is faster at higher temperatures due to increased diffusivities. The equilibrium volume fraction of β for Al-0.83Si-0.7Mg-0.27Fe-0.18Mn predicted by

Thermo-Calc™ at 540°C is very small (0.004%), and zero at higher temperatures. The equilibrium volume fractions of α-Al(FeMn)Si at these temperatures (540, 570, and 580°C) are 1.42%, 1.38% and 1.36%, marking a slight decrease in the temperature range. As seen in Figure 3.4, the evolution of relative α-Al(FeMn)Si at all three temperatures matches well with experiments from Kuijpers et al.[17] While equilibrium is not reached after 8h at 540°C and 570°C, at 580°C the volume fraction of β-AlFeSi reaches equilibrium as the relative volume fraction of α-Al(FeMn)Si approaches 1 in 8 hrs (Fig. 3.4). At higher temperatures (587°C) incipient melting[67] due to the reaction α-Al + β-AlFeSi + Si → L at may be a problem. The alloy finally melts at 600°C. For better extrudability than the as-cast structure, all of β-AlFeSi should be eliminated and α-Al(FeMn)Si which cannot be eliminated, minimized. The globular shapes of the remaining α-Al(FeMn)Si particles enhance hot ductility and surface finish during extrusion at higher temperatures.

Microstructures predicted by the model after homogenization for 8 hrs at 540°C, 570°C and 580°C are compared in Figure 3.5. The 540°C microstructure still has remnants of the β needles bounded by α-Al(FeMn)Si, while higher temperature microstructures have the α-Al matrix with mostly α-Al(FeMn)Si globules of various sizes (larger at higher temperature). In this temperature range (570-580°C), the effect of lower temperature over 8 hours is only to slow the transformation rates, as the equilibrium phase volume fractions are not a strong function of temperature. The phase transformation kinetics predicted by the model are fitted to the Johnson-Mehl-Avrami equation[68,69],

$$\Delta f_{\alpha-\mathrm{Al(FeMn)Si}} = 1 - \exp(-(kt)^n), \tag{3.1}$$

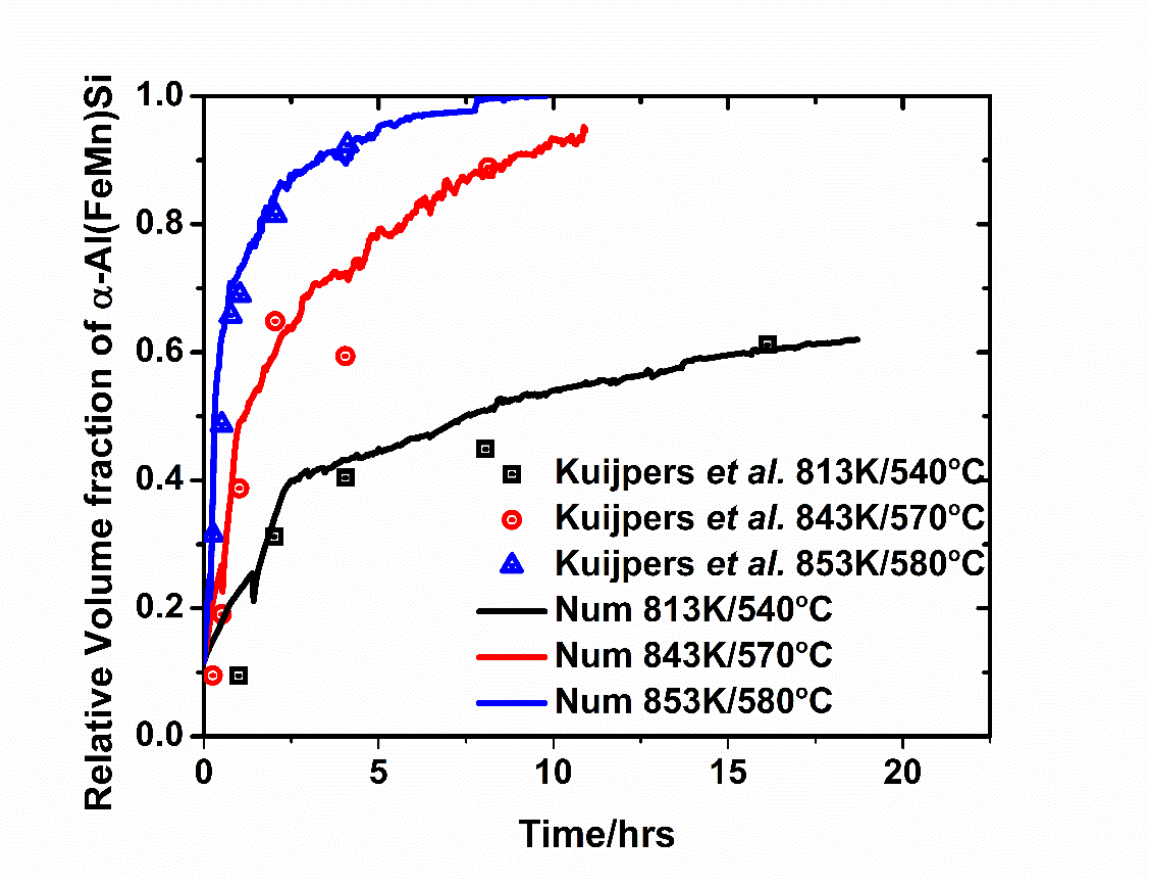

Figure 3.4: Comparison of predicted transient relative α-Al(FeMn)Si volume fraction with measurements of Kuijpers et al[17].

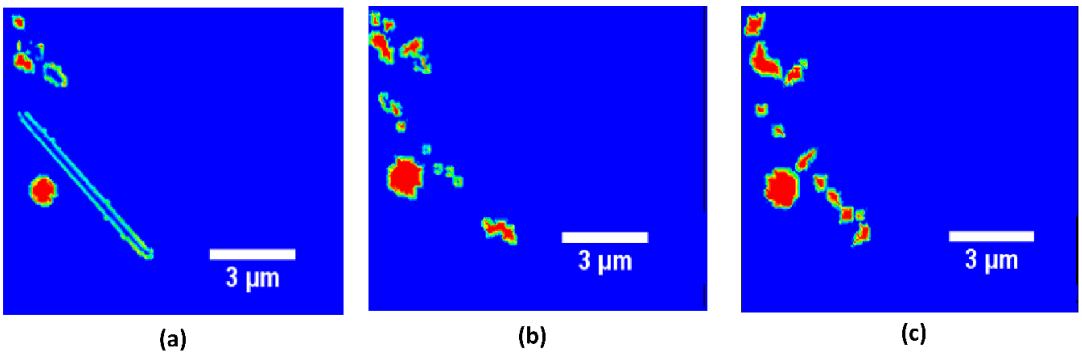

Figure 3.5: Morphology of the α-Al(FeMn)Si phase after homogenization of baseline composition for 8 hours at (a) 540°C, (b) 570°C, and (c) 580°C.

where $f_{\alpha-\mathrm{Al(FeMn)Si}}$ is the normalized volume fraction of α-Al(FeMn)Si. The Avrami exponent, *n*, increases with temperature from 0.4 to 0.65, which is in the range for diffusion controlled reactions[70]. The fit is found to be better during stage II of transformation which corresponding to when the β-AlFeSi to α-Al(FeMn)Si dominates the β dissolution.

3.3.3 Effect of Initial Alloy Composition

The effect of composition on homogenization was studied by independently varying levels of Si (0.6-1.2%), Fe (0.07-0.37%), and Mn (0.01-0.3%) from the baseline case. Here, small changes in initial alloy composition (within alloy specification) are assumed to result in the same as-cast phase volume fractions and the composition gradients are altered according to compositions predicted by Thermo-Calc™. While the composition does have some effect on phase fractions, this assumption makes easier comparisons to the baseline. The phase diagram gives equilibrium values of different phase fractions as functions of alloy composition and temperature, but the kinetics of homogenization predicted here determine how fast the metal approaches equilibrium.

Iron is usually present at some level in virgin aluminum and alloys made from recycled scrap tend to have even more. Unfortunately, iron is not a desirable component; because of its very low solubility in the α-Al phase, it forms β-AlFeSi needles which are deleterious to extrudability[3] and increases the required homogenization time, as seen in the α-Al(FeMn)Si volume fraction behavior in Figure 3.6(a). This time can be reduced by lowering Fe content, but no further significant gains are seen below 0.17% Fe, where the transformation rate of β-AlFeSi to α-Al(FeMn)Si is very high. The transformations are fast because lower Fe content in the alloy gives a higher equilibrium volume fraction of α-

Al(FeMn)Si, hence a higher driving force for transformation. Because iron is almost never removed from aluminum alloys, some way to mitigate its effect is needed. The addition of manganese to iron containing aluminum alloys allows the iron to be taken up by globular α-Al(FeMn)Si instead of the needle shaped β-AlFeSi, a change which improves surface finish and ductility of the extruded alloys[3]. It can be seen in Figure 3.6(b) that for low Mn (~0.01%), a reverse transformation of α-Al(FeMn)Si to β-AlFeSi occurs which is undesirable. Figure 3.6(b) shows that increasing Mn over the range from 0.1% to 0.3% has the opposite trend from iron, leading to a considerable decrease in homogenization time. It should be noted that lower homogenization times for high Mn may be because of higher equilibrium volume fractions of α-Al(FeMn)Si leading to higher driving force similar to low Fe cases.

The age hardenability of aluminum is improved by the addition of Si[9] and simulations were run with C^{Si} lower and higher than the baseline. Figure 3.6(c) shows the lower value of C^{Si} (0.6%) comes to equilibrium faster than the baseline (0.8%) and that trend reverses at C^{Si} = 1.2%. The increase in Si speeds transformation of β-AlFeSi to α-Al(FeMn)Si in stage I for Si content from 0.6% to 0.8% and slows it from 0.8% to 1.2%, due to initial increase and then decrease in equilibrium volume fractions of α-Al(FeMn)Si with increase in Si content. An increase beyond about 1.2% is not desirable as the alloy melts at 580°C at these high Si contents.

These predicted trends due to composition variation are valid as long as the equilibrium phases are only α-Al and α-Al(FeMn)Si; the homogenization model only simulates those phases. Other phases appear based on composition as seen in Figure 3.7. If the composition is changed to lower Si, then other, less desirable Fe-bearing phases

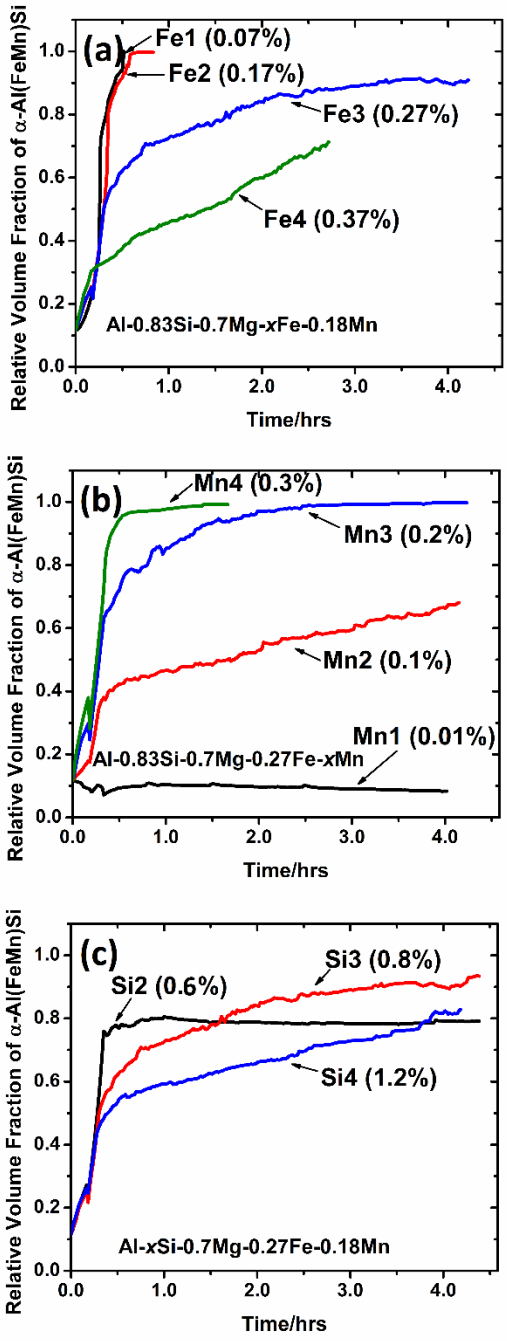

Figure 3.6: Effect of initial alloy composition on transformation to α-Al(FeMn)Si, or β-AlFeSi independently varying (a) Fe, (b)Mn, and (c) Si from the baseline.

($Al_{13}Fe_4$) appear, while an increase in silicon content much above the 1.2% shown here would cause incipient melting above 580^oC.

3.3.3.1 *Comparison with Phase Diagrams*

Figure 3.7 shows the phase diagram information with different phase boundaries which are affected by the composition of Si, Mn and Fe keeping Mg constant at 0.7%. This information is acquired from Thermo-Calc^{TM} using the TCAL1 database. Figure 15(a), (b) and (c) show effect of Si and Mn for increasing Fe compositions of 0.07, 0.27 and 0.37% respectively.

The phases favorable for extrusion are α-Al(FeMn)Si in α-Al matrix which is the phase present at higher Si and higher Mn contents. The Al_8Fe_2Si phase corresponds to the α-Al(FeMn)Si phase but has a hexagonal crystal structure as opposed to the otherwise cubic crystal structure. It has been reported for very low Mn contents (<0.01%) by Tanihata et al.[71]. This is also a favorable phase which can be attained for a Si composition ~0.6% and Mn content <0.01%. The phases which are totally undesirable are the Fe containing $Al_{13}Fe_4$ (Skjerpe[72]) and β-AlFeSi ($AlFe_2Si_2$) (Gorny et al.[73]) which are plate-like. These phases are the dominant phases at low Mn, low Si and high Fe contents. Al_6Mn is the phase present at high Mn and low Si contents in the alloy (Bahadur[74]).

If we compare the results for variation in alloying elements with the phase diagram information, we find the trends follow the phase diagram as expected. Higher Fe leads to an expansion of the $Al_{13}Fe_4$ and $Al_9Fe_2Si_2$ phase regions as can be seen in Figure 3.7(b) and (c). This is manifested by higher homogenization times from the numerical calculations.

=

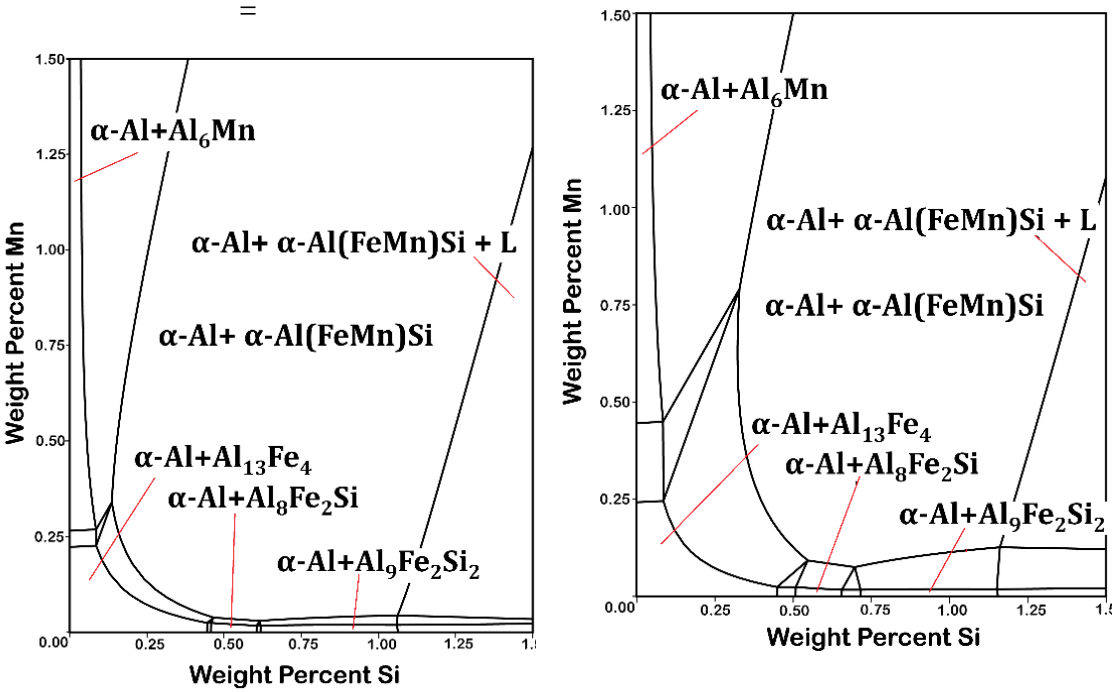

(a) (b)

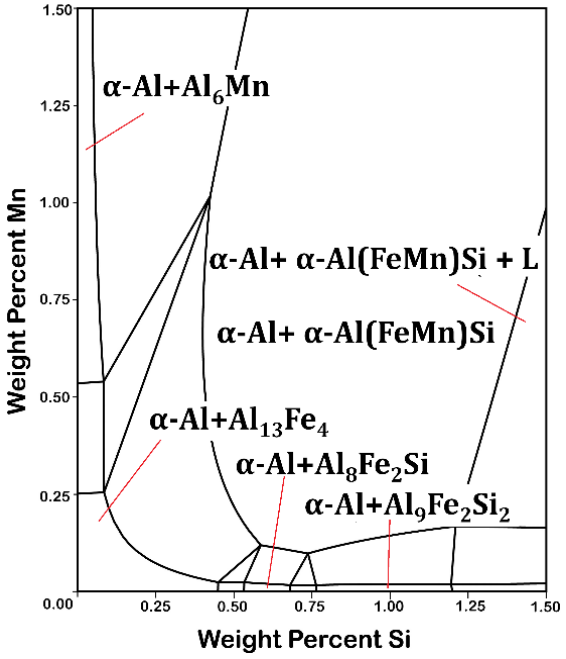

(c)

Figure 3.7: Effect of Si and Mn on the stable equilibrium phases at 580°C for Fe contents of (a) 0.07% (b) 0.27% and (c) 0.37%. The 2 phase regions are separated by 3 phase regions which are separated by 4 phase regions.

The phase boundaries do not change for Fe content <0.2% leads to saturation of homogenization times at <0.2% Fe.

On the contrary, increase in Mn leads to the α-Al(FeMn)Si + α-Al phase region manifested by lower homogenization times as seen in the results. However, no gain in homogenization time is achieved beyond 0.2% as this phase region is retained on any further increase in Mn content. The phase diagram also reveals that a very small amount of Mn addition leads to the α-Al(FeMn)Si + α-Al and Al_8Fe_2Si + α-Al phase regions which are phases favorable for extrusion.

The favorable Al_8Fe_2Si + α-Al phase region is attainable at Mn contents as low as <0.01% for intermediate Si contents of 0.5-0.6%. This phase information is manifested as an optimum Si range for Mn content <0.2% to achieve microstructure favorable for extrusion. For higher Mn contents Si content above a specific limit is favorable leading to the α-Al(FeMn)Si + α-Al phase region. On increasing Si content beyond 0.8%, into the 3 phase region of α-Al(FeMn)Si +β-AlFeSi + α-Al manifested as increase in homogenization time.

3.3.4 Effect of Initial Microstructural Features

The effect of size of microstructural features on homogenization times was investigated by independently changing β-AlFeSi needle thickness and relative α-Al(FeMn)Si volume fraction. The grid size and time step used were the same as in the baseline study. The test cases for specific variations of microstructural features are shown in Table 3.2.

Figure 3.8(a) shows the effect of β-AlFeSi needle thickness on α-Al(FeMn)Si growth, which is faster for the thinner needle thickness. Finer plates of β-AlFeSi can be

obtained by faster cooling during solidification[75], but this practice may also lead to higher overall as-cast volume fractions of β-AlFeSi[76]. Nuclei of α-Al(FeMn)Si form at the interface of β-AlFeSi and α-Al as β-AlFeSi dissolution occurs there. Finer β-AlFeSi needles lead to an increase in surface area per unit volume where these phase transformations can occur.

Initial α-Al(FeMn)Si volume fraction is varied in Figure 3.8(b), where higher levels (30%, 40%) reach the equilibrium values sooner than the 10% baseline microstructure as the starting microstructure has α-Al(FeMn)Si volume fraction closer to equilibrium value. Relative α-Al(FeMn)Si volume fractions depend on growth velocities[77,78] and cooling rates[76] during casting over a range of cooling rates found in DC casting and with and without TiB_2[75] or boron nitride[78] grain refiners.

3.4 Microstructural Evolution during Post-homogenization Quenching

The precipitation sequence of Mg_2Si during quenching involves independent clusters of Mg and Si atoms followed by co-clusters and small precipitates. These precipitates form β'' needle-shaped precipitates which transform to β' lath-shaped and rod-shaped precipitates[79]. However, this precipitation sequence is not taken into account as it would involve anisotropic shapes and surface energies. In order to simplify the problem (flux into and out of the radial control volumes) all the precipitates right from nucleation are taken as spherical with uniform thermodynamic properties including the surface energy. The quasi-binary Al-Mg_2Si phase diagram is used for tie-line calculation during nucleation and growth, reducing the complexities introduced in compositions of clusters and other metastable phases.

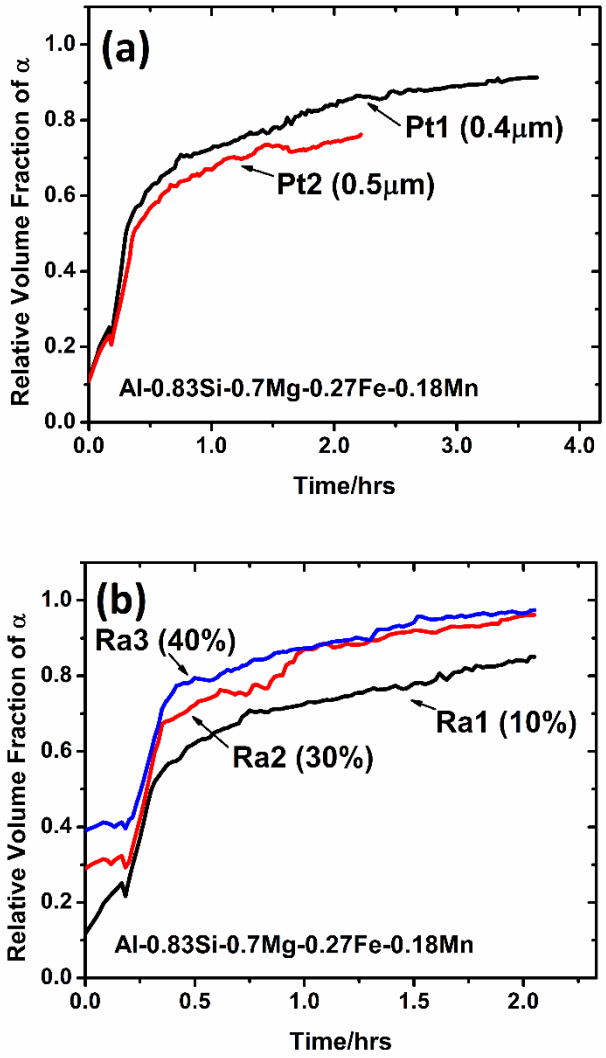

Figure 3.8: Effect of variation in size of microstructural features on homogenization times: (a) β-AlFeSi plate thickness and (b) relative α-Al(FeMn)Si volume fraction.

3.4.1 Behavior of Microstructure during Quenching from the Homogenization Temperature

Precipitation of Mg_2Si dispersoids occurs in two stages during post-homogenization cooling. The first precipitation occurs in the temperature range of 400-420°C and the second precipitation occurs at temperature range of 200-320°C as seen in Figure 3.9(a). The first precipitation stage was also reported by Birol[80]. However, he did not observe the second precipitation stage which can explained by the fact that very small clusters of Mg_2Si are nucleated during the second stage causing a little change in the Mg concentration in the matrix or volume fraction of Mg_2Si as can be seen in Figure 3.9(c) and (d). The estimation of the nucleation stages by Birol[80] were done on the basis of conductivity which seems to be unaffected by this nucleation stage.

The two nucleation stages result in a bimodal distribution of the dispersoid number density with the size of precipitates. The bimodal distribution is explained by diffusion of Mg and Si during the quench. Once the initial nucleation of Mg_2Si due to supersaturation occurs, it grows by diffusion enabled by the availability of Mg and Si from the nearby matrix. As these precipitates grow, there is a swift decrease in Mg near them in the matrix leading to an increase in the free energy needed for nucleation and decrease in the nucleation rate. At lower temperatures, however, the equilibrium Mg concentration of the matrix phase decreases drastically increasing its supersaturation level and causing the precipitation of a new batch of Mg_2Si. These precipitates cannot grow as fast as the early group because the temperature is too low for significant diffusion.

3.4.2 Effect of Cooling Rate

The effect of cooling rates was studied in the range of 150-1000°C/hr. The particle density evolution with temperature can be seen in Figure 3.9(a). Particle density increases while the mean particle size decreases with increasing cooling rates as high and early supersaturation result in higher nucleation rates leading to higher particle density and insufficient time for growth results in smaller particle sizes as seen in Figure 3.9(b).

The Mg concentration in the matrix change with temperature is shown in Figure 3.9(c) where the solubility limit of Mg with temperature is indicated by the dashed line. The Mg content in the matrix is not affected by nucleation as it involves clustering of a few atoms of Mg and Si. However, it decreases as the particles grow in size. The Mg content in the matrix after homogenization increases with increase in cooling rate raising the flow stress and making it more difficult to extrude which is undesirable. An increase in 0.1% Mg leads to an increase in flow stress of 3MPa[9] which is considerable considering the extrusion stress (~40-50MPa) used for these alloys. More Mg in the matrix implies more Si which is needed to form Mg_2Si which further increases the flow stress Increase in 0.1% Si causes an increase of 1.2MPa causing no increase for Si content >0.5% due to preferred precipitation as Mg_2Si[9].

The precipitated volume fractions of Mg_2Si increases with the decreasing cooling rate approaching the equilibrium volume fraction of 1.1% on decreasing the cooling rates for an alloy containing 0.7% Mg and 0.83% Si. A high volume fraction of Mg_2Si is desirable to reduce the flow stress during extrusion[80]. An increase in 0.1% volume fraction leads to a decrease in extrusion pressure by 8%[9]. However, higher volume fractions lead to Mg_2Si precipitates of size >1μm which are undesirable as they do not dissolve during

extrusion at typical preheat 450ºC and extrusion temperatures of 500-550ºC and decrease the age-hardenability of the alloy leading to lower alloy strength[59]. Lower cooling rates of ~250°C/hr are preferable that lead to Mg_2Si particles <1 μm in diameter but not all in the nm range which keep the flow stress of the alloy in control and dissolves during extrusion making Mg and Si available for age-hardening reactions during later processing stages.

An estimation of the temperature distribution from the center to the surface of a cooling billet would help understand the variation in microstructure in the billet during cooling. Johannes and Jowett[81] have done an estimation of the temperature distributions for finite lengths and diameters of billet on air cooling from 450°C considering a heat transfer coefficient for air of $14W/m^2K$ and all modes of heat transfer, conduction in the billet, convection and radiation at the surface of the billet. According to Johannes and Jowett[81] the cooling rates at the edge and at a distance >60cm from the edge of a cylindrical billet of diameter 5cm are 960°C/hr and 690°C/hr respectively and for a diameter of 40cm the cooling rates at the edge and >40cm from edge are 420°C/hr and 120°C/hr respectively. Also the initial cooling rate at the center and the surface of a billet of infinite length are 600°C/hr and 480°C/hr respectively for a billet 5cm in diameter and 60°C/hr and 180 °C/hr respectively for a billet 40cm in diameter.

The variation in cooling rate can cause variations in Mg present in the matrix after precipitation, size and volume fraction of the dispersoids more so along the length of the billets than in the radial direction.

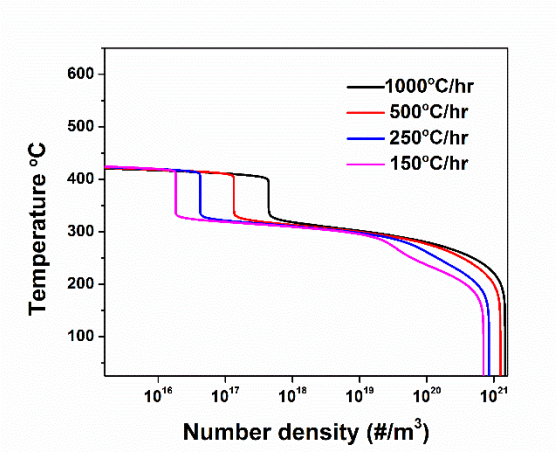

(a)

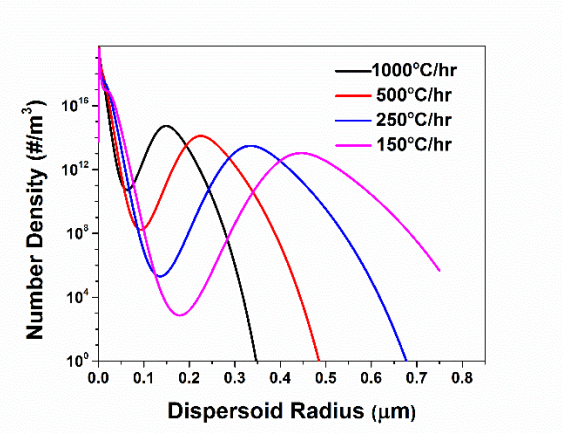

(b)

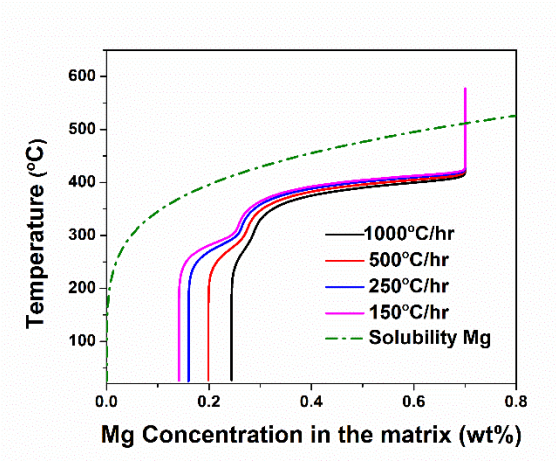

(c)

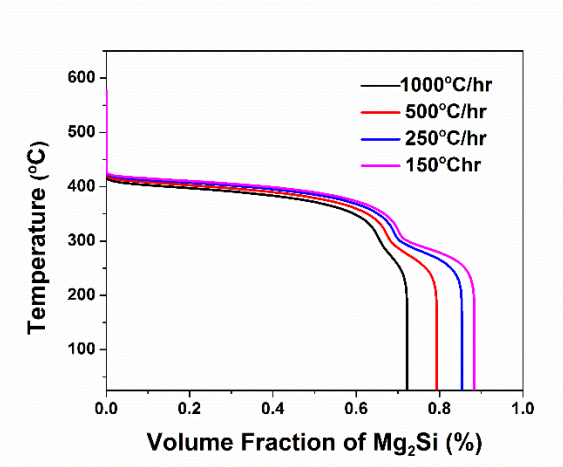

(d)

Figure 3.9: Effect of cooling rates on evolution of (a) particle density, (b) particle size distribution, (c) matrix Mg concentration, and (d) Mg_2Si volume fraction.

3.4.3 Effect of Initial Mg Composition

Results in Figure 3.10 were generated by Thermo-Calc^{TM} (TCAL1 database) and shows the effect of Mg content on phase boundaries for the baseline composition. It can be seen that at temperatures as high as the homogenization temperatures near incipient melting, only α-Al and α-Al(FeMn)Si are present for the entire Mg range studied. However, at lower temperatures, other phases including β-AlFeSi, Q, Si and Mg_2Si can form depending upon the Mg content of the alloy. These phases dissolve during high temperature homogenization, and upon subsequent cooling there is a strong driving force for (primarily) Mg_2Si precipitation[8]. The other phases may also precipitate but have been neglected in the following discussion.

The presence of Mg does not affect the volume fractions of α-Al(FeMn)Si or β-AlFeSi during homogenization but is mainly responsible for precipitation of Mg_2Si during post-homogenization cooling. Figure 3.11(a) shows the effect of Mg on the evolution of Mg_2Si particle density during cooling at a rate of 250°C/hr, from the homogenization temperature of 580°C.

Precipitation starts at temperatures below 500°C being lower for lesser Mg contents due to lower supersaturation levels (lower solvus temperature). Figure 3.11(b) shows the final particle density distribution with particle size for different Mg concentrations. It can be seen that one of the particle sizes corresponding to the highest number density lies in the nm range while the other lies in the μm range. The particle size in the μm range increases with increase in Mg content because of early nucleation. The amount of Mg in

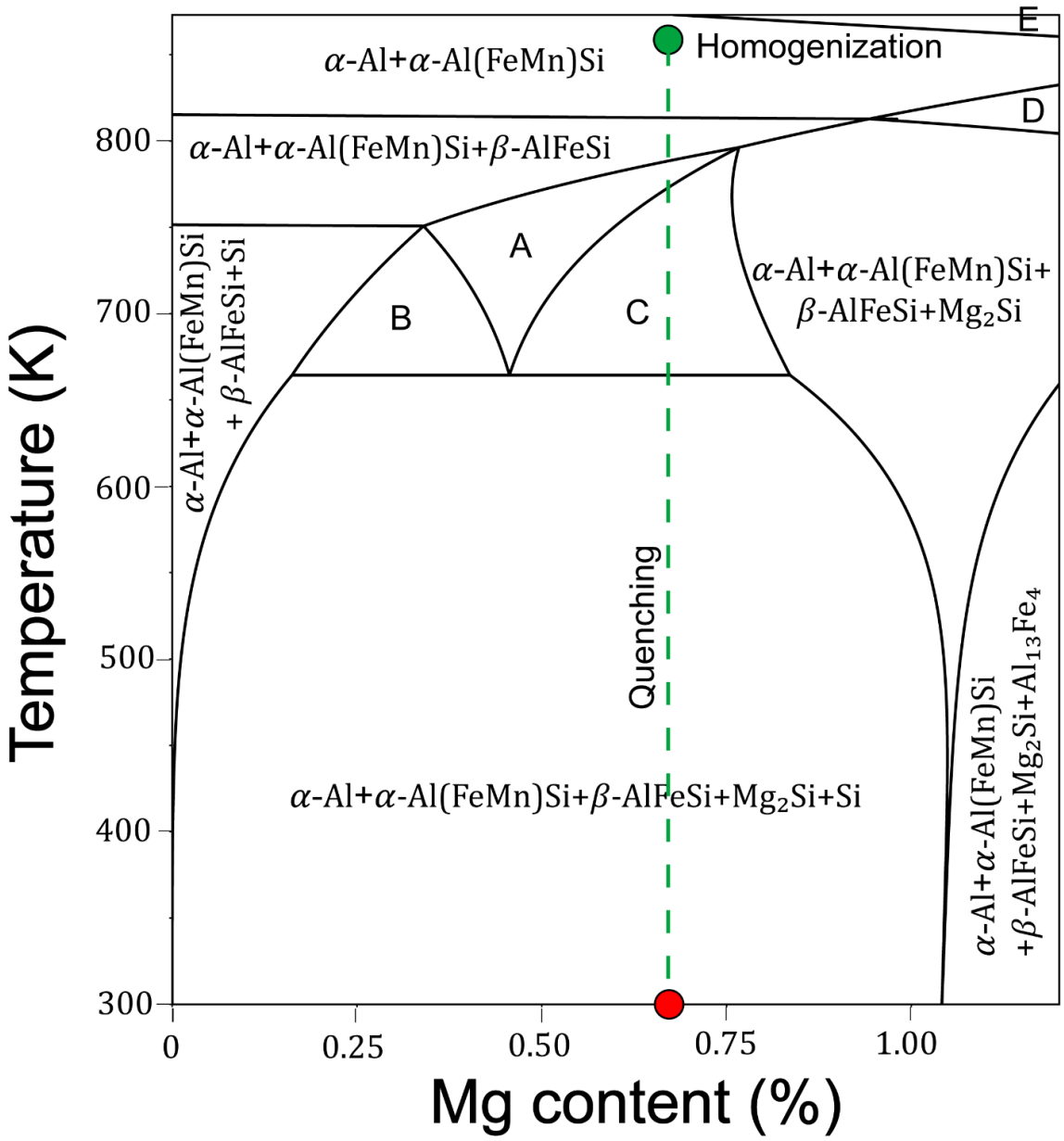

Figure 3.10: Effect of Mg on phase boundaries for the baseline composition, Phase regions A: α-Al+α-Al(FeMn)Si+β-AlFeSi+Q; B: α-Al+ α-Al(FeMn)Si+ β-AlFeSi+Q+Si; C: α -Al+ α-Al(FeMn)Si+ β-AlFeSi+Q+Mg_2Si; D: α-Al+α-Al(FeMn)Si+Mg_2Si; E: α -Al+α-Al(FeMn)Si+Liquid

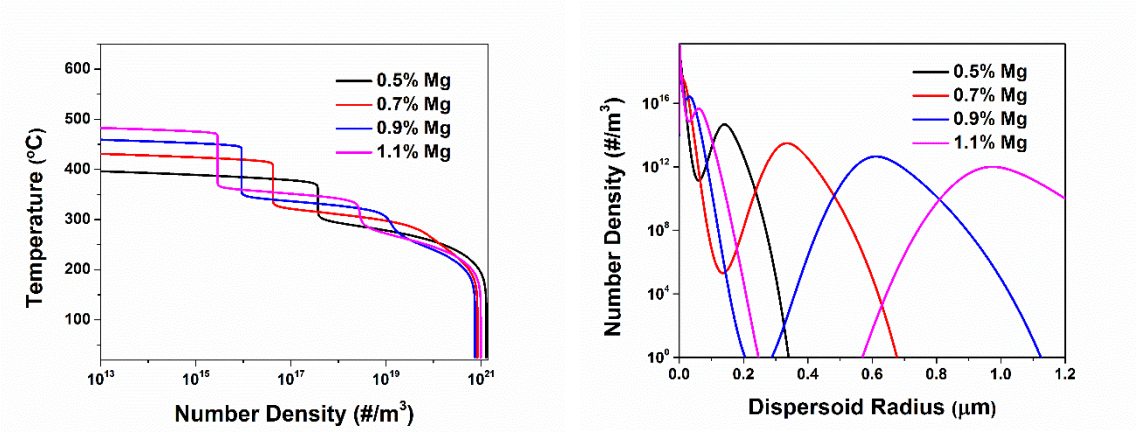

(a)

(b)

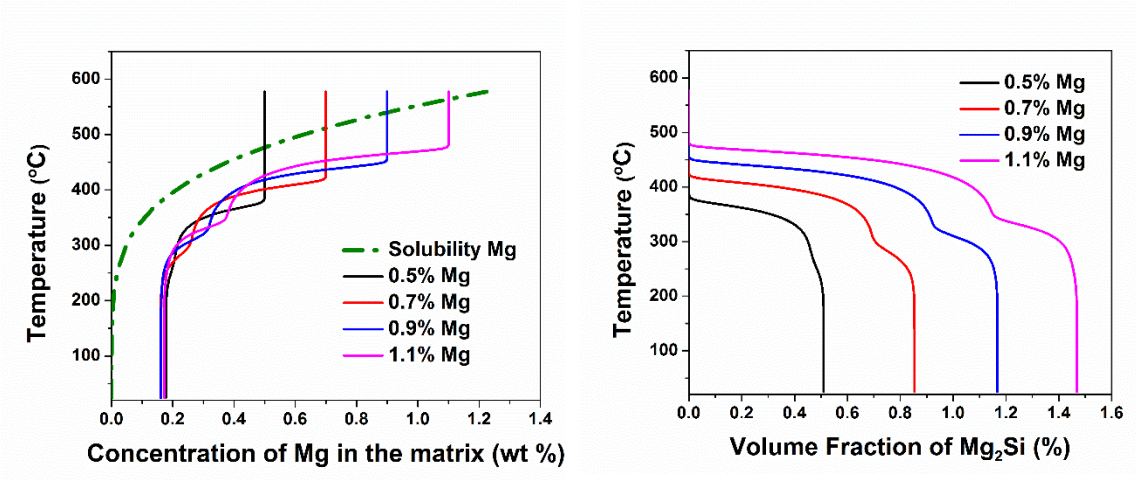

(c)

(d)

Figure 3.11: Effect of Mg on (a) particle density, (b) particle size, (c) average matrix Mg concentration, and (d) Mg_2Si volume fraction during cooling at 250°C/hr.

the matrix which determines the flow stress during extrusion seems to be minimally affected by the Mg composition of the alloy as can be seen in Figure 3.11(c) as the excess Mg in the alloy is used up in formation of larger volume fractions of Mg_2Si as seen in Figure 3.11(d).

The Mg content in the alloy does not seem to affect the amount of Mg left in the matrix. It may however affect the amount of Si left in the matrix after precipitation of Mg_2Si, which may affect the flow stress during extrusion[9]. Also very high Mg content can lead to dispersoids > 1μm in size which are difficult to dissolve during pre-heat before extrusion which are undesirable as they remain undissolved during pre-heat and hamper the age-hardenability of the alloy. Finally, the Mg/Si ratios in the 6XXX series alloys (typically >1.73)[82] are specified to optimize the final aging response, and this constraint must also be considered when selecting the Mg concentration for improved extrudability.

3.5 Process Recommendations

Homogenization at temperatures lower than 580°C requires longer times and ends with higher volume fractions of β-AlFeSi and α-Al(FeMn)Si. Homogenization at higher temperatures would further reduce the α-Al(FeMn)Si volume fractions and time required, but causes local incipient melting. Homogenization at 580°C for 8 hrs eliminates all of β-AlFeSi which transforms into globular α-Al(FeMn)Si. The final microstructure should have good ductility and not affect the extrudate surface finish.

Cooling at rates higher than 250°C/hr leads to smaller volume fraction Mg_2Si dispersoids less than 1 μm, which dissolve in the α-Al matrix during preheat before extrusion and thus increase the extrusion flow stress. On the other hand, lower cooling rates

lead to larger volume fractions of Mg_2Si dispersoids greater than 1μm. In this case, the flow stress is lower, but the Mg_2Si is difficult to dissolve during preheat, leaving less Mg and Si in the matrix to feed age hardening. The suggested cooling rate while improve the extrudability compared to the industrial cooling practice.

Using these results, homogenization at a temperature of 580°C for 8hrs and cooling at 250°C/hr are suggested for Al-0.83Si-0.7Mg-0.27Fe-0.18Mn alloy. For further improvement, this composition can be modified to $C^{Fe} < 0.17$, $C^{Mn} > 0.2$, and C^{Si} between 0.6 and 0.8, producing to a microstructure with no β-AlFeSi needles after homogenization for 8 hrs at 580°C. On the other hand, 0.5-0.7% Mg can produce Mg_2Si dispersoids which are <1 μm, with only a slight effect on extrusion flow stress. (All of these changes are still in the specification range for 6XXX series alloys.) These intermediate ranges of Si and Mg can be practiced in the industry for easily homogenizable and extrudable microstructures. Finally, homogenization time can also be decreased by refining the as-cast structure by higher solidification rates and the use of grain refiners[78].

3.6 Conclusion

Numerical models have been developed to study the microstructural evolution at the SDAS and dispersoid length scales during homogenization and post-homogenization quenching of Al-Si-Mg-Fe-Mn alloys. The models are able to predict microstructures which match experiments well. The needle-like β-AlFeSi in the as-cast microstructure transform into globular α-Al(FeMn)Si during homogenization, while Mg_2Si dispersoids precipitate during post-homogenization. These phase transformations are diffusion controlled processes. While Fe and Mn composition differences between the matrix and phase interface drive the initial stage of the homogenization phase transformation, only Fe

composition differences influence the later stage. A closer look at the diffusion lengths (Mn: 1.8 μm; Fe: 6.6 μm; Si: 39 μm for t=0.5 hr) indicates Mn is the slowest diffusing element which transfers from the matrix to the α-Al(Fe,Mn)Si in Stage I mostly while the transfer of the next slowest element Fe from the β-AlFeSi to matrix mostly happens in Stage II. Transfer of Fe from β-AlFeSi to α-Al(Fe,Mn)Si also occurs, in both the stages. The Mg_2Si precipitates during quenching, driven by Mg supersaturation in the matrix. Alloy compositions and processing conditions likely to give improved extrudability and age-hardenability are suggested.

CHAPTER 4. MICROSTRUCTURAL EVOLUTION DURING HOMOGENIZATION OF AL-ZN-CU-MG-ZR ALLOYS

4.1 Introduction

Aluminum alloys of Al-Zn-Cu-Mg-Zr (AA7XXX) are commonly used in aerospace applications due to their high specific strength, good fracture toughness and corrosion resistance[83,84]. The combination of properties come from the chemistry of the alloy and the mechanics of precipitation strengthening. The as-cast alloy consists of the coarse interdendritic phases which are detrimental to mechanical properties[12]. The as-cast coarse particles and microsegregation in the primary α phase are reduced during homogenization, while precipitation of coherent Al_3Zr dispersoids also occurs. Recrystallization during deformation processing and solution heat treating[85] which may degrade mechanical properties is reduced by the presence of Al_3Zr[16]. Furthermore, large undissolved particles above a critical size limit may stimulate recrystallization[15], and hence such particles should be eliminated. Thus homogenization involves changes in microstructure at the grain size (SDAS) and the dispersoid length scales, all of which affect properties during and after subsequent processing, underlining the importance of this processing step.

As-cast Al-Zn-Cu-Mg-Zr alloys consist of compositional variants of the η ($MgZn_2$) or the T ($Al_2Mg_3Zn_3$) as coarse interdendritic particles which transform to the S phase (Al_2CuMg) during homogenization[2,10,86]. Jia et al.[12] reported nucleation of S phase at edges

of the T phase leading to formation of diffusion networks. The η phase and Cu and Mg rich non equilibrium aluminides transform to S which gradually dissolves on further homogenization as reported by Deng et al.[2] in AA7050. The alloy is fully homogenized when the interdendritic volume of η, S and T phases is minimized and numerous fine Al_3Zr dispersoids precipitate across the grain.

The processing parameters and compositions which improve the homogenization treatment and microstructure are complex to pin down to because of the complexities of the phase transformations occurring. Along with the dissolution and transformation of the interdendritic particles, the precipitation of Al_3Zr dispersoids occurs across the grain, during homogenization. Numerical modeling of simultaneous phase transformations at both the length scales makes it easier to study and optimize the process and compositions.

The diffusion based model worked well for the 6XXX series alloys which were homogenized at high temperatures in the range of 540-580°C. However, homogenization of 7XXX series alloys is done at lower temperatures of 450-480°C due to low melting temperature (475°C) of the eutectic. An attempt was made to simulate the η ($MgZn_2$)/ T ($Al_2Mg_3Zn_3$) to S (Al_2CuMg) phase transformation in 7XXX series alloy similar to the β-AlFeSi to α-Al(FeMn)Si transformation in 6XXX series alloys. The microstructures predicted by the model resemble the experimentally found microstructures[12]. Diffusion networks were observed in the η phase and circular S phase precipitates precipitated out in the interdendritic regions as can be seen in Figure 4.1(a) and (b). However, the diffusion-based model predicted homogenization times which were 1 order of magnitude smaller than that experimentally observed by Fan at al.[11] as seen in Figure 4.1(c).

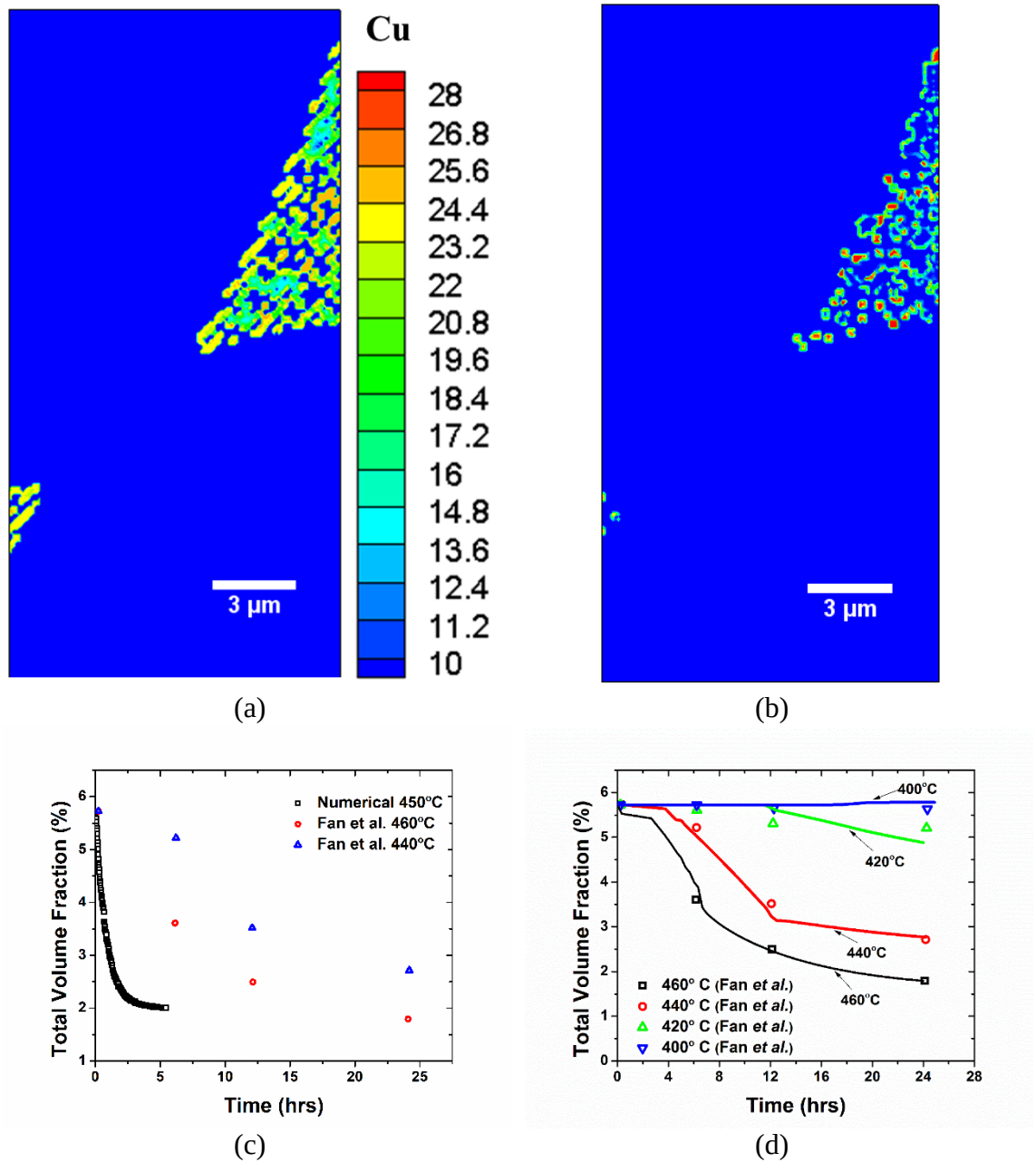

Figure 4.1: (a) Predicted composition diffusion network in the interdendritic particles as predicted by the diffusion based model as observed by Jia et al.[12]; (b) The predicted microstructure of spherical S phase (in red) nucleated on the interdendritic η during homogenization; (c) the comparison of homogenization times predicted by the diffusion-based model with experiments by Fan et al.[11] (d) comparison with predictions from the interface-reaction rate control based model with experiments from Fan et al.[11]

The results from the diffusion based model implied diffusion was not the slowest step at these temperatures and the transformation was interface reaction controlled where the transfer of atoms at the interface was slower than their diffusion in the matrix. The diffusion based model was modified to include the effect of interface mobility on the evolution of the phases. The interface reaction rate control based model was able to predict the kinetics well as shown in Figure 4.1(d). This model was coupled with the precipitation model to get a comprehensive picture of microstructure at both the length scales. This model was validated against laboratory-scale experiments. The improved homogenization schedule was proposed.

4.2 Domain Description

The transformation of the interdendritic η and S is modeled using the CA-FV model discussed in CHAPTER 2. The numerical domain representing half the grain consists of 10 cells (control volumes) with concentrations in each pertaining to Gulliver-Scheil [64] solution during casting predicted as by Thermo-Calc™. The position of the domain with respect to an equiaxed grain is represented in Figure 4.2(a). Cell 1 includes the area near the grain boundary with the interdendritic phases, whereas cell 10 is positioned at the center of the grain. Cells 2-10 are entirely the α-Al matrix phase, while Cell 1 has the interdendritic region, including a phase fraction of η + S phases between 0 and 1, with the remaining being α-Al as shown in Figure 4.2(b).

In every time step, changes in η and S phase fractions are calculated. The amount of solute rejected or absorbed in the process is distributed in the neighboring cell 2 as described by Krane et al.[45] (In that work, solute was redistributed to only one phase, the liquid, and here only to the α phase.) The concentration gradient developed at the interface

in the interdendritic cell 1 and neighboring cell 2 is levelled by the diffusion process in each time step. The grid size $\Delta x=10^{-6}$m and $\Delta t=375$s at 480°C.

Transformation and dissolution of the interdendritic phases (η and S) during homogenization is accompanied by precipitation of nanosized, coherent dispersoids of metastable L_{12} Al_3Zr throughout the primary α phase. This process is modeled as in Myhr and Grong[55], by calculating the distribution of dispersoid number density (N) over dispersoid size (r), as shown in Figure 4.3(b). The control volume size is $\Delta r = 10^{-10}m$ and time step $\Delta t_{sub} = 75\ s$ at 480°C. This size distribution tracking is carried out in each of the 10 cells of the half-grain domain as shown in Figure 4.2(b).

The values of various parameters used by the precipitation model required by the model are listed in Table 4.1.

Table 4.1: Values of parameters for the precipitation model.

Parameter	Value
Molar volume of Al_3Zr, V	10^{-5} m^3/mole
Interfacial energy of α-Al/Al_3Zr, γ	0.816 J/m^2
Lattice parameter of Al, a	4.08×10^{-10} m
Number of nucleation sites, N_{max}	1.5×10^{-21}
Wetting angle, θ	45°

4.3 Experimental Procedures

The numerical predictions of the model were compared to experimental observations in as-cast and homogenized samples. An aluminum alloy (Al-6.2Zn-2.3Cu-2.35Mg-0.13Zr, in

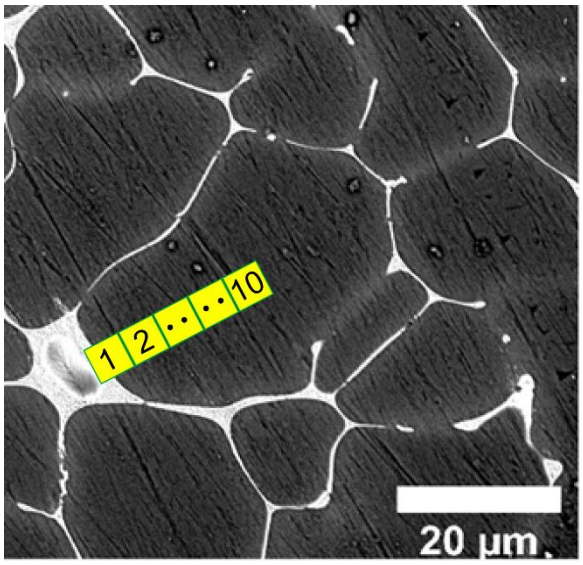

(a)

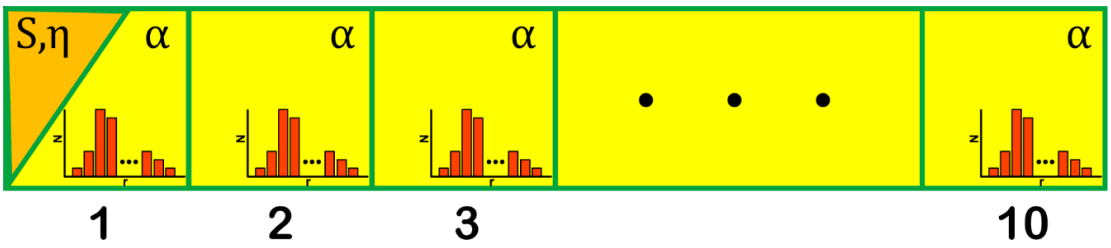

(b)

Figure 4.2: (a) A sample as-cast microstructure with a schematic of the computational domain superimposed over half an α-Al grain. (b) Schematic of half grain domain showing coupling of the two models: homogenization model with phase change in cell 1 and diffusion across the grain and precipitation model in each cell in the half grain.

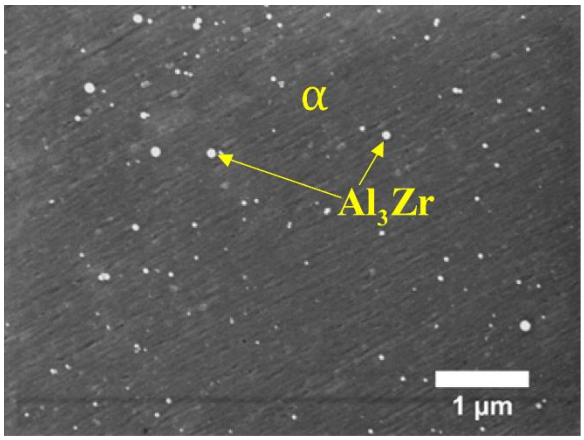

(a)

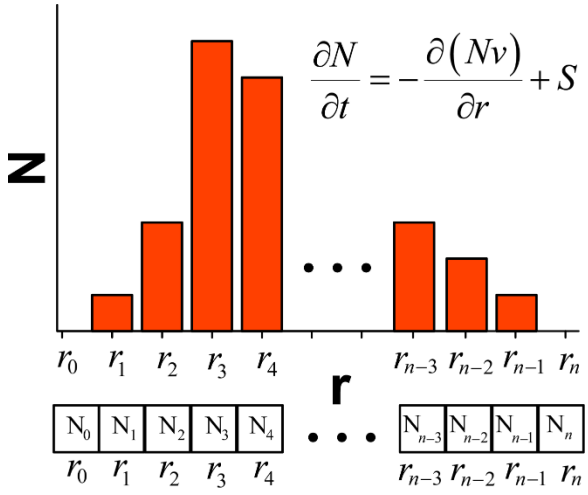

(b)

Figure 4.3: (a) A sample homogenized microstructure showing the Al_3Zr dispersoids in α-Al matrix. (b) Schematic of 1D radial domain showing size distribution of dispersoids across the radial domain

wt%) meeting the commercial specification for AA7050 was induction melted and cast. High purity starting materials were used to eliminate the presence of Fe-containing intermetallic phases and were melted and mixed in an argon atmosphere to minimize gas porosity. The as-cast cylindrical samples (L = 10 cm, D = 2.5 cm) were homogenized on different schedules in a box furnace and then polished for microscopic characterization using a FEI XL40 Scanning Electron Microscope and Phenom desktop SEM. Energy Dispersive X-Ray Spectroscopy was used to determine the presence of secondary phases and measure the composition at different positions in the α-Al grain. The volume fraction of the secondary phases at the grain boundary was calculated by analysis of SEM images using the counting grid technique. The number density and mean radius of the Al_3Zr dispersoids were calculated by image analysis of the SEM images using ImageJ. The 2D number density (areal) and mean radii was converted to 3D(volume) data using Schwartz-Saltykov stereological method[87]. The areal size distribution was divided into small bin sizes, Δ. The volume number density of a particular size class, *j*, $(N_V)_j$ was dependent on ate areal number density, $(N_A)_i$ excluding the contribution to this size class from all the larger precipitates expressed as:

$$(N_V)_j = \frac{1}{\Delta}[\alpha_i(N_A)_i - \alpha_{i+1}(N_A)_{i+1} - \alpha_{i+2}(N_A)_{i+2} - \ \ldots\ldots\ldots\ldots - \alpha_k(N_A)_k] \qquad (4.1)$$

where, *i* and *j* are integer values between 1 to *k*, *k* being the total number of bins.

X-Ray Diffraction using a Bruker D8 Diffractometer and Differential Scanning Calorimetry (DSC) using a TA Instruments Q1000 Differential Scanning Calorimeter were used to characterize the phases present after each homogenization schedule. The DSC was

performed on the as-cast and homogenized samples using Al pans and a heating rate of 30°C/minute in an argon atmosphere.

4.4 Evolution of Microstructure

4.4.1 Initial Microstructure of the Baseline Composition

The numerical model predicts time evolution of volume fraction of interdendritic η and S phases, composition profiles across the grains, number densities and size distributions of Al_3Zr dispersoids across the grains for different homogenization schedules. The model is provided with an idealized initial microstructure resembling an as-cast Al-6.2Zn-2.3Cu-2.35Mg-0.13Zr (wt%) alloy. The 10 μm long domain is a one dimensional representation of half a grain, with η phase at the grain boundary. This boundary region is represented by the first cell in the 1D domain and includes both η and α-Al. The composition distribution of various alloying elements across the α-Al grain was predicted by Themo-Calc^{TM}, assuming Scheil conditions, and is shown in Fig. 4.4. Zn, Cu and Mg have partition coefficients less than 1 and thus show a composition increase from center to the grain boundary, whereas Zr has the opposite trend due to a partition coefficient (k_{Zr}) greater than unity (k_{Zr}= 1.4). Real as-cast microstructures of Al-Zn-Cu-Mg-Zr alloys may sometimes contain S phase in small quantities[2], but it has been neglected in the initial conditions. The composition of the η phase (Laves phases in Thermo-Calc^{TM}) is taken from predictions by Themo-Calc^{TM} to be Al-41.5 Zn-32.4 Cu-20.7 Mg with a f_η = 0.0572 over the entire domain. (While the stoichiometric composition of η is $MgZn_2$, the phases calculated in ThermoCalc^{TM} and represented by η, all have the same crystal structure and wide solid solubility of Zn, Cu, and Mg.)

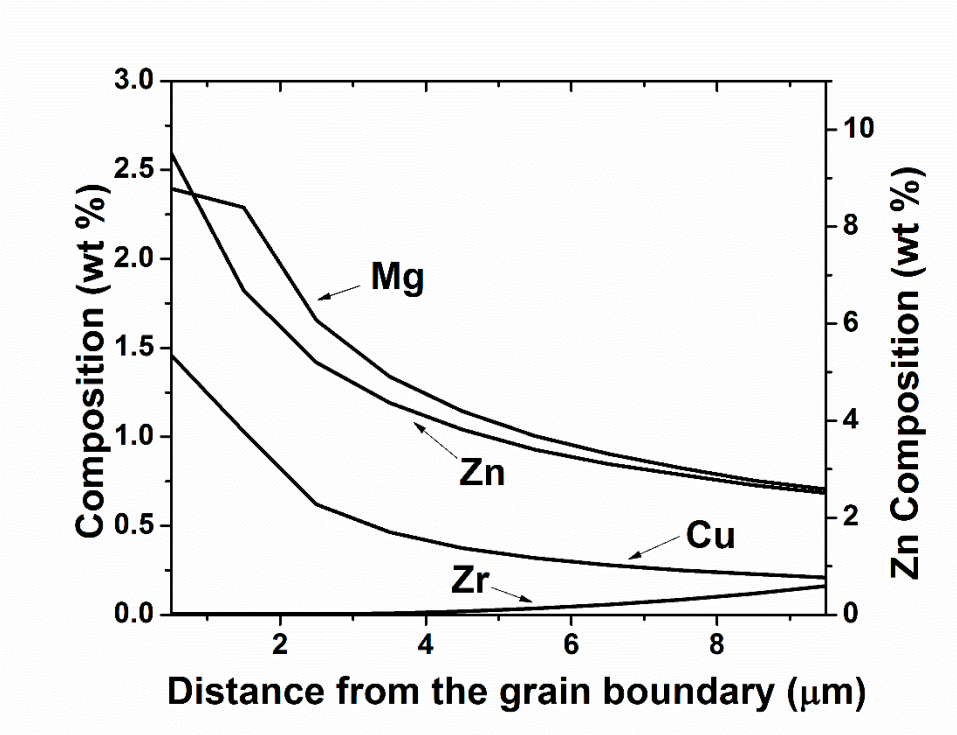

Figure 4.4: Initial composition on the half grain domain, showing the as-cast, Scheil-type microsegregation predicted by Thermo-Calc™ for Al-6.2Zn-2.3Cu-2.35Mg-0.13Zr.

4.4.2 Comparison of Homogenization Schedules for Precipitation of Al_3Zr Dispersoids

Dispersoids of Al_3Zr in Al-Zn-Cu-Mg-Zr alloys are important as they pin grain boundaries and inhibit recrystallization during extrusion and solution heat treatment[85]. Recrystallization can be prevented by a sufficient volume fraction of coherent dispersoids, small enough in size to exert a Zener drag pressure, P_Z which can be expressed mathematically as[88]:

$$P_Z = \frac{1.5f\gamma}{r} \tag{4.2}$$

However, the number density and volume fraction of the dispersoids across the grains is not uniform due to microsegregation during casting. The Al-Zr system is a peritectic

system with partition coefficient for Zr >1 (k_{Zr}~1.4), causing lower concentrations of Zr in regions near the grain boundaries as shown in Figure 4.4. The Zr concentration can be low enough to cause a dispersoid-free zone in that region. It is difficult to prevent recrystallization in these dispersoid-free zones[16].

The aim of this study is to evaluate homogenization at different temperatures for different times to determine an optimized homogenization schedule for AA7050 alloy. We will specifically compare the number densities, mean radius and volume fraction to mean radius ratios along the length of the SDAS for three schedules: (i) single step homogenization; (ii) multistep homogenization and (iii) slow heating to the homogenization. The model is different from previous studies as it includes a multicomponent model of dispersoid nucleation and growth and considers simultaneous transformation of the η to S, redistribution of alloying elements, and the nucleation and growth of the Al_3Zr dispersoids leading to realistic nucleation and growth rates and microstructures.

Three different types of homogenization schedules are evaluated for maximum number density and minimum dispersoid radius to get f/r ratios above the critical value to avoid recrystallization. The different test cases that were run are provided in Table 4.2. For the SSH and TSH schedules, the homogenization temperatures are reached instantaneously involving no ramp from the room temperature. Same is true for SHH to reach 300°C after which there is a slow ramp.

Table 4.2: Homogenization schedules for different test cases run

	Homogenization schedule
SSH1	Single step homogenization at 420°C
SSH2	Single step homogenization at 450°C
SSH3	Single step homogenization at 470°C
SHH1	Slow heating from 300°C to 475°C at 5°/hr followed by homogenization at 470°C
SHH2	Slow heating from 300°C to 475°C at 10°/hr followed by homogenization at 470°C
SHH3	Slow heating from 300°C to 475°C at 20°/hr followed by homogenization at 470°C
TSH1	Two step homogenization: 380°C and 470°C
TSH2	Two step homogenization: 400°C and 470°C
TSH3	Two step homogenization: 420°C and 470°C

4.4.2.1 *One-step Homogenization*

The most straightforward schedule for 7XXX series alloys is to homogenize at a single temperature at which the η to S phase transformation and their dissolution is fast. With these phases melting at temperatures above 475°C, it seems that the alloy should be heat treated below that temperature for fast elimination of the η and S phases without forming liquid. Such a homogenization schedule would save both time and cost for the heat treatment. However, the dispersoids formed near this incipient melting temperature coarsen very fast, which could be minimized by lowering the homogenization temperature at the cost of time needed to eliminate the interdendritic phases.

Homogenization at the temperature of 470°C and the lower temperatures (420°C and 450°C) was simulated. Figure 4.5(a) and (b) show the evolution of number density and

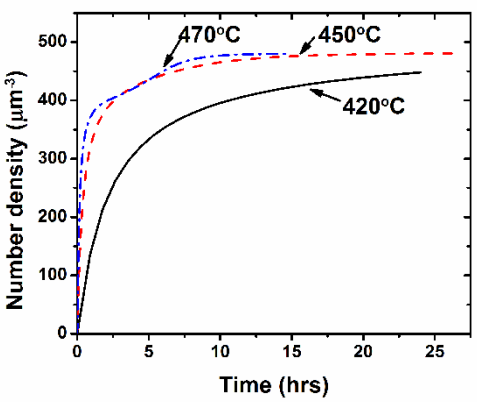

(a)

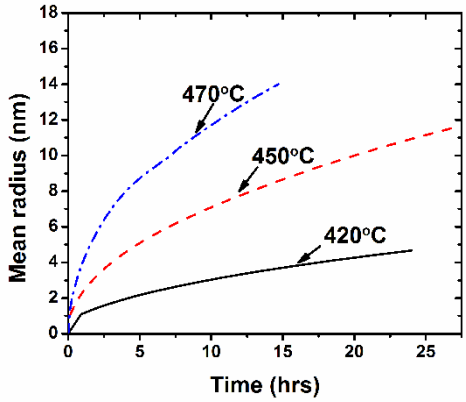

(b)

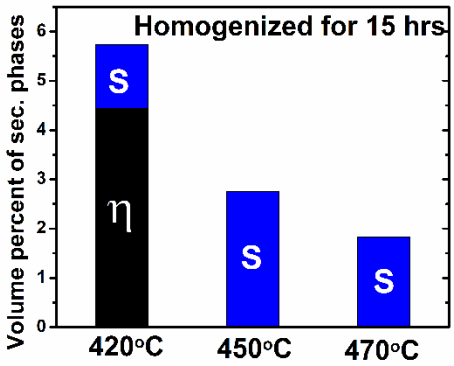

(c)

Figure 4.5: Evolution of (a) number density; (b) mean radius of dispersoids and (c) remnant volume fraction of secondary phases during single step homogenization at different temperatures.

dispersoid radius with time at these 3 temperatures, respectively. There is a steep increase in the number density initially which saturates later on. Because of faster diffusion of Zr in Al at higher temperatures, the saturation is faster. There is little difference in the saturated number densities at these three temperatures but the mean dispersoid radii are different at these temperatures. While the growth of dispersoids is very slow at 420°C, it is relatively rapid at 470°C due to faster diffusion of Zr in Al.

It might seem that lower temperatures are ideal for homogenization as the dispersoids are smaller in size. However, η to S phase transformation is very sluggish at lower temperatures. The equilibrium volume fraction of the η and S phases are also higher at lower temperatures so not all of those are eliminated. While all the η transforms to S at 470°C this is not true at 420°C as seen in Figure 4.5(c). The segregation existing in the as-cast microstructure also is removed more slowly at lower temperatures.

4.4.2.2 *Slow Heating*

Because number density evolution is faster and mean radius coarsening is slower at lower temperatures while elimination of microsegregation and η/S phases is faster at higher temperatures, slow heating to homogenization temperatures of 470°C seems to be a viable homogenization schedule which is also more realistically attainable in practice. In this work three, different ramp rates of 20°/hr, 10°C/hr and 5°/hr are evaluated to form an industrially acceptable microstructure in a reasonable amount of time.

Figure 4.6(a) and (b) show the evolution of number density and mean radius of dispersoids with time respectively, at different heating rates between 5-20°C/hr. The number density increases very slowly initially after which it accelerates until it gradually

saturates.Figure 4.6(a) and (b) show the evolution of number density and mean radius of dispersoids with time respectively, at different heating rates between 5-20°C/hr. The number density increases very slowly initially after which it accelerates until it gradually saturates. The initial number density curve is steeper for faster heating rates because of the rapid increase in temperature. As more time is spent at lower temperatures (400°C-425°C) where increase in number density is considerable, the number densities at lower heating rates is higher. It can be seen that the saturated number density at 470°C is higher at lower heating rates. The mean radius evolution shows a trend different from the number density. It increases very slowly at low temperatures gradually increases parabolically in the temperature range 400°C to 450°C and then increases linearly above 450°C to 475°C. The growth rate is higher at high temperatures owing to higher diffusion leading to very rapid coarsening of the dispersoids.

While faster heating rate may seem to be an attractive homogenization schedule option as far as mean radius of dispersoids is concerned, the number densities for the three cases are comparable. However, we should also keep in mind the time taken to eliminate the η and S phases. The predicted volume fractions of η and S phases remaining at 470°C in the alloy are, 4.12% and 0.83%; 2.53% and 1.15%, and 0% and 2.47% at heating rates of 20°C/hr, 10°C/hr and 5°C/hr respectively. It can be seen that slower heating rates lead to more transformation of η to S phase, which can be eliminated in a shorter time when compared to faster heating rates, during holding at 470°C. So an intermediate heating rate seems to be an answer to having a distribution of fine dispersoids with a high number density as well as more η to S phase transformation.

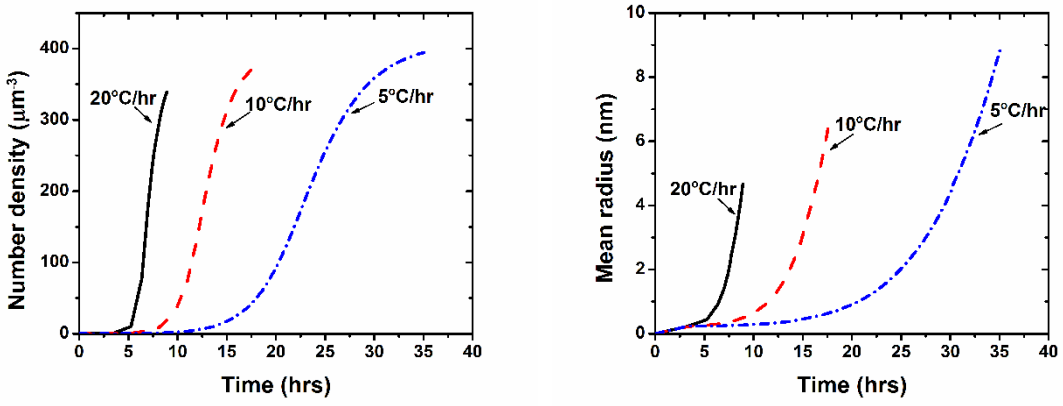

(a) (b)

Figure 4.6: Evolution of (a) number density and (b) mean radius of dispersoids with time during slow heating from 300°C to 475°C at different heating rates.

4.4.2.3 *Two-step Homogenization*

To take advantage of the faster nucleation rates at lower temperatures (400-450°C) and faster η to S phase transformation and dissolution at higher temperatures (450-475°C), it would be useful to evaluate a two-step homogenization treatment schedule, consisting of a lower temperature stage for dispersoid nucleation followed by a higher temperature stage for interdendritic phase dissolution. Here, we have evaluated 3 homogenization schedules: (i) holding at 380°C for 35 hours followed by 470°C for 15 hrs; (ii) holding at 400°C for 20 hours followed by 470°C for 15 hrs; and (iii) holding at 420°C for 10 hours followed by 470°C for 15 hrs.

Figure 4.7(a) and (b) show the time evolution of number density and mean radius of the dispersoids for the above-mentioned homogenization schedules. The number density of the dispersoids increases steadily, approaching saturation during the first step. There is a steep increase in dispersoid production rate at the beginning of the second step. The

number density then proceeds towards saturation. The mean radius of the dispersoids show a similar trend during the first step, however at higher temperatures the mean radius increases steeply and continues to do so after 10 hrs. Both the number density and mean radius of the dispersoids during the first step is higher at higher temperatures. However, there is little difference in the final number density and mean radius of the dispersoids after the second step at 470°C for 15 hrs.

As there is no difference in the final number density and mean radius after 10 hrs of holding at 470°C, the factor that differentiates the schedules is the time taken to eliminate the η and S phases. Most of the S phase dissolves at 470°C, leaving 0.95%, 0.92% and 0.89% η for first step at 380°C, 400°C and 420°C, respectively. So, holding at 420°C for the first step seems to be a time and energy saving step due to more η to S phase transformation.

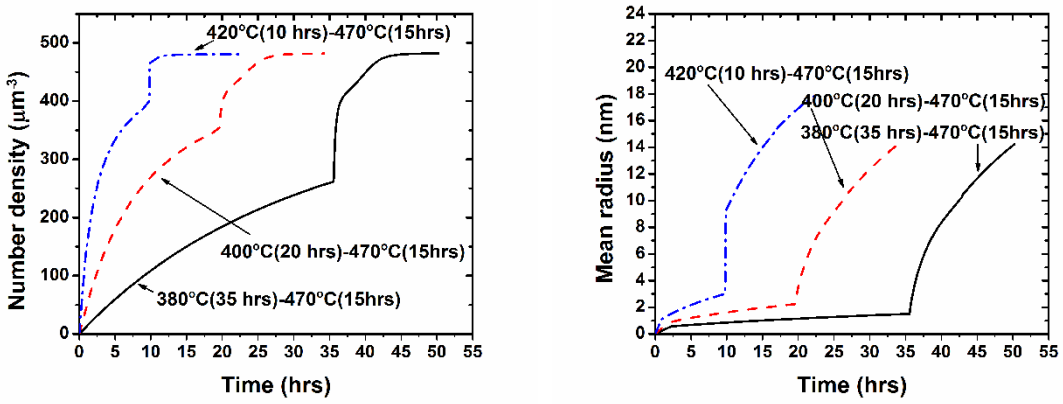

(a) (b)

Figure 4.7: Evolution of (a) number density and (b) mean radius of dispersoids with time during two step homogenization.

4.4.2.4 *Comparison of f/r for Different Schedules*

To inhibit grain boundary movement and minimize recrystallization, the dispersoids must exert enough Zener pressure, which is proportional to the volume fraction and depends inversely on the mean radius of the dispersoids (eqn. 4.2). An optimized homogenization schedule can be determined after evaluating the Zener pressure by the precipitated dispersoids. It should however, be kept it mind that there is a variation of Zr concentration from the center to the edge of the grain leading to variation in volume fractions and mean radius from the center to the edge of the grain. To be able to evaluate the best homogenization schedule we should have a look at the f/r ratio variation from the center to the edge of the grain. Figure 4.8(a) shows the variation of f/r ratios along the SDAS for one test case from each homogenization schedule.

Comparison of f/r ratios for the three homogenization schedules in Figure 4.8(a) shows that f/r ratios for slow heating and two step homogenization are comparable and both are better than the single step homogenization. Two step homogenization is slightly better than slow heating. Two step homogenization provides the best recrystallization resistance across the grain. It is also the most cost and energy efficient schedule as it takes less time to remove microsegregation and dissolve the interdendritic phases as seen in Figure 4.8(b). Next we try to study the two-step homogenization process in detail and try to improve on it to make time efficient in terms of dissolution of the secondary phases too.

4.4.3 Evolution of Composition Profiles during Homogenization

The composition profiles of Cu across the grain at different times during homogenization of the as-cast alloy at 450°C predicted by the numerical model and from the EDS measurements are shown in Figure 4.9. Of the four elements tracked by the model

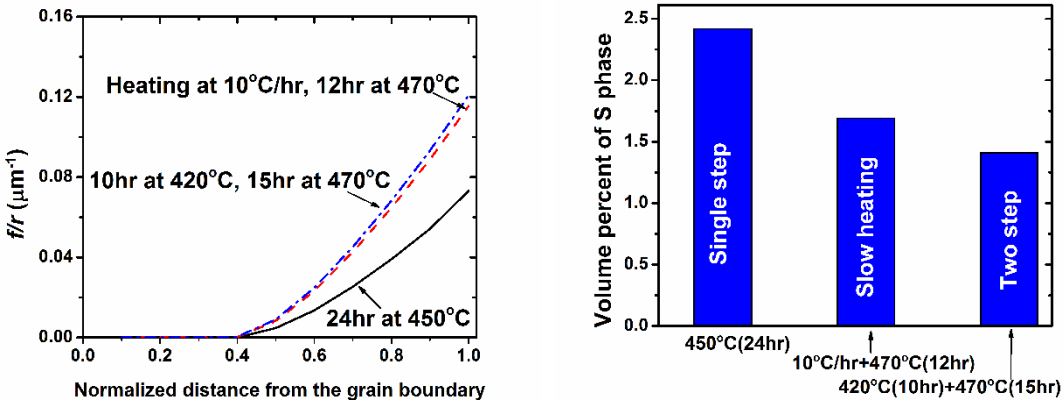

(a) (b)

Figure 4.8: Comparison of (a) f/r ratios from the center to the edge of the grain and (b) volume fraction of S phase remaining for different homogenization schedules.

(Cu, Mg, Zn, Zr), zirconium has the smallest diffusion coefficient and shows no significant change across the grain through all the homogenization processes simulated. Because copper is the slowest diffusing element that exhibits changes during these processes, its behavior has the most influence on the rate of phase change at the grain boundary and the nucleation and growth of Al_3Zr.

It can be seen in Figure 4.9 that the total amount of Cu in the grain is predicted and observed increasing with time. This increase in Cu is due to the dissolution of η (32.4wt% Cu), which releases copper to the α matrix. Before t = 2 hours, however, the S phase (44.1wt% Cu) nucleates and grows at the grain boundary and consumes enough copper to decrease the amount rejected to the grain. This delayed appearance of S is the reason for the dip in the Cu composition in α near the grain boundary in Fig. 5 at t = 2 hours; it is smoothed out later as the η and S phase fractions stabilize and copper diffuses in the α towards the grain center.

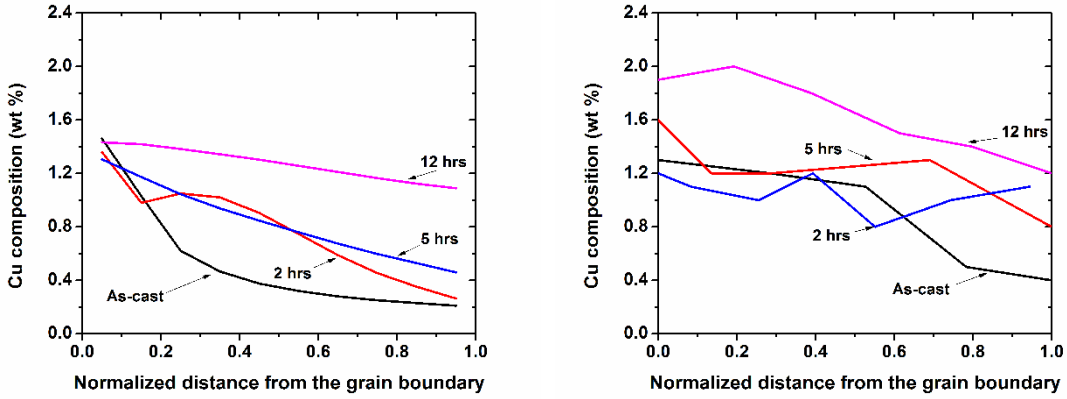

Figure 4.9: Composition of Cu along the half SDAS at different times of homogenization at 450°C (a) predicted by the numerical model (b) measured by EDS.

4.4.4 Microstructural Evolution of Interdendritic Phases during Homogenization

The as-cast Al-6.2Zn-2.3Cu-2.35Mg-0.13Zr (wt%) alloy has a dendritic microstructure with the interdendritic particles mainly consisting of aluminides with an EDS-measured average composition Al-16Cu-14.5Zn-15.5Mg (wt%). These aluminides and their transformation to the S-phase have also been observed by Deng et al[2]. and are represented here by the η phase.

Figure 4.10 shows the evolution at 450°C of volume fractions of different phases with time from the as-cast microstructure predicted by the homogenization model. The equilibrium microstructure at 450°C includes the α and S phases, but not η (as well as nanosized Al_3Zr discussed in section 4.4.5). The transformation of η to S phase and the gradual dissolution of both secondary phases to their equilibrium values are observed. The curves clearly show three distinct stages of phase evolution behavior. The dominating

mechanism and kinetics in each stage are different and are discussed in the following sections.

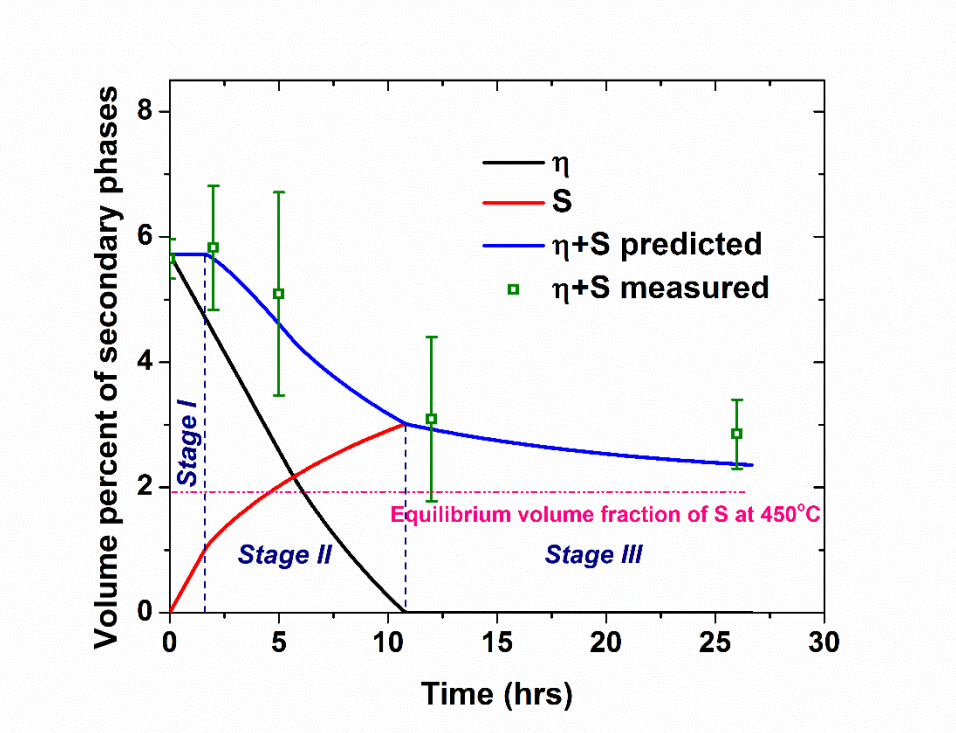

Figure 4.10: Evolution of predicted and measured volume fraction of secondary phases during homogenization at 450°C. The equilibrium microstructure contains no η phase.

4.4.4.1 *Stage I*

During this first stage, there is no change in total volume fraction of the two secondary phases in the interdendritic region as η transforms to S. Nucleation and growth of S phase occurs at a high and steady rate until 1.6 hours (Figure 4.10), as it takes Cu from the α phase and the consumed η. This transformation is modeled as controlled by the

interface reaction rate, leading to a linear decay of volume fraction with time. The interfacial transfer of Cu atoms from η to S is sluggish and is the rate-determining step.

4.4.4.2 *Stage II*

Stage II commences when the net S growth rate slows. The growth of S comes at the expense of η (as described above), but, as its volume fraction exceeds the equilibrium value (seen in Figure 4.10), a diffusion-controlled S ⇒ α reaction begins. This transformation rate increases as the S fraction increases further from equilibrium, continually decreasing the net rate of S production. This stage hence has a mixed influence of both the interface reaction rate and diffusion controlled kinetics. This process continues until all the η phase disappears at about 11 hours of homogenization at 450°C.

4.4.4.3 *Stage III*

With the η gone, the third stage consists of diffusion-controlled dissolution of S into the α-Al matrix, as the S has reached volume fractions above the equilibrium level. This process continues at ever slower rates. After 26 hours at 450°C, the process is terminated, as it may take another day of simulation time to approximate equilibrium.

This predicted behavior of the phase volume fractions has also been verified through XRD and DSC measurements as seen in Figure 4.11. The strongest intensity peaks for η and S phase lie within $30° < 2\theta < 50°$. Fig. 5(a) shows η peaks (~35° and 40°-45°) in the initial as-cast microstructure, but they fade over the first few hours, while the S peaks begin to appear at 2 hours as stage II commences. A very small quantity of η is detected at 5 hours and none at 12 hours, which either represents a very sluggish dissolution rate at the end or a reappearance during quenching. The amount of S peaks in the measurement at 12

hours (beginning of Stage III), after which it decreases. The strongest peaks in the plot at $2\theta = 38.4^{o}$ and 44.7^{o} are the α phase.

Similar observations are also made using the DSC measurements seen in Figure 4.11(b). The start temperature of the peaks is calculated by drawing tangents where the peak begins and when the peak is fully developed which intersect at the start temperature. The exothermic peak starting at 478°C in the DSC plot for the as-cast alloy is likely associated with the melting of the η phase. A bigger endothermic peak at 487°Cnext to it is identified to be aluminides with composition of Al-54.4%, Cu-16%, Zn-14.5%, Mg-15.5% measured by EDS. These aluminides are solid solutions of the η phase. As the alloy is homogenized, the exothermic peak pertaining to melting of S phase at 489°C can be identified along with the earlier peak of 478°C at 2 hrs which remains at 5 hours as the amount of S grows during stages I and II. However, the endothermic peak at 478°C is no longer seen at 5 hours as all the η dissolves after Stage II. At the same time the exothermic peak pertaining to the aluminide is replaced by the endothermic peaks by S phase with composition of Al-56.9%, Mg-23.8% and Cu-19.4% measured by EDS. Because the S phase dissolves during Stage III, the endothermic peak intensity is low at 26 hours. The percent η+S volumes from these XRD and DSC measurements are compared to predictions in Figure 4.10 and show a very good agreement

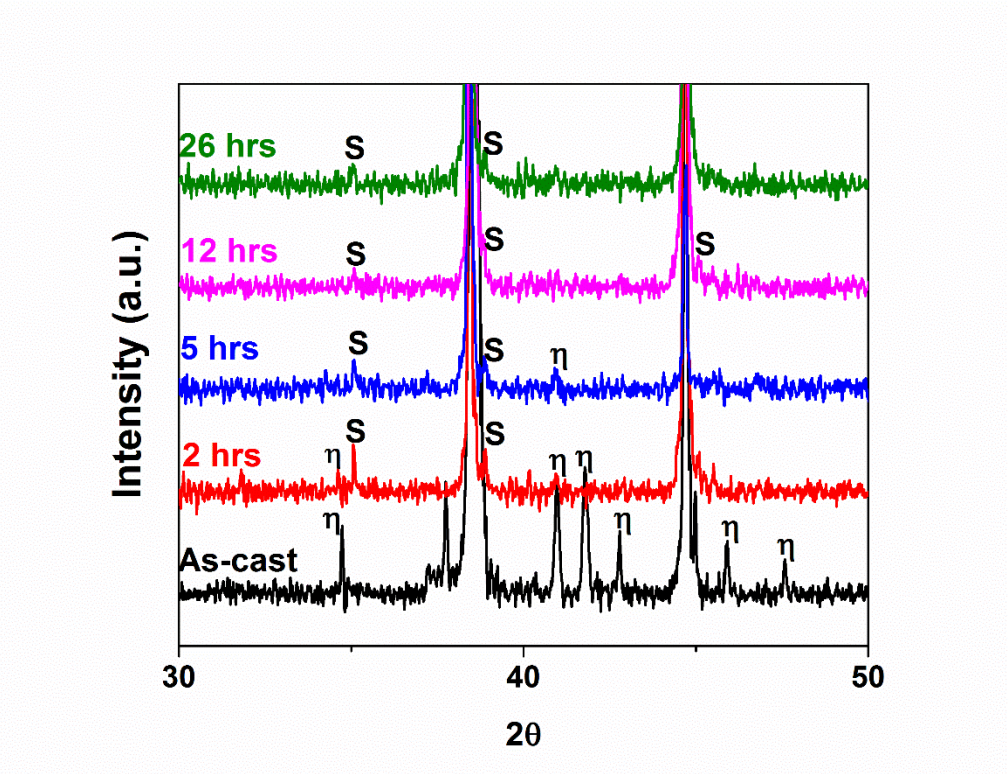

(a)

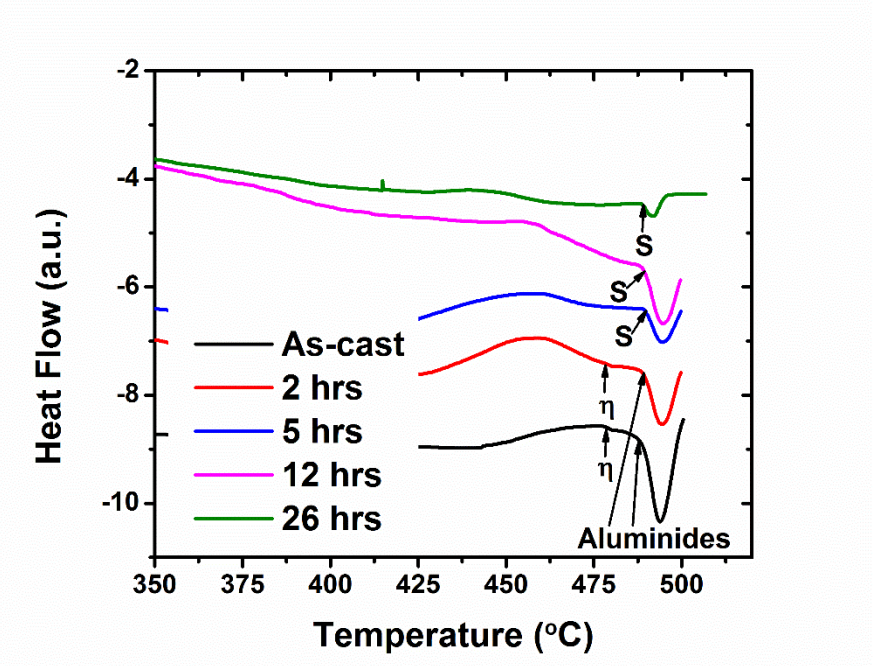

(b)

Figure 4.11: (a) XRD plots (b) DSC curves of samples as-cast and homogenized at 450°C. The arrows on the DSC plots indicate start of the endothermic peaks for the corresponding phases.

4.4.5 Microstructural Evolution of Al_3Zr Dispersoids during Homogenization

During homogenization of Al-Zn-Cu-Mg-Zr alloys, along with the interdendritic phase transformations and composition diffusion at the grain size length scale, microstructural changes occur on a smaller length scale. Nanosized Al_3Zr dispersoids can precipitate throughout the matrix, a process in which diffusion is the rate-limiting step and which has been numerically modeled by Robson[89]. Their work assumed homogeneous nucleation (not the more likely heterogeneous), resulting in fewer active nucleation sites and so lower final number densities and dispersoid radii that have been experimentally observed. The present model for Al_3Zr behavior is based on Robson's[89], except with the assumption of heterogeneous nucleation and the linkage to the grain scale microstructure evolution model. The numerical predictions are compared to experimental observations in Figure 4.12, and the simulation results fall within the experimentally observed ranges. The initial number of heterogeneous nucleation sites considered in the model has a profound effect on the predicted number densities and size distributions which causes the deviations seen in the predicted values from experimental measurements.

The time evolution of number density and mean radius of the dispersoids on homogenization at 450°C can be seen in Fig. 4.13(a). No direct correlation of the time evolution with the different stages observed in the evolution of the interdendritic particles is seen. The number density increases sharply initially and then levels off as the nucleation sites saturate. The mean radius also increases very quickly at first, but then growth slows due to decreasing compositional supersaturation.

There is a compositional gradient of Zr in the as-cast alloy due to microsegregation as seen in Figure 4.4. The composition is highest at the center (0.162%) and it decreases

towards the grain boundary (0.004%). The diffusion of Zr in Al is very slow compared to the other elements and so there is no noticeable change in the Zr distribution across the grain, even after prolonged homogenization. This Zr variation causes a variation of microstructure across the grain and so the precipitation kinetics also vary. Fig. 4.13(b) and (c) show the time evolution of number density and volume fraction at various normalized positions on the half grain (0 being the edge of the grain and 1 the center). There is a dispersoid free zone close to the grain boundary, which is detrimental to the alloy's mechanical properties, as the Al_3Zr inhibits recrystallization during downstream solution heat treating prior to aging. As the rate of increase of volume fraction and number density is highest at the grain center, it attains the critical volume fraction to mean radius ratio required to pin grain boundaries before other positions. This ratio is a measure of the pinning pressure applied by these dispersoids to inhibit grain boundary motion during recrystallization. Homogenization for longer durations would be required to precipitate dispersoids at closer to the grain boundary, but in that time mean values of the older dispersoids would be much larger.

The number density increases from the grain boundary to the center and a saturation of all the heterogeneous nucleation sites in the center is observed. As the driving force for nucleation of Al_3Zr is highest at the center of the grain (where the Zr concentration is highest), the number density there shows the fastest increase. Because of this abundance of Zr, growth is also faster at the center, giving the highest volume fraction, as seen in Figure 4.13(c). Figure 4.13(d) shows the dispersoid size distribution at different positions across the half grain. Again, the higher availability of Zr allows faster nucleation and growth, and so the distribution of Al_3Zr radii is shifted to higher values there.

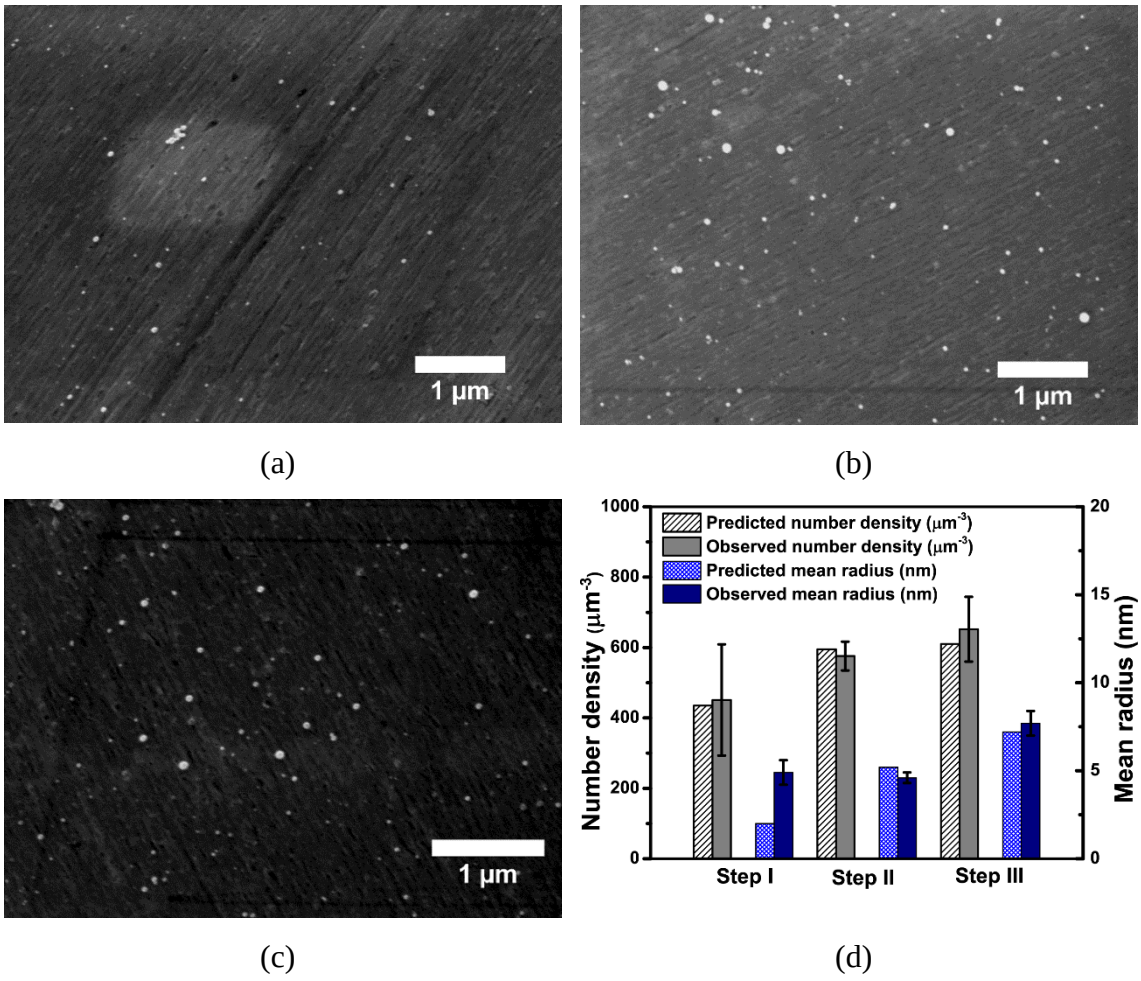

(a) (b)

(c) (d)

Figure 4.12: Secondary Electron images of Al-6.2Zn-2.3Cu-2.35Mg-0.13Zr alloy after (a) Step I; (b) Step II; (c) Step III; (d) Comparison of numerically predicted and experimentally observed size distribution of dispersoids after 3 steps of homogenization. (Step I: 10 hrs at 420 ^{o}C; Step II: 4 hrs at 470 ^{o}C; Step III: 15 hrs at 480 ^{o}C)

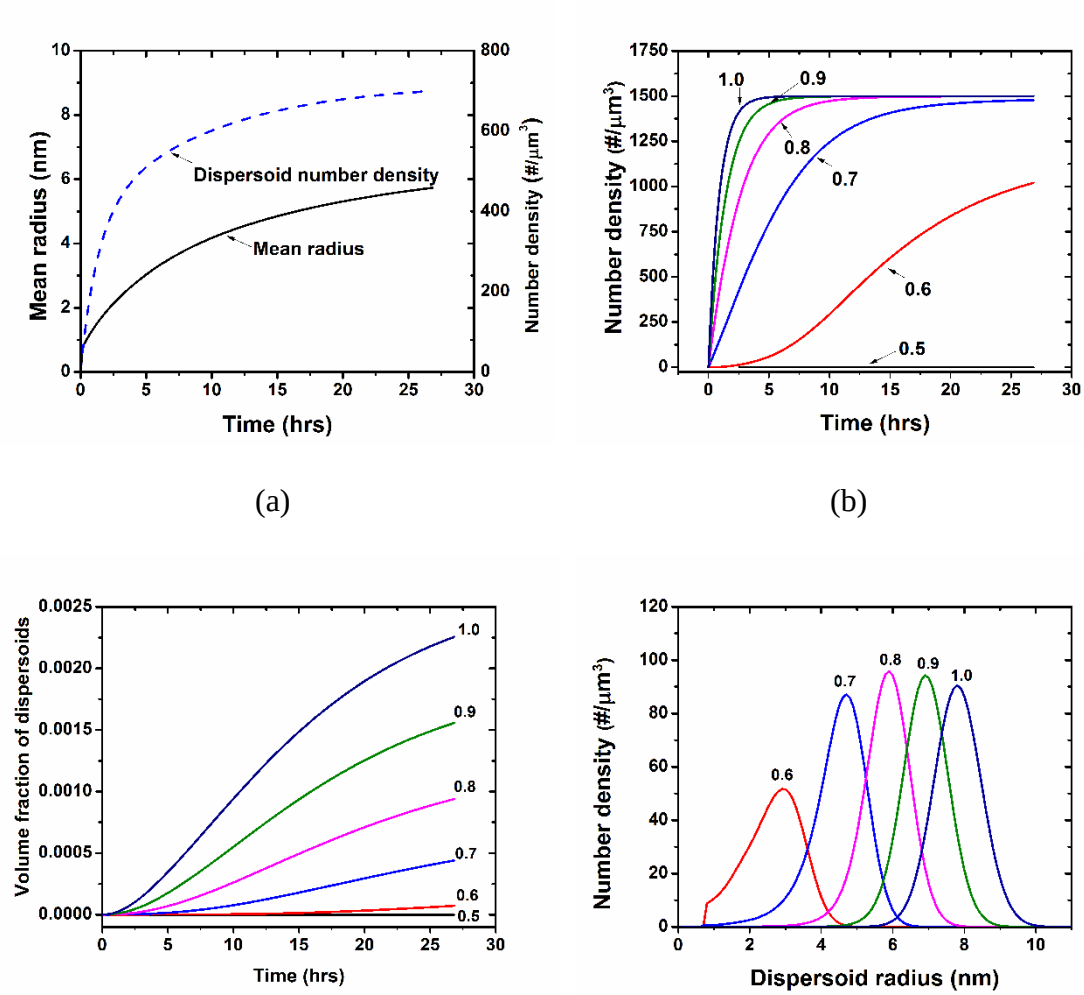

Figure 4.13: (a) Time evolution of mean dispersoid radius and number density during homogenization at 450°C; Time evolution of (b) number density (c) volume fraction of the dispersoids at different positions across the grain; (d) Size distribution of the dispersoids at the different normalized positions across the half grain (1 refers to the grain center).

4.4.6 Effect of Heating Rate on Dispersoids

During the course of the experiments conducted, we found that the heating rate at the beginning and in between the homogenization stages had a profound effect on the dispersoid number density and mean radius. Fast heating rates led to dissolution of the previously formed dispersoids leading to a reduction in number density and coarsening of the dispersoids. 'Reversion' which refers to the dissolution of the precipitated dispersoids on sudden increase of temperature was responsible for such a phenomenon. Figure 4.14 shows the microstructure of the dispersoids precipitated at heating of the sample at 10°C/min and holding at 420°C for 10 hours. The number density of the sample is 330μm^{-3} which is less than the number density when the sample was heated at a much slower heating rate of 20°C/hr as seen in Figure 4.12 (a). Figure 4.14(b) shows the microstructure after the next homogenization step at 470°C for 5 hours which was reached at a very fast heating rate of 1°C/min. The number density of this microstructure was found to be 25.5μm^{-3} which shows that most of the dispersoids formed in the previous step were dissolved during faster heating. Coarsening of the dispersoids was also observed as the mean radius of the dispersoids was calculated to be 25.2 nm as compared to 13.9 nm in the previous step.

The reversion and coarsening of the dispersoids can be explained on the bases of the phase diagram. Figure 4.15 shows the schematic of the Al-Al_3Zr phase diagram. At a temperature T_0, the concentration of the matrix at the Al-Al_3Zr interface is C_{p0} for the matrix composition of $C_{m0} > C_{p0}$ leading to growth of the dispersoid. On suddenly increasing the temperature to T_1 the matrix composition remains C_{m0} while the composition at the interface becomes $C_{p1} > C_{m0}$ leading to dissolution of the dispersoids as shown in the

schematic in Figure 4.15(b). Due to dissolution, the composition of the matrix increases to $C_{m1} > C_{m0}$ leading to rapid growth of the dispersoids. Thus fast heating due to this sequence of procedures leads to dissolution and coarsening of the diapersoids, which was also reported by Morere et al.[85].

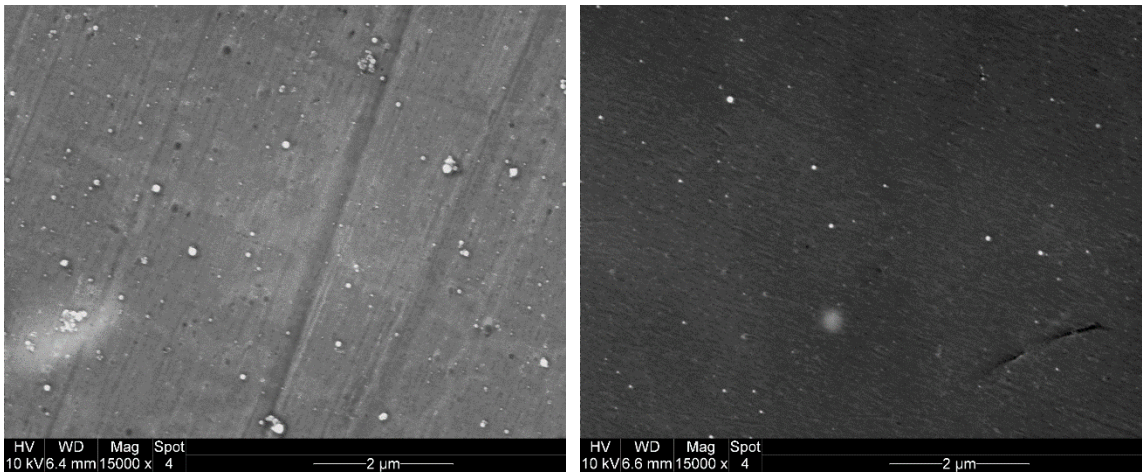

(a) (b)

Figure 4.14: Microstructure after (a) heating at 10°C/min to 420°C and holding for 10 hours (b) followed by heating at 1°C/min to 470°C and holding for 5 hours.

4.4.7 Process Recommendations

The findings in this study about the microstructural evolution occurring at the grain size and dispersoid scales can be used to suggest homogenization schedules which can minimize time and energy consumption. The end microstructure after homogenization of Al-Zn-Cu-Mg-Zr alloys ideally is devoid of all secondary phases and should have a uniform distribution of nanosized coherent Al_3Zr dispersoids. The η and S phases are undesirable because they degrade the mechanical properties and act as nucleation sites for

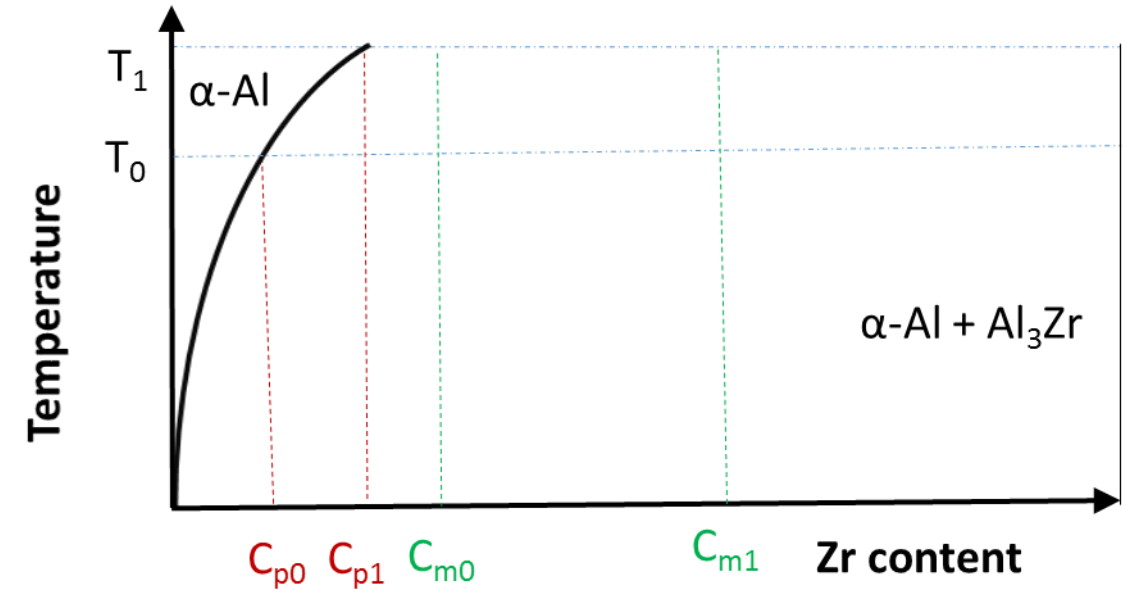

(a)

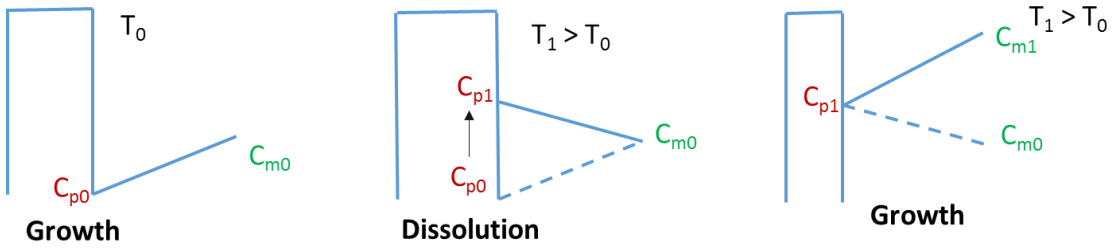

(b)

Figure 4.15: (a) Schematic of the Al-Al_3Zr phase diagram (b) the reversion and coarsening of the dispersoids on fast heating.

recrystallization, while the dispersoids are desired to pin the grain boundaries, inhibiting recrystallization.

The interdendritic secondary phase η present in the as-cast alloy transforms to the S phase during homogenization. From DSC measurements, the incipient melting point of the η phase is 478°C and that of the S phase is 489°C, which agree with literature values[2]. To minimize homogenization time without melting the initially present η phase, we need to homogenize at a temperature close enough to the melting point of η for fast diffusion but not enough to cause melting. During homogenization, the η dissolves completely in Step II and the dissolution of S phase continues during Step III, the latter of which can be sped up by increasing the temperature by 10°C. This increase can be done because melting point of S phase is 10°C higher than that of dissolved η.

Section 4.4.2 has a detailed study on the precipitation of Al_3Zr dispersoids in these alloys to find a schedule that produces a microstructure with a distribution of Al_3Zr dispersoids across the entire grain with a high volume fraction/mean radius ratio. It was found that homogenizing these alloys first at a lower temperature (420°C) for 10 hours leads to precipitation of a nanosized, coherent dispersoids which apply a higher pinning pressure. This temperature has low enough diffusion and supersaturation needed for nucleation but not high enough to cause rapid coarsening of the dispersoids. This step can be followed by homogenization at a higher temperature necessary to dissolve the secondary phases.

We recommend a three step homogenization for the Al-6.2Zn-2.3Cu-2.35Mg-0.13Zr alloy (AA7050):

(i) Step I: Homogenize at 420°C for 10 hours to precipitate many small Al_3Zr dispersoids, increasing pinning pressure to minimize recrystallization during later processing;

(ii) Step II: Homogenize at 470°C below the melting point of η, for 4 hours to transform it to S phase completely; and

(iii) Step III: Homogenize at 480°C below the melting point of S phase for 15 hours to minimize it.

A slow heating rate of 20°C./hr was chosen to transition between the steps.

Typical experimental microstructures observed after each step can be seen in Figure 4.16(a)-(c). Figure 4.16(d) shows the predicted and observed time evolution of various phases during the three step homogenization schedule. The observed volume fractions match the predicted values within the range of experimental uncertainty. Figure 4.17 shows the DSC curves and XRD spectra for the alloy in the as-cast condition and after each homogenization step. It can be seen that after Step I the endothermic peak for the S phase appears and that pertaining to η disappears. The peak corresponding to the aluminides overlap with the S phase melting after Step I. After Step II, we observe a shift in the endothermic peak pertaining to S phase melting to higher temperatures, indicating absence of the aluminides. None of the endothermic peaks are visible after Step III, indicating complete dissolution of the secondary phases. However, some small amount of S is left after Step III, which goes undetected in DSC but is visible in the micrographs in Figure 4.16(c). The XRD plots in Fig. 4.17(b) indicate similar trends. While the peaks corresponding to the S phase (~35°) appear along with those of η after Step I, those

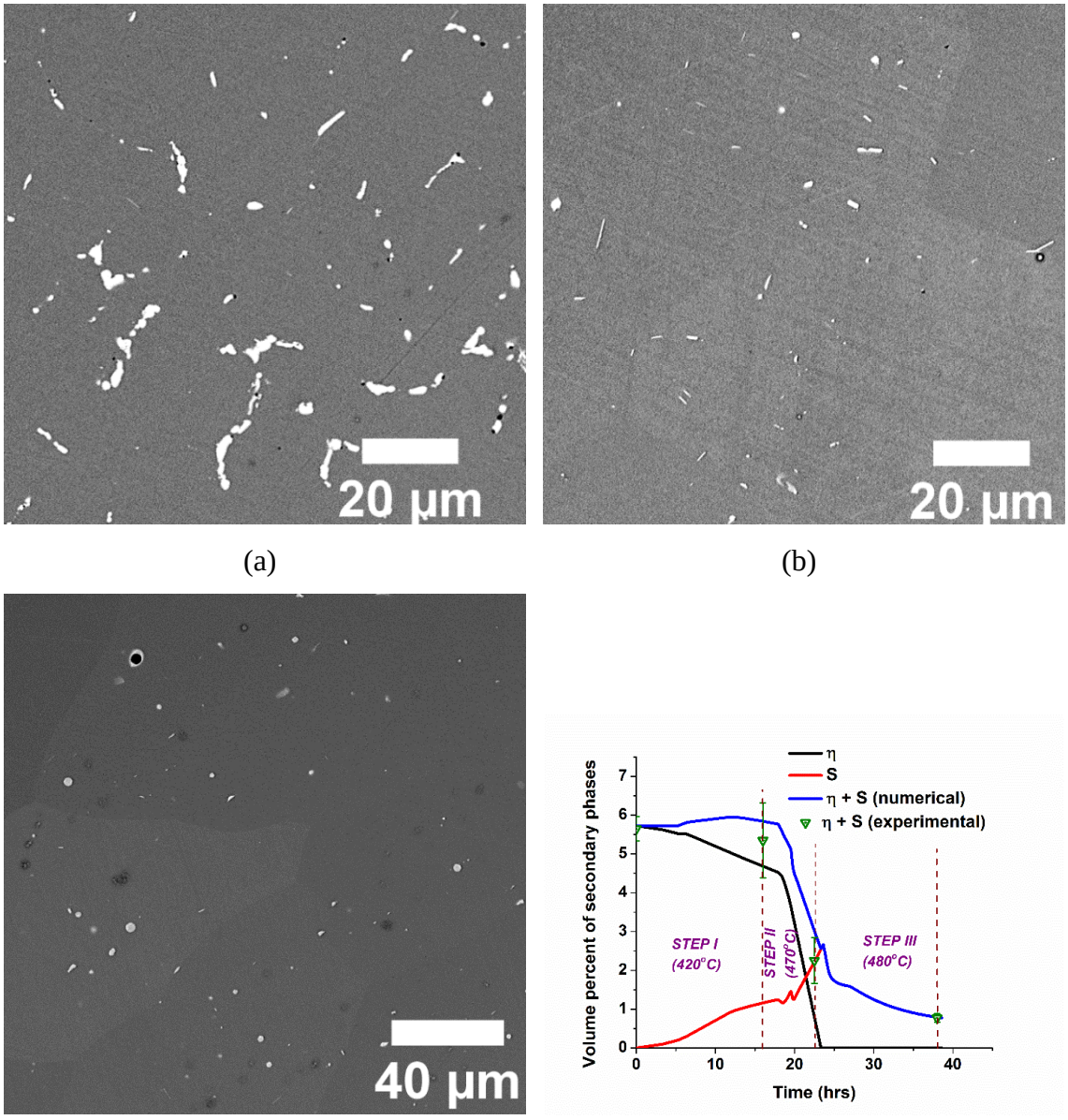

(a) (b)

(c) (d)

Figure 4.16: Backscattered Electron micrographs of the Al-6.2Zn-2.3Cu-2.35Mg-0.13Zr after (a) Step I (white phase is η+S); (b) Step II (white phase is S); (c) Step III(white phase is S); The grey phase is α-Al.(d) Numerically predicted volume fraction of secondary phases compared to experiments.

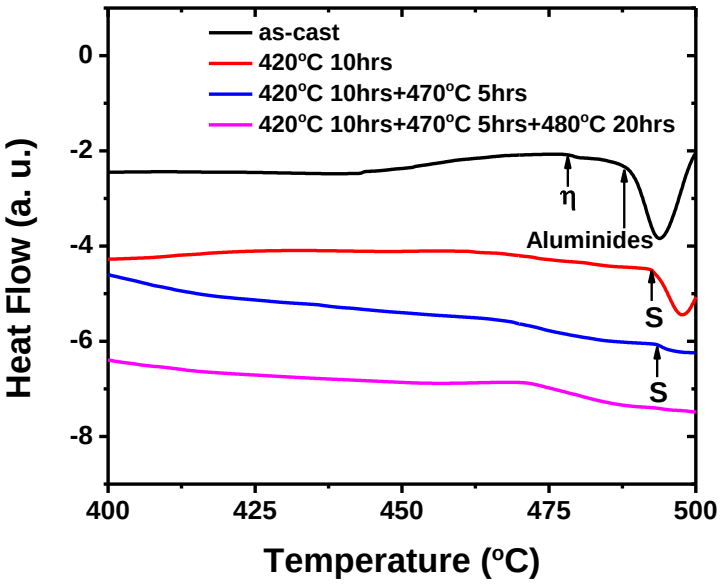

(a)

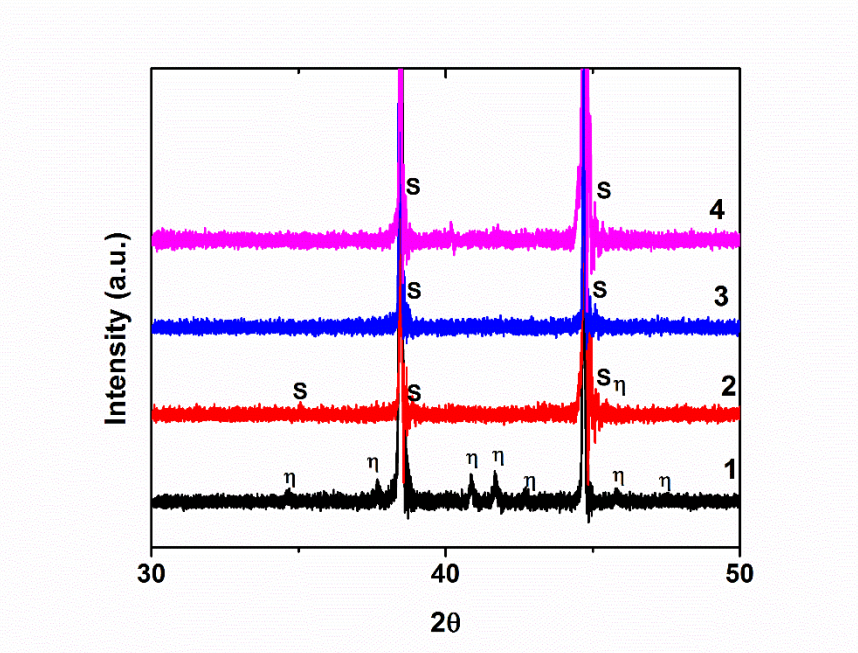

(b)

Figure 4.17: (a) DSC plots and (b) XRD spectra from samples after every step of homogenization. Curves: (1) as-cast; (2) after 420°C for 10 hours; (3) after (2) + 470°C for 4 hours; (4) after (3) + 480°C for 15 hours.

corresponding to η (close to 38°) disappear after Step II. Only the peaks corresponding to α-Al can be seen after Step III.

Figure 4.12(d) shows a comparison of experimental and numerical number density and mean dispersoids sizes after the 3 step homogenization and a reasonable match is seen. The observed mean radius after Step I is more than the predicted value because the number density was calculated from image analysis of SEM micrographs with poor contrast at very small sizes, thereby discounting the smaller structures. Both the number density and mean radius generally increase after every step.

4.5 Conclusion

A model of coupled phase transformations at two different length scales during homogenization of Al-Zn-Cu-Mg-Zr alloys has been developed. A CA-FV based model which simulates elemental diffusion in the grain and microstructural evolution of the interdendritic η and S phases has been linked to a PSD-based model which simulates precipitation of Al_3Zr dispersoids across the grain, providing a comprehensive picture of time evolution of microstructure. The sluggish nature of the η to S phase transformation is attributed to interface-controlled kinetics, which is included in the numerical model using a novel approach. During homogenization, η transforms to S phase and the remaining S phase then dissolves to reach the equilibrium volume fraction. While this occurs, the Al_3Zr precipitates and grows, but are mostly found near the grain center which has the highest Zr concentration in the as-cast microstructure.

Based on the sequence and rates of transformations, a three stage homogenization schedule is suggested for this alloy. Homogenization at 420°C for 10 hours, followed by 470°C for 4 hrs and 480°C for 15 hours, is seen to produce a microstructure consisting of

uniform nanosized dispersoids with maximum pinning pressure and minimum secondary phases. The suggested homogenization temperatures are 8-9°C below the incipient melting temperatures of the alloy also indicated by the DSC results. This model can easily be used for optimizing the homogenization schedules for other 7XXX alloys which will be discussed in the next chapter. An accurate prediction for the duration of Step II needed to dissolve the η, helps in making the process time efficient by taking advantage of the faster diffusion at higher temperatures in Step III.

CHAPTER 5. IMPROVED 7XXX COMPOSITIONS FOR EASE OF HOMOGENIZATION AND EXTRUSION

5.1 Introduction

Compositional variations in Al-Zn-Cu-Mg-Zr alloys have significant effects on the microstructure after casting and homogenization, which influences the workability and mechanical properties of these alloys[90–94] during extrusion. The varying amounts of alloying elements lead to stabilization of coarse interdendritic particles[13], as well as affect the distribution of fine dispersoids[95] across the secondary dendrite arm spacing (SDAS) or the grain during homogenization of the as-cast alloys. Thus the alloying elements affect the microstructure both at the SDAS and the dispersoid length scale.

The composition determines the stable or metastable phases which remain after processing. The η, T or S phases that remain affects the mechanical properties: strength, ductility and fracture toughness of the component[92,94]. While the η and η' phases are desirable, T and S are not. The η and η' precipitates formed during age-hardening of these alloys, increase the strength and fracture toughness of the alloy[92,94]. The T and S phases have low melting temperatures[96] which might melt during thermo-mechanical processing. The S phase is brittle and also affects the fracture toughness of the material[97,98].

Increase in the Zn:Mg ratio decreases the amount of T and S phases in the alloy[13]. Increasing the Zn also improves the strength of the component[94]. However, very high amounts of (Zn+Cu+Mg) make the component quench sensitive[13], requiring very high

cooling rates to subdue precipitation which may lead to residual stresses[99,100] and deformation which is not uniform. Decreasing the Mg and Cu content decreases the amount of T phase and S phase both of which are desirable. However, they are needed for age-hardening precipitation reactions of these alloys[101].

Alloying elements in these multi-component alloys also affect the solubility of Zr in Al, affecting their microsegregation during casting, and nucleation and growth during homogenization. Because there is a variation of Zr composition across the SDAS which is not eliminated after homogenization due to its low diffusivity, there is a difference in microstructure along the SDAS which also depends on the composition of the alloy. Robson and Prangnell[95] have looked at the effect of Zn, Cu and Mg on precipitation of Al_3Zr dispersoids. However, the effect on the initial microsegregation of Zr which in turn affects the precipitation behavior has not been considered. In this study, we try to evaluate the microstructure both in the interdendritic regions and across the grains in the as-cast and homogenized parts, which is affected by variations in compositions.

For ease of homogenization, (i) the initial volume fractions of the interdendritic fraction should be minimum and (ii) the transformed S phase volume fractions should be low so that a homogenized structure with a uniform distribution of Al_3Zr dispersoids and minimum S phase in α-Al is achieved in minimum time. For ease of extrusion, (i) S phase in the homogenized alloy should be minimum (affects hot ductility) and (ii) there should be a high number density of fine nano-sized Al_3Zr dispersoids across the grain (to inhibit recrystallization). Compositions which lead to these microstructural goals are investigated.

The current study is a comprehensive study of the effect of composition on microstructure after homogenization at two different length scales. The aim is to achieve a

microstructure which is easy to homogenize and extrude. A numerical model which couples microstructure development in the interdendritic regions involving transformation of η to S phase, and their subsequent dissolution, with the precipitation of Al_3Zr dispersoids across the SDAS, discussed in CHAPTER 4, has been used here. The initial as-cast microstructure (interdendritic volume fractions and microsegregation) predicted by Thermo-Calc™ is used. Microstructural evolution for compositions in the range of the specification for 7XXX is studied to reach improved composition ranges for better extrudability, minimum recrystallization and better age-hardenability. Experiments performed by Sun et al.[102] verify the microstructural evolution during homogenization for a solute rich and solute lean specimen.

Effect of alloying elements Zn, Cu, Mg and Zr on the microstructure after homogenization at 450°C has been numerically studied. The baseline case was that of Al-6Zn-2Cu-2Mg-0.13Zr pertaining to AA7050 alloy. The ratios of Zn/Mg in the range of 1.5 to 6 and Zn+Cu+Mg in the range of 8 to 14 wt% have been investigated. The various compositions that have been investigated numerically into are provided in Table 5.1.

5.2 Effect of Composition on Evolution of Interdendritic Phases

Composition of the alloy affects the phases formed during solidification as well as the phase transformations during homogenization. It also affects the phases present after post-homogenization processing: extrusion and age-hardening which will not be discussed in the current work.

Table 5.1: The different test cases run for different compositions.

Test case	Zn	Cu	Mg	Zr	Zn/Mg	Zn+Cu+Mg
Zn1	4	2	2	0.13	2	8
Zn2/Cu2/Mg2	6	2	2	0.13	3	10
Zn3	8	2	2	0.13	4	12
Zn4	10	2	2	0.13	5	14
Cu1	6	1	2	0.13	3	9
Cu3	6	3	2	0.13	3	11
Cu4	6	4	2	0.13	3	12
Mg1	6	2	1	0.13	6	9
Mg3	6	2	3	0.13	2	11
Mg4	6	2	4	0.13	1.5	12
Zr1	6	2	2	0.05	3	10
Zr2	6	2	2	0.10	3	10
Zr3	6	2	2	0.15	3	10
Zr4	6	2	2	0.20	3	10

5.2.1 Effect on As-cast and Homogenized Microstructure

The microstructural evolution during homogenization for different compositions can be compared only when the initial as-cast microstructure has the right volume fractions of the interdendritic phases which in turn depend on the compositions. Scheil type solidification calculations were performed using Thermo-Calc^{TM} to predict the as-cast microstructures for the different test cases. The compositions not only affect the as-cast phases but also the microsegregation of various alloying elements which has a considerable effect on the segregation of Zr and Al_3Zr precipitation which will be discussed in the later section.

Varying amounts of Zn, Cu and Mg in the alloy leads to varying amounts of T phase, V phase and the S phase in the as-cast microstructure. While T phase is a solution of the $MgZn_2$ or the η phase, also represented as $(Al,Cu,Zn)_{49}Mg_{32}$, the V phase also known as the Z phase, is a solution of Mg_2Zn_{11} and $Al_5Cu_6Mg_2$ with varying Cu and Al solubility. The S phase is mostly stoichiometric represented as Al_2CuMg. For the sake of numerical calculations, the T and V phases are taken as a single solid solution which will transform to the S phase which has been experimentally observed[2,12].

The effect of Zn, Cu and Mg on the as-cast interdendritic phases is shown in Figure 5.1. Increase in Zn leads to increase in the Zn-rich T and V phases which transform to S phase for upto 8% Zn levels during homogenization, as seen in Figure 5.2(b). Increase in Zn levels lead to longer Stage II transformations which was discussed in CHAPTER 4. Zinc levels more than 8% leads larger volume fractions of T+V in the as-cast material which are difficult to dissolve as seen in Figure 5.2(a). It is interesting to note no linearity in volume fraction change indicating the transformations may be diffusion controlled. Decreasing the Zn levels on the other hand, does not help either, as the fraction of the S phase increases due to increased Cu and Mg contents. This S phase takes more time to dissolve leading to longer Stage III transformations. Also, Zn is needed for precipitating Zn-rich η' phase during age-hardening which leads to strengthening.

Increase in Cu leads to decrease in the Zn-rich T phase, and an increase in the Cu-rich S phase and V phase, which has increased Cu solubility, in the as-cast microstructure, as seen in Figure 5.1(b). The increased T+V volumes lead to longer Stage II

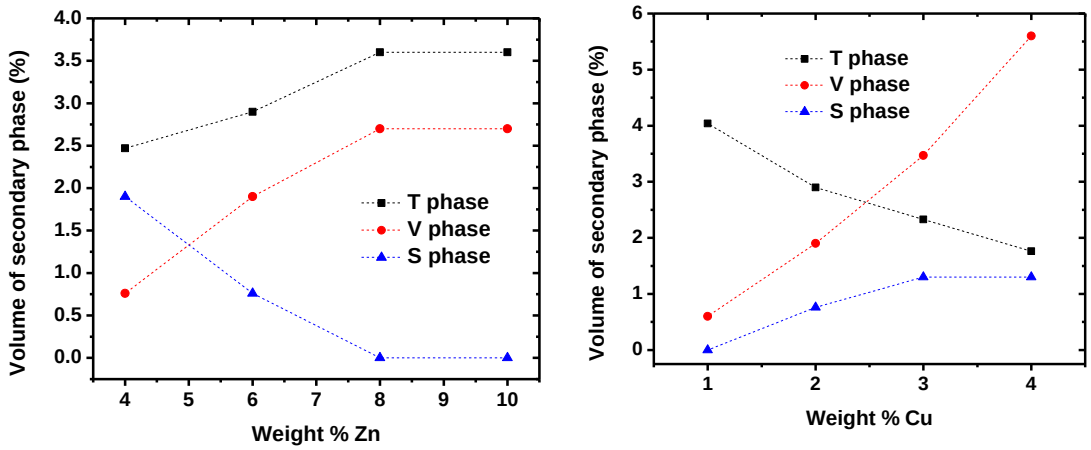

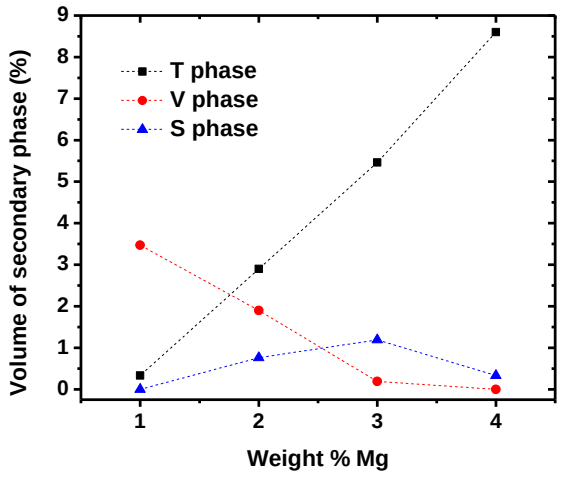

(c)

Figure 5.1: Effect of varying amounts of (a) Zn, (b) Cu and (c) Mg on the initial volume fraction of interdendritic particles in the as-cast state for the base composition of Al-6Zn-2Cu-2Mg-0.13Zr predicted by Thermo-Calc™.

transformations to S phase during homogenization, resulting in larger volume fractions of S phase as seen in Figure 5.2(d). This S phase needs to be minimized leading to longer Stage III transformations. Low Cu compositions of ~1% leads to a short Stage II and even shorter Stage III as the volume fraction of S phase formed is low and easy dissolves to give a S phase free microstructure which is desirable. However, Cu is needed in the alloy for strength and ductility[103].

Increase in Mg content leads to an increase in the Mg-rich T and S phases and a decrease in the Zn-rich V phase in the as-cast microstructure as seen in Figure 5.1(c). The S phase is seen to decrease after 3% Mg as it is replaced by T phase which is even richer in Mg. A peculiar thing to note during homogenization is higher Mg leads to an initial increase in T phase and decrease in S phase owing to microsegregation of Mg which leads to a very high concentration of Mg near grain boundaries which favors a reversion of S phase to T phase (Figure 5.2(e) and (f)). Increasing the Mg content leads to an increase in the Stage I and Stage II transformations when the T phase transforms to S phase. Mg of 4% leads to an extended Stage II without a Stage I, which extends to more than 50 hours as seen in Figure 5.2(e). There is no linearity in the volume fraction change indicating diffusion controlled transformations for high Mg content of 4%. The amount of transformed S is minimum for 1% Mg which has a short Stage II and Stage III leading to complete dissolution of S phase during homogenization as seen in Figure 5.2(f). Magnesium is however, a much needed alloying element needed for the strengthening η' precipitates.

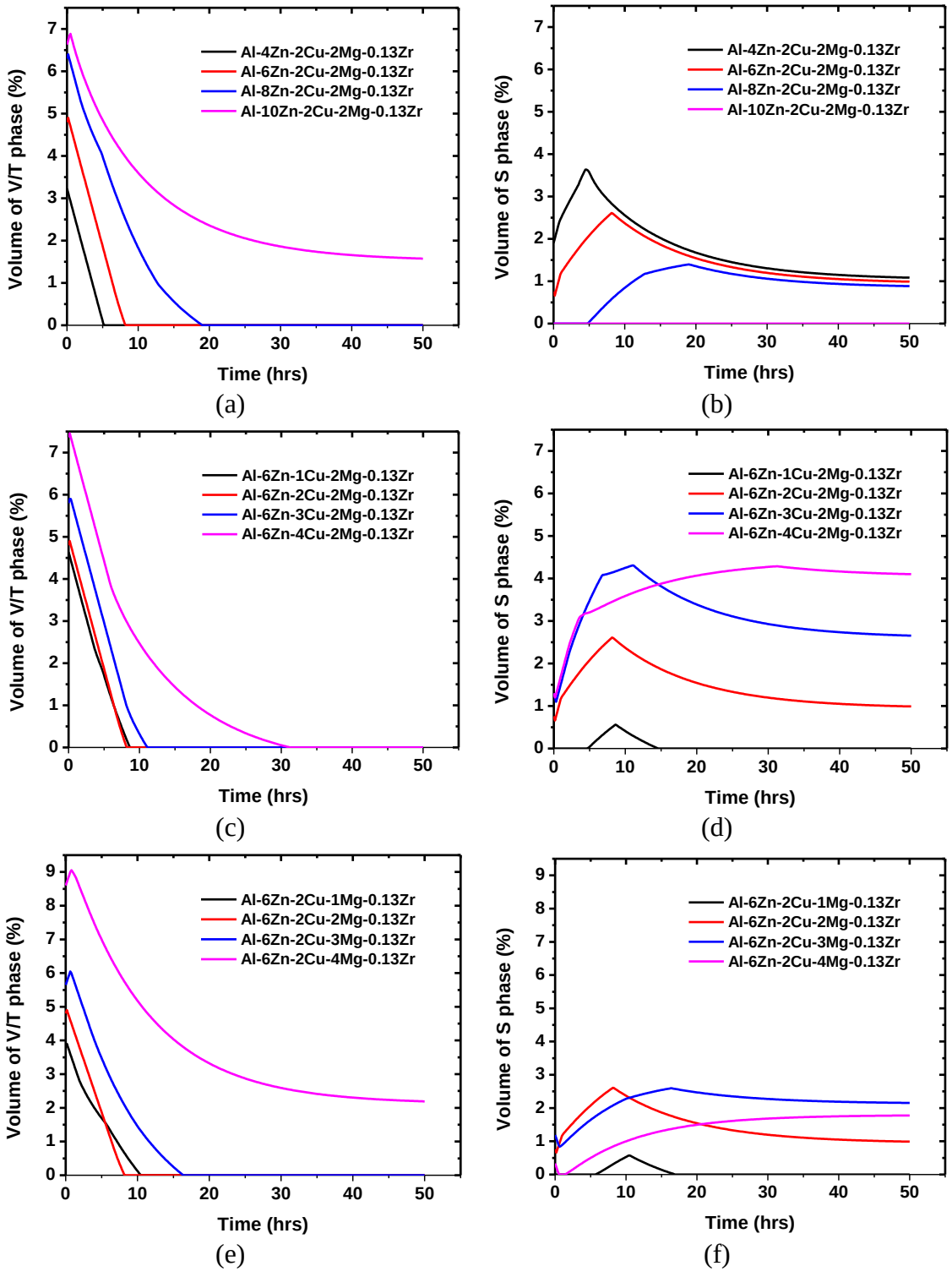

Figure 5.2: Effect of alloying elements (a),(b) Zn; (c),(d) Cu and (e),(f) Mg on evolution of T/V and S phases respectively during homogenization at 450°C.

5.2.2 Comparison with Phase Diagrams

Table 5.2 summarizes the effect of composition on as-cast microstructure and time taken for homogenization. The effect of composition on microstructural evolution witnessed in this study is because these alloying elements affect the phase diagrams for quaternary Al-Zn-Cu-Mg system. The phase diagram information is incorporated in the numerical model from Thermo-Calc^{TM} using the TCAL1 database. An older version for these phase diagrams is available from Stawbridge et al[104]. An updated version from Thermo-Calc^{TM} using TCAL1 database is presented in Figure 5.3 for compositions of 4%, 6%, 8% and 10% Zn.

Table 5.2: Summary of effect of composition on as-cast microstructure and homogenization time

	As-cast	**Homogenized**
Higher Zn	More T, More V	More time for stage II and stage III
Higher Cu	More S and V, Less T	Way more time for stage III
Higher Mg	More T and S, Less V	More time for stage I and lesser time for stage III

With increase in Zn content the number of stable phases in the composition range investigated increases. At low Zn content, Mg-rich T is stable at low Cu contents and Cu-rich Θ is stable at low Mg contents as seen in Figure 5.3(a). At intermediate compositions of Cu and Mg the S phase stabilizes. With increase in Zn, V phase with high Cu solubility stabilizes for higher Cu contents as seen in Figure 5.3(b). For still higher Zn of 6% the η phase appears as seen in Figure 5.3(c). For Zn as high as 10%, the Zn-rich V phase regions

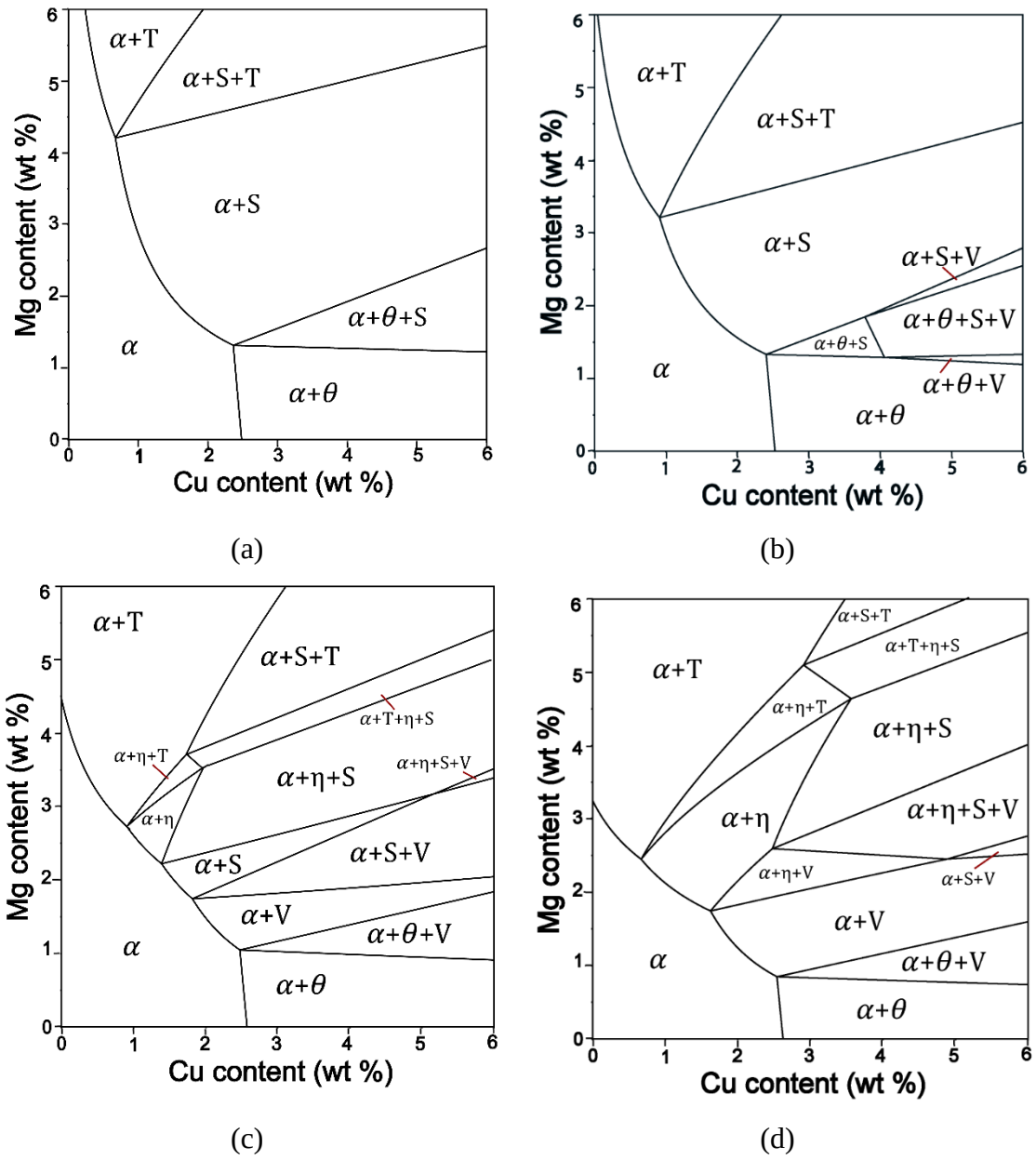

Figure 5.3: Effect of Cu and Mg on phase diagrams for (a) 4%, (b) 6%, (c) 8%, (d) 10% Zn at 45

expands. The as-cast and homogenized microstructures, as expected, show trends similar to these phase diagrams.

5.3 Effect of Composition on Evolution of Al_3Zr Dispersoids

Composition not only affects the microstructure in the interdendritic regions near the grain boundaries but also affects the microstructure within the grains. This happens due to difference in Zr concentrations across the grains brought in by microsegregation during casting. Zirconium has a very low diffusivity owing to which it is not "homogenized" even after prolonged durations of holding at homogenization temperature ranges. Presence of Zr above the solubility limits during homogenization causes the precipitation of Al_3Zr dispersoids whose number density and radius and hence the microstructure across the grains depends on the (a) initial Zr concentration; (b) solubility limits (c) nucleation and growth rates all of which are affected by composition. These in turn affect the homogenized microstructure which needs a uniform distribution of fine Al_3Zr dispersoids.

5.3.1 Effect on Zr Microsegregation in As-cast Microstructure

As the difference in dispersoid microstructure across the grains occurs due to the microsegregation of Zr that was caused during solidification, the microsegregation in the initial microstructure to start with for different compositions should be correct. In an earlier study by Robson and Prangnell[95] these initial as-cast microstructures were not considered leading to results which are different from that reported here. The microsegregations have been predicted from Scheil type calculations using Thermo-Calc™. The solidification of Al-Zn-Cu-Mg starts with crystallization of equilibrium $L1_2/DO_{23}$ Al_3Zr in the matrix followed by crystallization of the fcc α-Al phase. So, some Zr is lost in precipitating out these primary precipitates.

The equilibrium mass fraction of primary Al_3Zr (which is predicted by Thermo-Calc^{TM}) for various compositions investigated as seen in Figure 5.4(a), we find higher alloying contents lead to higher equilibrium mass fraction of DO_{23} Al_3Zr leading to less of it to remain in the matrix. This translates to the reduced amounts of Zr in the grain for higher Mg content (Mg is chosen for comparison) as seen in Figure 5.4(b). The same has been observed for other alloying elements but the effect is prominent for Mg.

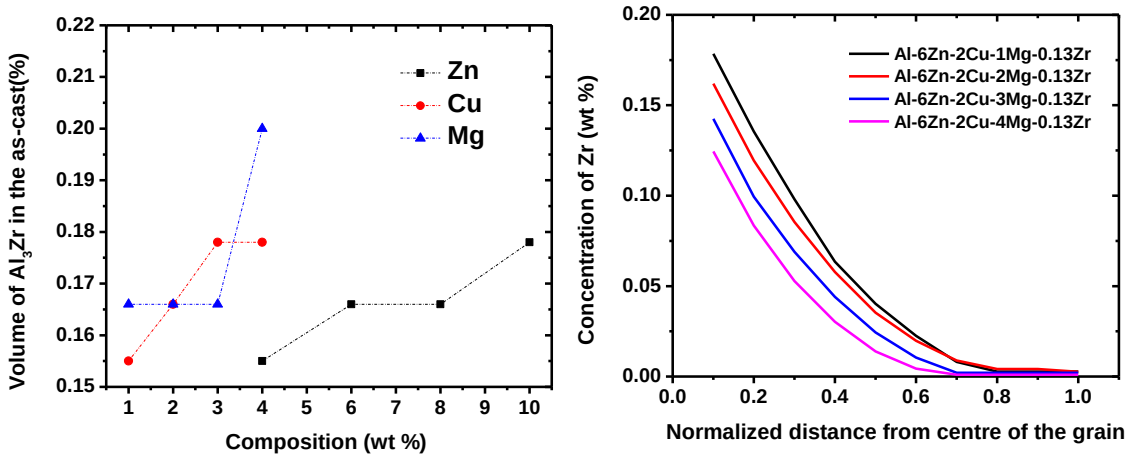

(a) (b)

Figure 5.4: (a) Variation of volume fraction of Al_3Zr in the as-cast state with composition for the baseline case of Al-6Zn-2Cu-2Mg-0.13Zr predicted by Thermo-Calc^{TM} (b) Composition of Zr across the SDAS for variation of Mg

5.3.2 Effect on Thermodynamics and Kinetics of Precipitation

The solubility limits of Zr in the fcc α-Al matrix decides the amount of precipitation that occurs. The change in fcc α-Al phase solvus with increasing Mg concentration is shown in Figure 5.5(a). It is seen that the solubility of Zr decreases with increase in Mg content of the alloy leading to higher supersaturation and higher driving force for Al_3Zr

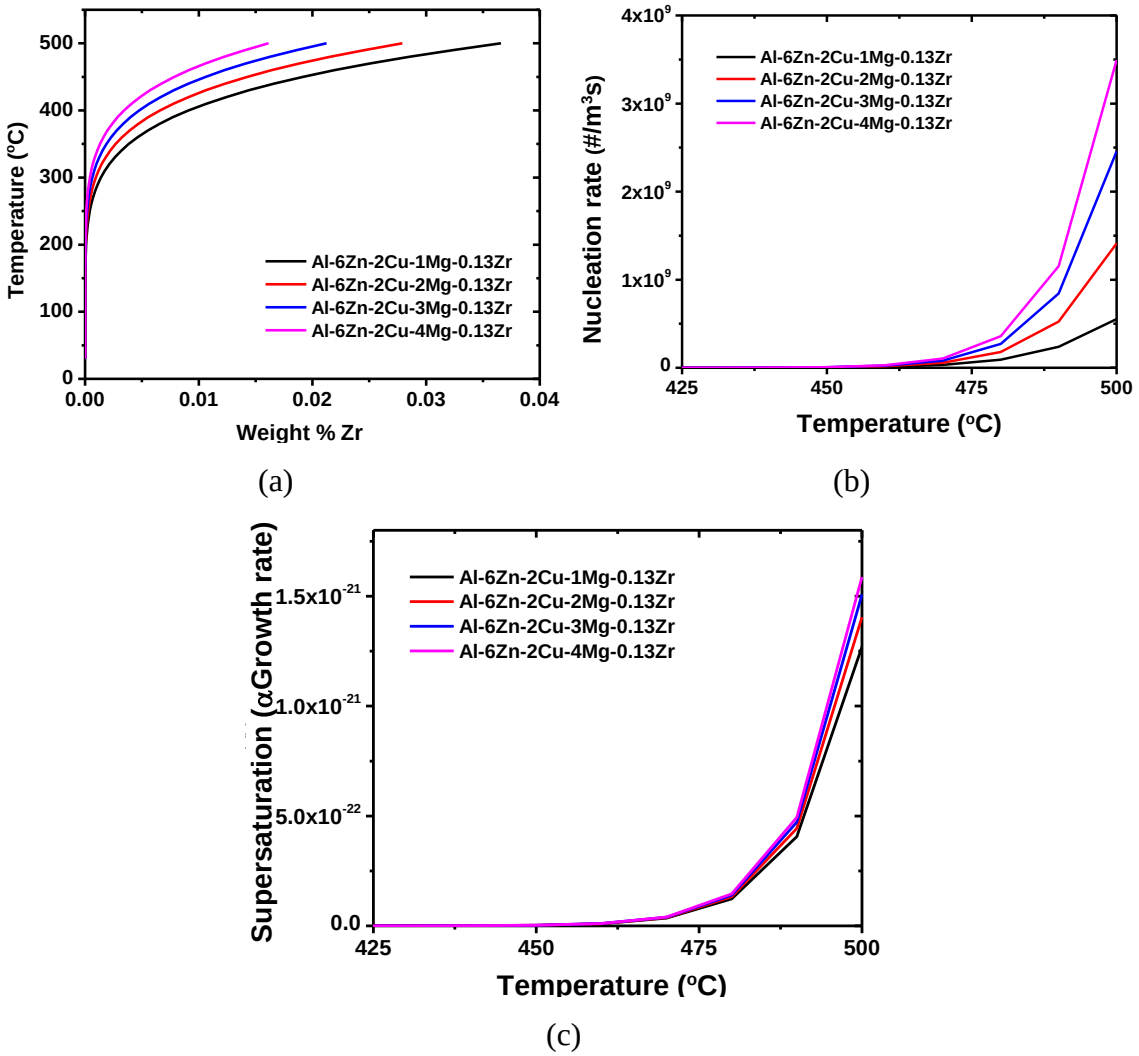

Figure 5.5: Variation of (a) supersaturation, (b) nucleation, (c) growth rates for varying amounts of Mg for the baseline case of Al-6Zn-2Cu-2Mg-0.1

nucleation and growth. The same trend is true for increasing Cu and Zn compositions. However, Mg has a greater influence on solubility limits as compared to Zn or Cu.

The nucleation and growth rates for various compositions in the order of increasing Mg content for various temperatures is shown in Figure 5.5(b) and (c) respectively. Both the nucleation and growth rates increase with increasing temperatures owing to increased diffusivity at higher temperatures which is characteristic of heterogeneous nucleation and growth. The nucleation and growth rates for different compositions, do not vary till a temperature of 450°C, after which increased Mg compositions lead to increase in both nucleation and growth rates as seen in Figure 5.5(b) and (c). To study the effect of composition on dispersoid precipitation, two temperatures of 450°C and 470°C have been chosen pertaining to the regimes with no and some difference in nucleation and growth rates.

5.3.3 Effect on Dispersoid Precipitation

The effect of varying amounts of Zn, Cu, Mg and Zr on the microstructure (number density and radius of dispersoids) across the grains about the baseline case of Al-6Zn-2Cu-2Mg-0.13Zr has been shown in Figure 5.6. The number densities and mean radii of the dispersoids at temperature of 450°C on homogenization for 30 hrs ((a),(c),(e)) and 470°C on homogenization for 5 hrs ((b),(d),(f)) have been compared. It can be seen that both the number densities and mean radii decrease with increasing amounts of Zn, Cu and Mg. While both of them increase with increasing amount of Zr. This is true for both the temperatures, 450°C pertaining to regime with no difference in nucleation and growth rates and 470°C pertaining to the regime with difference in nucleation and growth rates as can be seen in Figure 5.5(c) and (d).

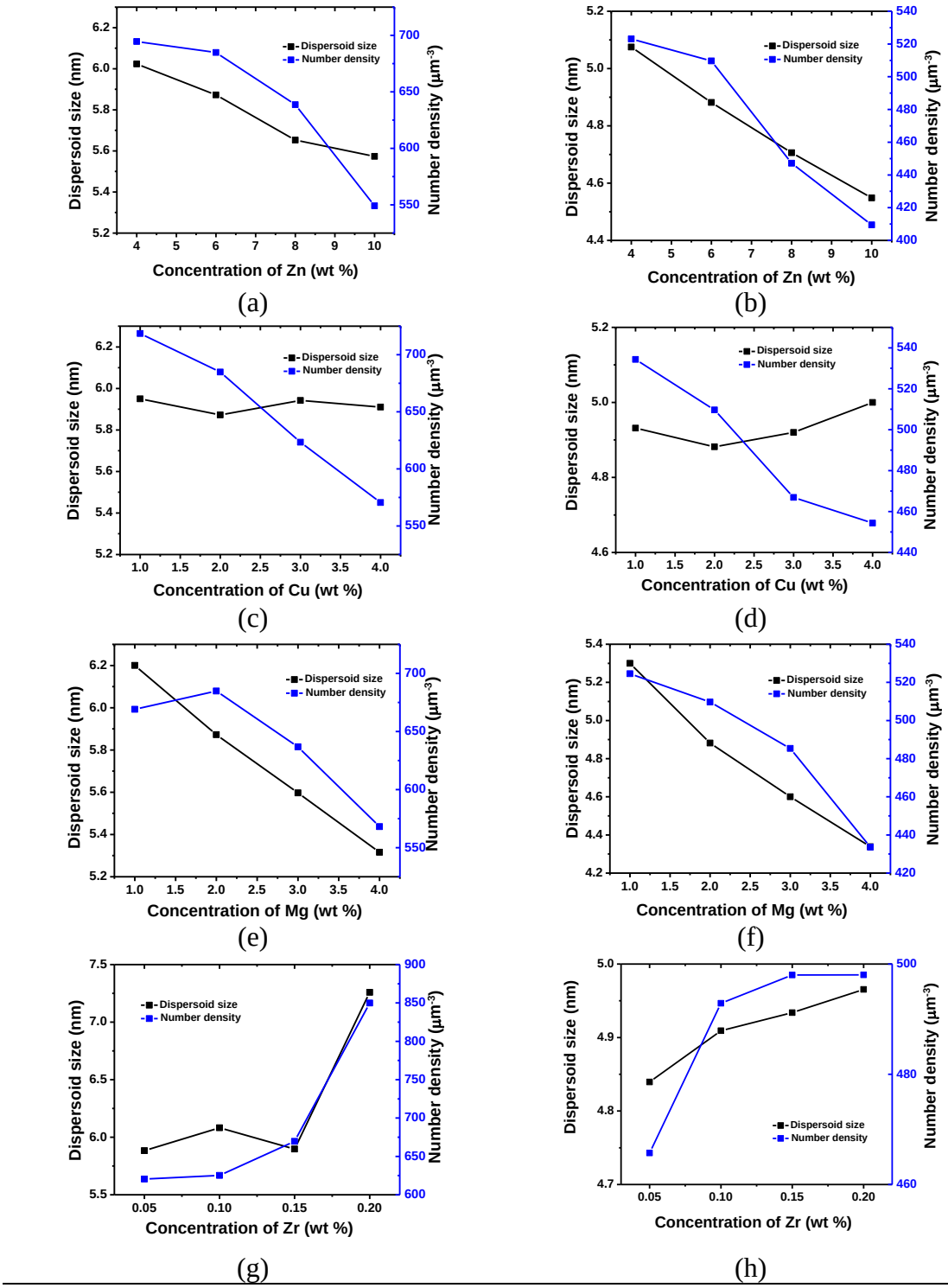

Figure 5.6: Effect of composition on number density and mean radius of the dispersoids (a),(b) Zn; (c),(d) Cu; (e), (f) Mg; (g),(h) Zr for homogenization at 450°C for 30 hrs and 470°C for 5 hrs.

The trend observed in this study is reverse to the trend observed by Robson and Prangnell[95] who did not consider the initial microsegregation of Zr in the as-cast microstructure. Although the solubility of Zr is decreased with increasing alloy content leading to increase in nucleation and growth rates, the availability of lesser amount of Zr across the grains with increasing alloying content restricts both the number density and mean radii. Thus the initial microsegregation is very crucial in determining the effect of composition on dispersoid precipitation.

The effect of Zr content on microstructure on homogenization at the two temperatures can be seen in Figure 5.6(g) and (h) respectively. It can be seen that at 450°C, the mean radius of the dispersoids sees a sharp increase after 0.15% Zr, which is not desirable as a very fine distribution of dispersoids is required to pin grain boundaries. Also, both the number density and mean radius seem to saturate after 0.15% leading to no gain in benefits of adding more Zr above 0.15% Zr.

5.4 Experimental Validation

To study the effect of composition on microstructure, Sun et al.[102] performed experiments on two separate samples with different compositions. The alloy of composition Al-6.2Zn-2.4Cu-2.3Mg-0.13Zr was first statically cast, and then remelted and directionally solidified. Due to segregation of the alloying elements, a solute lean top and a solute rich bottom of the directionally solidified sample was acquired which was homogenized. It should be noted that Zr content was less in the bottom while it was more in the top sample due to a partition coefficient of 1.4 which is unlike other alloying elements which have a partition coefficient less than 1.

The exact composition of the samples from EDX/OES methods is Al-5.1Zn-1.4Cu-2.2Mg-0.11Zr for the bottom sample and Al-6.6Zn-3.4Cu-4.3Mg-0.03Zr for the top sample. The DS top and bottom samples were homogenized for 5hrs at 420°C and for 24 to 40 hrs at 480°C.

Numerical test cases were set up pertaining to the compositions of the two samples and were run for the homogenization schedule that had been experimentally provided. The initial microstructure was chosen as predicted by Thermo-Calc™. The comparison of the microstructure at the two length scales is provided in Table 5.3. It can be seen that the results for dispersoids are within the experimental errors. The average size of the dispersoids are higher because of the larger dispersoids which might have been formed during directional solidification. Also images of dispersoid rich zones have been analyzed which might lead to overprediction of the number densities. The model predicted melting for the DS top sample while it predicted full dissolution of the interdendritic particles for the bottom sample. The discrepancy for the top sample may be because of the variation of melting point of the remnant S phase in the sample which seems to be higher for the sample than that predicted by Thermo-Calc™ as no melting was observed in the sample.

The recrystallization behavior of these two samples have been compared by Yiwei et al.[102] and in spite of the higher Zr in the bottom sample, it was found to be less resistant to recrystallization. This can be attributed to the coarser dispersoids found for this sample which has also been predicted by the model.

Table 5.3: Comparison of the predicted and experimentally measured microstructure of the DS Top and DS Bottom samples after homogenization for 5hrs at 420°C and 24hrs for interdendritic phase 40hrs for dispersoids at 480°C.

	DS Top		DS Bottom	
	Experimental	Numerical	Experimental	Numerical
Interdendritic phases				
Volume fraction (%)	1.5±0.89	Melting	1.0±0.97	0
Al_3Zr dispersoids				
Number density (/μm^3)	725	528	826	583
Mean diameter (nm)	28.5±12.4	15.2	37.1±20.0	17.7

5.5 Improved Composition Ranges

This study is helpful in throwing light on the effect of composition on as-cast and homogenized microstructures for Al-Zn-Cu-Mg-Zr alloys. The composition affects the as-cast microstructure by affecting the volume fraction of interdendritic phases and microsegregation which affects the microstructural evolution during homogenization and subsequent processing. More alloying elements in general increase the amount of interdendritic phases which increase the amount of homogenization time needed to minimize them. We need an optimum amount of alloying elements to take advantage of them and for ease of processing.

Increasing Zn increases the time needed for homogenization. However, Zn above 6 minimizes S phase considerably but leads to other phases like T and V in the as-cast microstructure, which need to be dissolved before extrusion and age-hardening by homogenization at higher temperatures. Having Zn higher than 8% leads to very high alloying element content increasing the quench sensitivity of the alloy requiring high

cooling rates to subdue precipitation which can induce residual stress and is also difficult to attain for thick forgings. So, a Zn content of 6-8% with Zn/Mg ratio of 3-4 is desirable.

High Cu or Mg increases the S phase that remains after homogenization which is difficult to dissolve. Low Cu and Mg (~1%) leads to easy homogenization with no detrimental interdendritic particles which is desirable. However, they are both needed for good mechanical properties of the alloy. The desirable Cu and Mg content is in the range of 1-2% with Mg:Cu of 1-2.

The composition of Zn, Cu and Mg affect the amount of primary Al_3Zr precipitated during solidification, leaving remaining Zr available for precipitation of fine dispersoids during homogenization. These precipitates formed during solidification are coarse and incoherent, and hence undesirable. In general increase in alloying content increases the tendency for precipitation during solidification leading to fewer fine coherent dispersoids at high alloy contents. This is however the reverse, if cooling during solidification exceeds a critical cooling rate leading to less or no precipitation of Al_3Zr. Alloying elements decrease the solid solubility of Zr leading to higher volume fractions of metastable Al_3Zr which is desirable. But this advantage can be taken only when we can prevent Al_3Zr from precipitation during solidification. No significant gain in number density or mean radius observed above 0.15% Zr at both temperatures investigated in the study. Hence a Zr content of 0.1-0.15% is the optimum range to attain fine distribution of numerous metastable coherent Al_3Zr dispersoids.

5.6 Conclusion

The model developed in CHAPTER 4 is used to study the effect of composition on microstructural evolution during homogenization in 7XXX alloys. A microstructure with

minimum S and uniform distribution of fine, coherent Al_3Zr dispersoids is desired after homogenization. The composition affects the volume fraction of secondary particles and microsegregation during solidification which has a profound effect on the microstructure during homogenization and subsequent processing. Higher Zn, Cu and Mg contents lead to higher amounts of interdendritic particles and hence require more time to homogenize. Higher alloying content also leads to increased quench sensitivity. Higher alloy content also leads to decrease in solid solubility of Zr leading to higher driving force for nucleation of dispersoids. This is however, possible only when the cooling rate during solidification is fast enough to prevent primary Al_3Zr from nucleating. These precipitates are coarse and incoherent and decrease the amount of Zr needed for precipitation of dispersoids which is undesirable. For solidification otherwise, higher alloying content leads to lower number densities for dispersoids. This result contradicts previous studies by Robson and Prangnell[95], who did not take the initial solidification microstructure into consideration.

Based on the study an improved composition range of 6-8%Zn, 1-2%Cu, 1-2%Mg and 0.1-0.15%Zr has been suggested. It should be noted that these suggestions are made solely based on ease of homogenization and extrusion, and so, are closer to composition of the AA7075 alloys except for higher Zn and also closer to the AA7050 except for lower Cu. Copper in the range of 2-2.5% is intentionally added to AA7050 to improve its fracture toughness and corrosion resistance which has not been taken into account.

CHAPTER 6. MICROSTRUCTURE DUE TO PRECIPITATION DURING COOLING OF 7XXX ALLOYS

6.1 Introduction

Aluminum 7XXX alloys fall in the category of heat-treatable alloys which derive mechanical strength through the age-hardening heat treatment. Prior to age hardening the processing steps after the metal is cast consist of homogenization to get rid of microsegregation, low melting interdendritic particles, and precipitate dispersoids, followed by thermo-mechanical processing such as extrusion or hot rolling. The metal is then solution treated to reach a supersaturated solid solution prior to aging when precipitation of strengthening particles occurs. Each high temperature processing step is followed by cooling to room temperature. While we have some understanding of the microstructural evolution during these processes, less information is in the literature about its behavior during the subsequent quenching. The microstructure after quenching is the initial condition for the next processing step and determines the mechanical properties.

Precipitation during cooling in 7XXX alloys is important and has been studied by many researchers. Early studies on precipitation in 7XXX series observed η/M (Description of the phases in appendix B) phase precipitation on previous Zr or Cr based dispersoids[99,105]. Precipitation of only the η phase has also been reported by a recent study on a 7A09 alloy[106]. However, precipitation of the S and T phases were reported by Godard et al.[14] Godard reported heterogeneous nucleation of η on dispersoids at higher

temperatures followed by precipitation of metastable S' and T on grain boundaries, sub-grain boundaries, and dislocations at intermediate temperatures and homogeneous nucleation of metastable η' at low temperatures during cooling of an AA7010 alloy. Robson[107] reported the precipitation sequence in AA7050 through step quenching experiments and microstructural examination. He reported a complex precipitation sequence of S' needles within grain, followed by M phase within the grain and S phase at the grain boundaries, followed by numerous metastable M' needles in the grain at lower temperatures during slow cooling of AA7050. Controlling the precipitation of these phases by controlling the composition of an AA7175 alloy has been suggested by Lim et al[13].

A microstructure ideal for ease of extrusion without recrystallization should be free from all precipitates. S phase has a solvus temperature of 493°C, which is close to the melting temperature and is so very difficult to dissolve during pre-heat. All the phases precipitated during cooling have low melting temperatures and can easily melt during extrusion. They also hamper the age-hardenability of the alloy. They should therefore, be fine enough to dissolve during pre-heat. According to McQueen and Celliers[108] particles of size >0.6μm do not dissolve during preheat. Also, any precipitates with size >1μm leads to particle stimulated nucleation of recrystallization[108].

In this work we aim to do a comprehensive study of precipitation during cooling over a range of cooling rates relevant to the industrial practice and a range of compositions belonging to the 7XXX alloys. The aim here is to minimize the precipitation during cooling and to have precipitates smaller than 0.6μm. We choose a numerical approach in this work, first validating our initial results with experiments. We have developed a Particle Size Distribution (PSD) based numerical approach to model precipitation of multiple phases

during cooling from homogenization temperature of 7XXX alloys. This model is used to study the effect of cooling rates and compositions. Continuous Cooling Curves (CCC) and Time Temperature Transformation (TTT) curves are also predicted for AA7050.

6.2 Domain Description

The numerical domain is a 1D radial domain similar to the precipitation model in CHAPTER 3, as shown on Figure 3.1(b). As precipitation of 4 different phases are modeled, 4 such domains are considered one for each phase. Four precipitate classes: S (Al_2CuMg),η ($MgZn_2$), T($Al_2Zn_3Mg_3$), and Θ (Al_2Cu) phases are considered in the study as these phases have been found in the experimental studies[13,109] and also predicted by Thermo-Calc™. These phases S, η and T, are plate/needle-shaped[13,107] and are assigned these experimentally observed morphologies in the model. The values of the various constants in the numerical model for the four phases have been listed in Table 6.1.

Table 6.1: The phases and property values for the phases used by the numerical model

Phases	S, η, T, Θ
Molar volume (m^3/mole)	1×10^{-5}
Interfacial energy (J/m^2)	0.18
Aspect ratio	10

6.3 Experimental Validation

Precipitation of the S, η, T and Θ phases is predicted by ThermoCalc™ during cooling of the baseline composition of Al-6.2Zn-2.3Cu-2.35Mg-0.13Zr. The phases precipitated were characterized through Energy Dispersive Spectroscopy (EDS) mapping,

X-Ray Diffraction (XRD) and Differential Scanning Calorimetry (DSC) during cooling an Al-6.2Zn-2.3Cu-2.35Mg-0.13Zr alloy in the furnace.

An Al-6.2Zn-2.3Cu-2.35Mg-0.13Zr alloy was induction melted in vacuum and cast in cylindrical copper molds of size 10cm length and 2.5cm diameter. This cylindrical ingot was then cut into smaller samples and homogenized in the box furnace for 10 hrs at 420°C to precipitate the Al_3Zr dispersoids, 4hrs at 470°C to dissolve the aluminides and 16hrs at 480°C to minimize the S phase as proposed in CHAPTER 4. These samples are then furnace cooled by letting the sample remain in the furnace which had been switched off. The samples are then polished using silica papers and colloidal silica and observed under a Phenom ProX Desktop Scanning Electron Microscope (SEM).

Figure 6.1 shows the microstructure of furnace cooled sample and the corresponding EDS mapping. Abundant plate-like precipitates are observed in the furnace cooled sample. The coarser particles at the grain boundaries are the remnant S phase also indicated by the XRD plot for the homogenized sample as seen in Figure 6.2(a), after three step homogenization with some Zn solubility. There are smaller disk shape precipitates near the grain boundaries (look like small rectangles) with Mg, Zn and Cu solubilities may be the η phase precipitates. There are finer and longer precipitates within the grains seem to have Cu with little or no Zn may be the S phase or the Θ phase.

To better characterize the phases precipitated XRD and DSC runs were also conducted on the as-cast, homogenized/water quenched, and homogenized/furnace cooled samples. The XRD plot in Figure 6.2(a) shows peaks corresponding to mostly η in as-cast, mostly S in homogenized and both the phases in furnace cooled samples. Other phases may have precipitated but at volume fractions too small to be detected by XRD. Figure 6.2(b)

shows the DSC plot of the as-cast sample with an endothermic peak corresponding to the aluminides present in the as-cast microstructure. The homogenized/water quenched sample shows the onset of dissolution of the S phase while the furnace cooled sample shows the onset of the dissolution of the η and S phases. These peaks were also observed by Shu et al.[101]

The number density of the precipitates was calculated using the mean projected height technique[87] for disc-like precipitates where the mean projected height of the particles is

$$\overline{H'} = \pi r/2. \tag{6.1}$$

The number of particles per unit area, which is calculated from the 2D SEM micrographs, then translates to the number of particles per unit volume using the relationship:

$$N_V = \frac{N_A}{\overline{H'}}. \tag{6.2}$$

The plate radius for the particles was calculated using the relationship:

$$r = \frac{N_L}{N_A}. \tag{6.3}$$

A test case corresponding to the cooling experiment for the composition of Al-6.2Zn-2.3Cu-2.35Mg-0.23Zr was run using the numerical model. The cooling rate selected was 130°C/hr which corresponds to our furnace cooling conditions, as measured by Sun et al.[59] The model predicts precipitation of coarse S, η T and Θ phases, some of which have been experimentally verified as seen in Figures 6.1 and 6.2. The number density and mean platelet lengths are listed in Table 6.2. The total number density of the particles found experimentally using the projected image technique stated above was $3.1\times10^{20} \pm 2.2\times10^{19}$ /m^3, which is of the same order of magnitude of the predicted total number density. The

predicted number density is very sensitive to the total number of nucleation sites which has been taken as 1×10^{22} /m^3 which may be less than the actual number of nucleation sites available. The mean platelet length is 3.04μm which is very less compared to 0.31μm (for visible plates >0.1 in length) found numerically which is very sensitive to surface energy values. The variation is also observed because not all the precipitated particles were plate like. The experimental number density and mean platelet length corresponds to all the precipitates visible in the micrographs as it is difficult to visibly characterize the different phases. Here we try to make a semi-quantitative study of the effects of cooling rates and composition on precipitation response of 7XXX alloys during cooling.

Table 6.2: The predicted number densities and mean platelet lengths for the different precipitated phases.

Phase	Number density (/m^3)	Mean platelet length (μm)
Al_2CuMg (S)	6.3×10^{19}	0.16
$MgZn_2$ (η)	6.6×10^{20}	1.2×10^{-2}
Al2Mg3Zn3 (T)	1.5×10^{18}	4.0×10^{-3}
Al_2Cu (Θ)	6.7×10^{15}	4.0×10^{-3}
Total/Mean	7.2×10^{20}	0.02

6.4 Numerical Results and Discussion

The baseline case for this study is an AA7050 alloy with composition 6Al-6.2Zn-2.3Cu-2.35Mg-0.13Zr, although the role of Zr is only to precipitate dispersoids as discussed in CHAPTER 4. The test cases run to study the effect of cooling rates are listed in Table 6.3. The different test cases run to study the effect of composition are listed in Table 6.4.

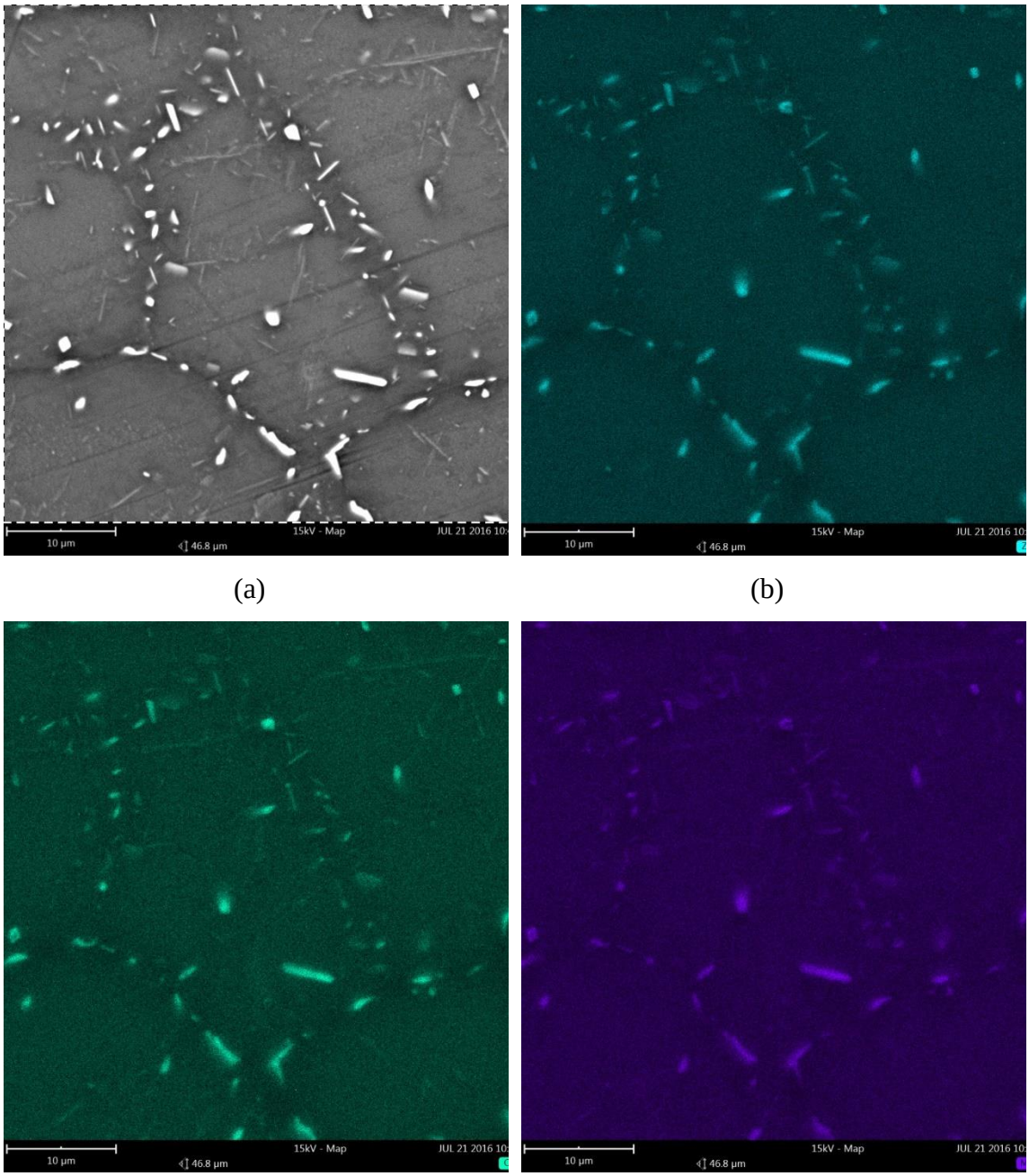

(a) (b)

(c) (d)

Figure 6.1: (a) Back scattered electron image of a homogenized and furnace cooled Al-6.2Zn-2.3Cu-2.35Mg-0.13Zr; EDS mapping for (b) Zn; (c) Cu and (d) Mg.

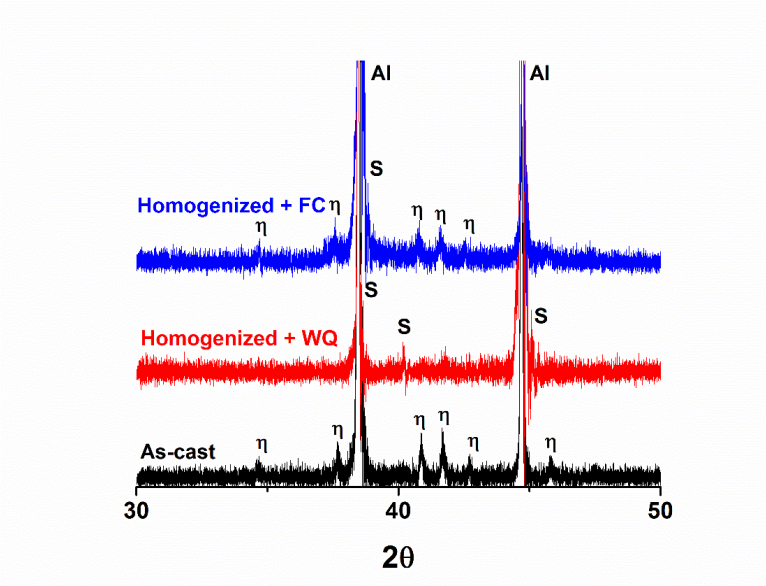

(a)

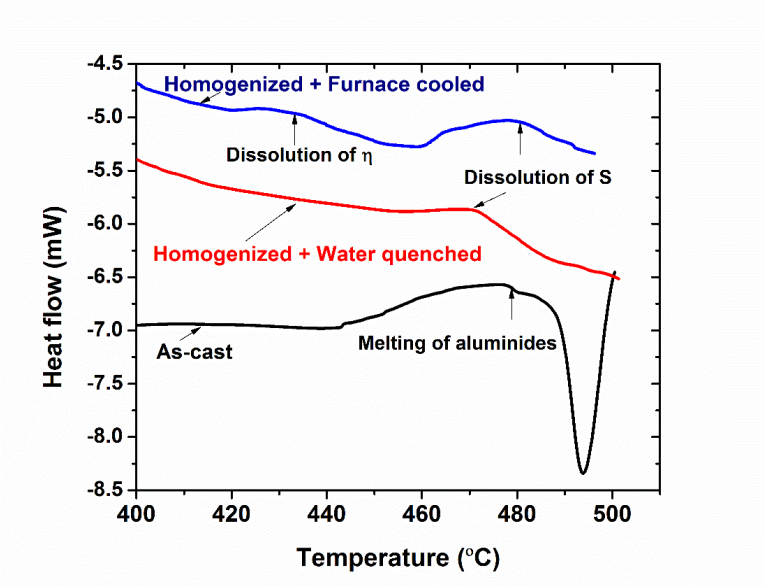

(b)

Figure 6.2: (a) XRD plot of the Al-6.2Zn-2.3Cu-2.35Mg-0.13Zr as-cast, homogenized/water quenched and homogenized/furnace cooled samples (b) DSC plots for the same indicating the onset temperatures of listed processes.

Table 6.3: Test cases run to study the effect of cooling rates on precipitation

	Cooling rate (°C/hr)	Zn(wt%)	Cu(wt%)	Mg(wt%)	Zr(wt%)
1	150	6.2	2.3	2.35	0.13
2	250	6.2	2.3	2.35	0.13
3	500	6.2	2.3	2.35	0.13
4	1000	6.2	2.3	2.35	0.13

Table 6.4: Test cases run to study the effect of composition on precipitation

	Cooling rate (°C/hr)	Zn (wt%)	Cu (wt%)	Mg (wt%)	Zr (wt%)
1	250	4	2	2	0.13
2	250	6	2	2	0.13
3	250	8	2	2	0.13
4	250	10	2	2	0.13
5	250	6	1	2	0.13
6	250	6	3	2	0.13
7	250	6	4	2	0.13
8	250	6	2	1	0.13
9	250	6	2	3	0.13
10	250	6	2	4	0.13

The CCC are plotted based on test cases for the composition of Al-6.2Zn-2.3Cu-2.35Mg-0.13Zr for cooling rates of 0.01, 0.1, 1, 10 and 100°C/s. The TTT curves are plotted for the same composition at isothermal temperatures of 100, 150, 200, 250, 300, 350, 400 and 450°C.

6.4.1 Effect of Cooling Rates

The model predicts precipitation of S (Al_2CuMg), η ($MgZn_2$), T ($Al_2Mg_3Zn_3$) and Θ (Al_2Cu) phases during cooling in the range of 150-1000°C/hr. The number density

evolution of each of the phases with time, is shown in Figure 6.3. The precipitation can be categorized into three temperature ranges:

(i) High temperature precipitation: S phase solvus (494°C for composition of Al-6Zn-2Cu-2Mg-0.13Zr) is the highest and so it precipitates first. Precipitation of S phase is very fast and occurs mostly at temperatures above 400°C.

(ii) Medium temperature precipitation: The η phase (solvus temperature of 423°C for composition of Al-6Zn-2Cu-2Mg-0.13Zr) precipitates at temperatures ranging from 300 to 400°C.

(iii) Low temperature precipitation: Cooling to temperatures below 200°C leads to supersaturation and diffusion enough to precipitate the T and Θ phases (solvus temperatures of 174°C and 80°C respectively, for composition of Al-6Zn-2Cu-2Mg-0.13Zr).

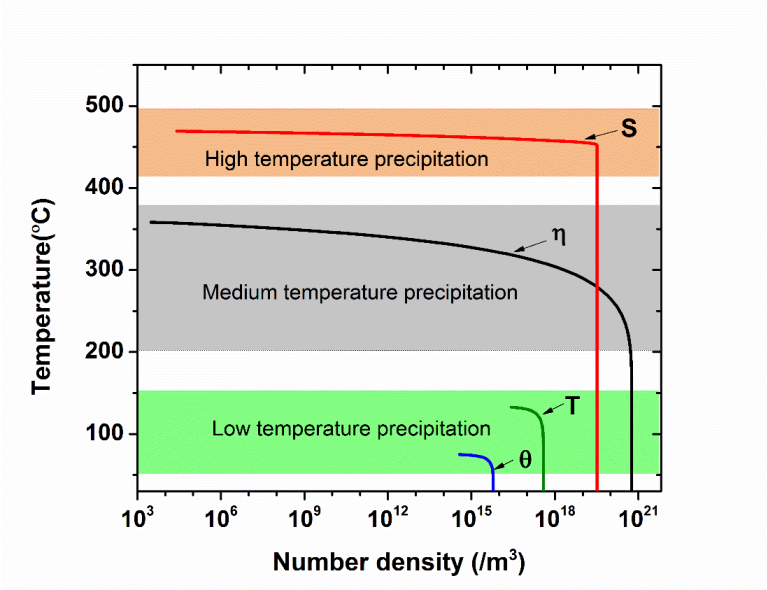

Figure 6.3: The evolution of predicted number densities of various phases precipitated showing the temperature ranges of precipitation

As the S phase nucleates first at a high temperature it gets ample time at high temperature for diffusion to occur leading to longer platelets as compared to other phases as seen in Figure 6.4(a). The length of the precipitates decrease with increasing cooling rate, as the time available for growth is smaller for higher cooling rates.

The number density of the S phase increases with decreasing cooling rate as seen in Figure 6.4(b), because higher cooling rates lead to higher supersaturation before precipitation begins, but still at high enough temperature to have significant diffusion. However, this is not true for other phases where the number densities decrease with cooling rate as these phases have a lower solvus where diffusion is extremely slow leading to nucleation (requiring local rearrangement of atoms through diffusion) of lesser precipitates. There is a crossover of maximum number of precipitates from S to η phase at cooling rates lower than 650°C/hr. At higher cooling rates although the S phase precipitates are more, they are smaller in length. The Θ phase here, is the last to precipitate and has the minimum number density.

The volume fraction of S phase shows little change in the range of 150-1000°C/hr while it decreases for other phases as seen in Figure 6.4(c). As the volume fractions do not vary much with cooling rates, the composition of the matrix does not vary with cooling rates, leading to flow stresses insensitive to cooling rates in the range of 150-1000°C/hr.

Figure 6.4(d) shows the predicted size distribution of the platelets of η and S for the 4 cooling rates studied. It can be seen that the average size of the platelets decreases with increasing cooling rates. Also, as S phase platelets get enough time at higher temperatures leading to higher growth facilitated by diffusion, they are larger than the η phase platelets which have less time to grow.

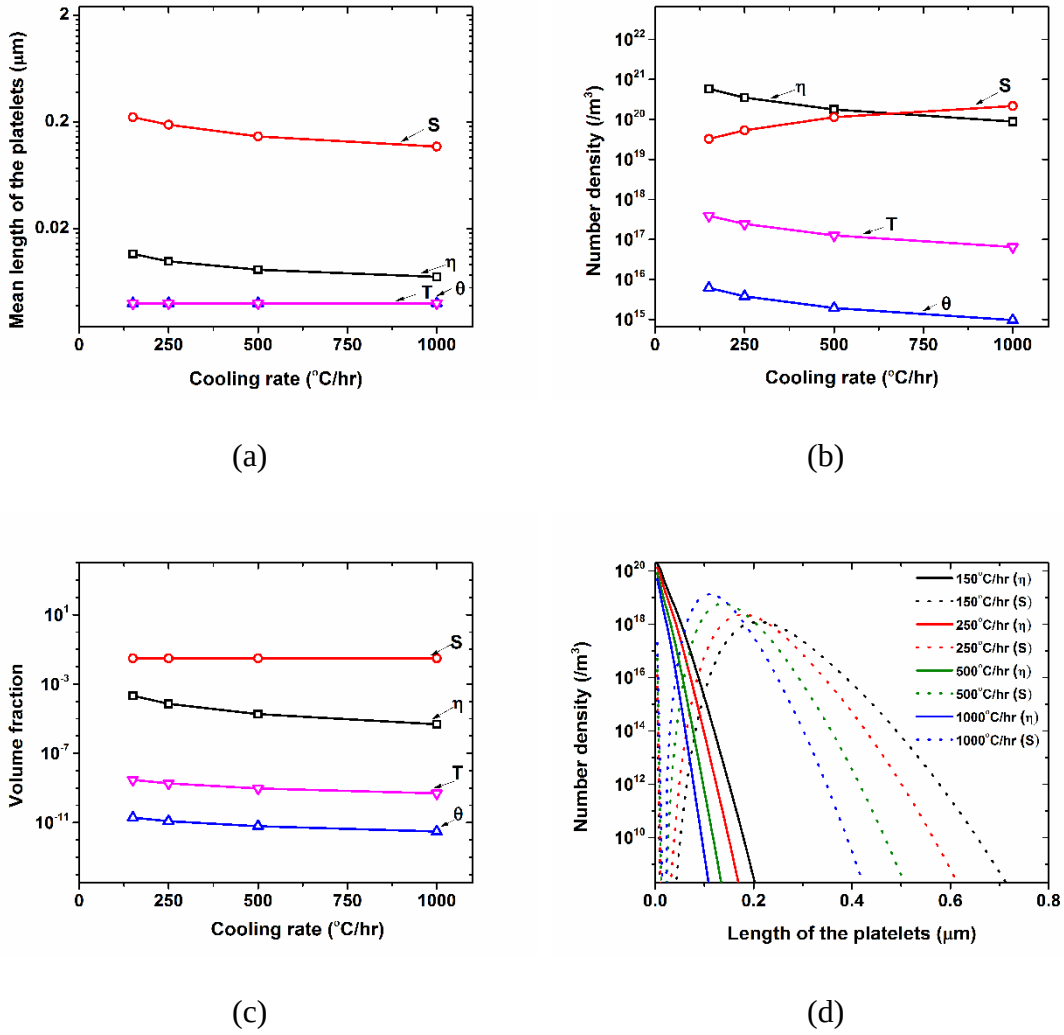

Figure 6.4: Effect of cooling rates on (a) mean length of platelets (b) the number density (c) volume fraction and (d) size distribution of different precipitated phases.

6.4.1.1 *Continuous Cooling Curves*

Figure 6.5 shows the cooling curves for the Al-6.2Zn-2.3Cu-2.35Mg-0.13Zr (AA7050), as predicted by the numerical model for cooling rates varying over a range of 4 orders of magnitude. The curves have the start (solid lines) and end temperatures (dashed lines) of the precipitation of different phases through high, medium and low temperature precipitation reactions. The start temperature is when number density for that particular phase has its first non 0 value and the end temperature, when it becomes constant. The nucleation is not evenly distributed over the range of temperatures shown. The nucleation rate is more initially and decreases with time.

The precipitation regions of the S phase start at lower temperatures at higher cooling rates due to the fact that higher supersaturation is needed to overcome slower diffusion for nucleation at lower temperatures. As nucleation and growth is limited, the supersaturation grows as the temperatures drop, leading nucleation continuing at lower temperatures at higher cooling rates, leading to a large S phase precipitation region at higher cooling rates. The number density of S phase is higher at higher cooling rates but they are finer in size due to limited growth. These smaller platelets more easily dissolve during preheating before extrusion. There is an overlap of the high and medium temperature precipitation reaction stages at higher cooling rates. The medium and the low temperature precipitation reactions begin early at higher cooling rates due to availability of solute in the alloy. No precipitation at temperatures below 50°C is observed.

The S (490°C), η(470°C), T(480°C) and Θ(540°C) phases are low melting temperature phases which, if they do not dissolve during preheat (> 0.6μm) , may melt during extrusion[6]. S phase is brittle and reduces the toughness of the alloy[97]. If larger than a critical size (>1μm) , they may also cause particle stimulated nucleation of recrystallization[15]. To have a favorable microstructure with precipitates < 0.6μm, the cooling rates need to be > 500°C/hr.

In case of cooling after solution heat treatment before aging, any S phase is undesirable as it might remain in the final microstructure. Elimination of S phase is possible if we quench the alloy at very high cooling rates. However, cooling at very high cooling rates causes residual stresses which may cause distortion or cracking. To minimize these

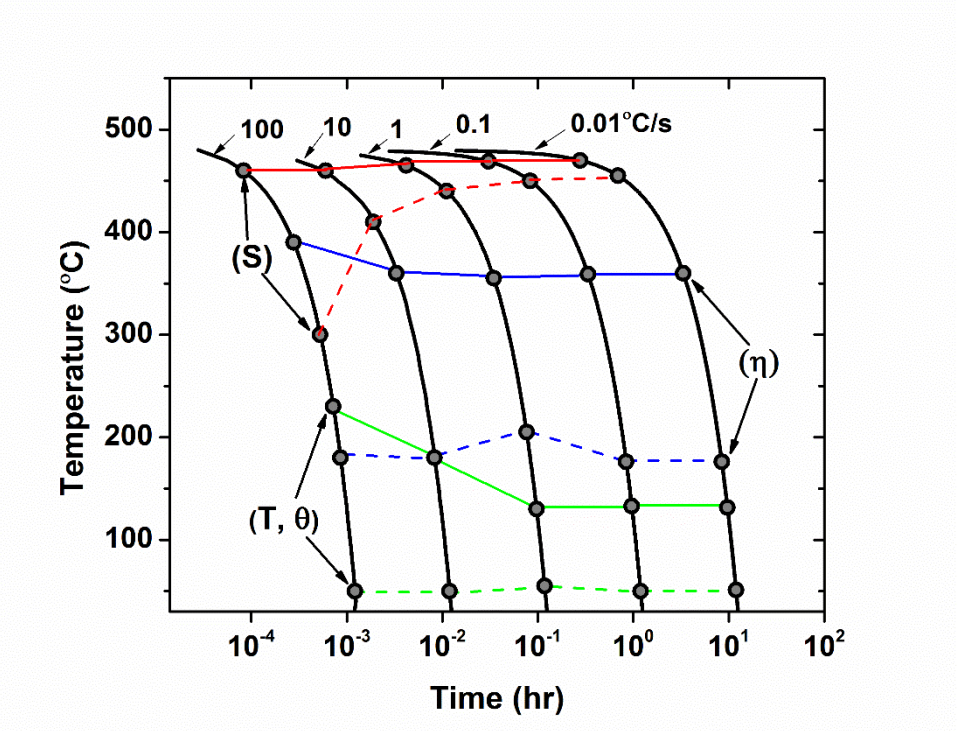

Figure 6.5: Simulated Continuous Cooling Curves for AA7050 showing the high temperature, medium temperature and low temperature precipitation regions. The solid lines showing the start temperatures and dashed lines showing the end temperatures of precipitation.

effects, warm water or glycol quenching has been proposed which is found to increase cooling rates with reduced residual stresses[110]. The glycol has a very high boiling point and does not form a vapor blanket stage but dissociates to form a residue which uniformly covers the section leading to uniform heat transfer all across the component which reduces residual stresses. The residue later dissolves at lower temperatures. Cooling at 10-100°C/s (36000-360000°C/hr) greatly reduces the unfavorable S phase, which remained the same for the cooling rate range of 150-1000°C/hr. A high cooling rate is highly desirable in the 300-480°C temperature range to avoid the high temperature S phase precipitation.

6.4.1.2 *Time Temperature Transformation Curves*

The numerical model was also used to predict the Time Temperature Transformation curves. Isothermal cases were run at several temperatures to note the precipitation volume fractions. Figure 6.6 shows the TTT curve for the precipitated S, η and T phases for AA7050 alloy. The red hollow circles indicate the time required to precipitate a volume fraction of 1% S during isothermal treatment in the temperature range of 250-450°C. As mentioned earlier the CCC also suggest very fast quenching in this temperature range to avoid S phase precipitation.

The η phase precipitates in the temperature range of 150-350°C, with the nose of the curve lying at approximately 275°C. The aging heat treatment is done to form fine metastable η' phase precipitates prior to the stable η precipitates. However, at this temperature, η' grows fast enough to transform into undesirable coarse stable η precipitates. η' precipitation also is accompanied simultaneously by the undesirable T phase precipitates,

occurring in the temperature range of 150-250°C. At temperature of 100-125°C, the TTT curve for η lies ahead of the curve for T phase. In this temperature range, supersaturation is high enough to precipitate numerous fine-sized metastable η' precipitates without precipitation of the T phase. This temperature range is hence ideal for aging of these alloys.

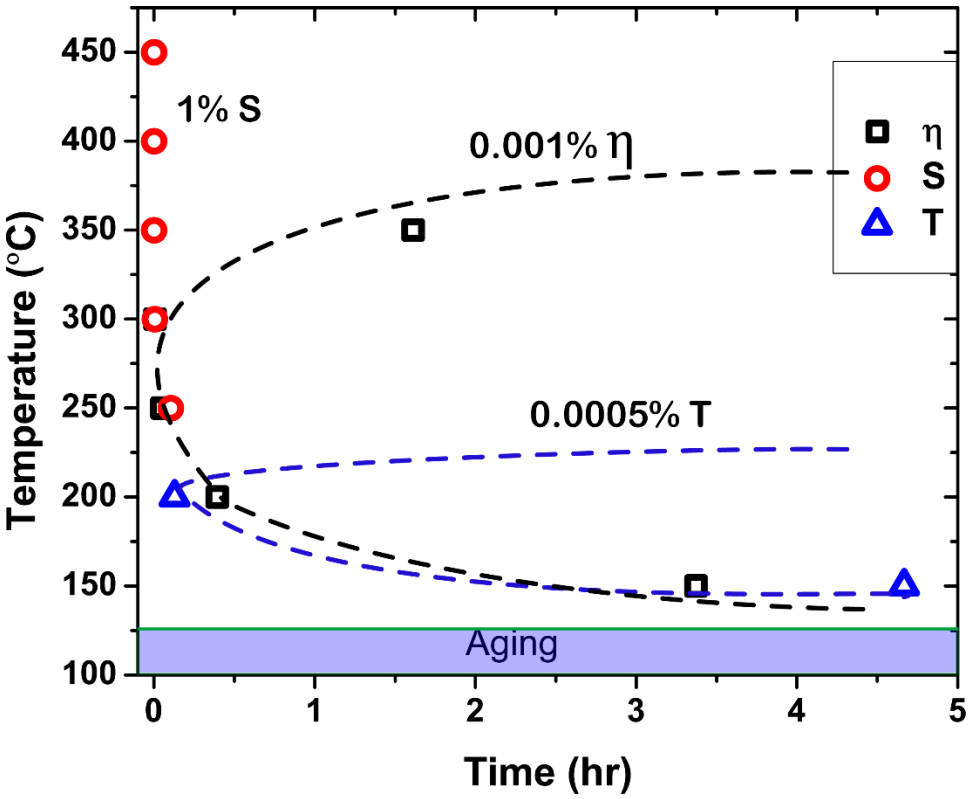

Figure 6.6: Time Temperature Transformation curves for AA7050 showing the time required for precipitation of 1% S, 0.001% η and 0.0005% T.

6.4.2 Effect of Composition

The effect of individual compositional variations of alloying elements Zn, Cu and Mg on the precipitation of different phases has been studied. The compositional variation

leads to change in the phase diagram, which leads to difference in the phases that precipitate including the formation of a new phase, V, which is a solid solution of Mg_2Zn_{11} and formed at higher Zn content.

Figure 6.7 shows the effect of increasing Zn, Cu and Mg contents on the stable phases in 7XXX alloys as predicted by Thermo-Calc^{TM} using the TCAL1 database. The base composition is Al-6Zn-2Cu-2Mg. As seen in Figure 6.7(a) for low Zn compositions (low Zn:Mg) lead to T phase stabilization which is Mg-rich, which is undesirable. Too much Zn stabilizes the Zn-enriched η and V phases which, also have a low melting point. The S phase, which is ideally Zn free diminishes at higher Zn contents. Θ is formed at low temperatures for Zn > 3% and is less harmful because its small size and higher melting point.

The effect of Zn on the precipitation behavior of 7XXX alloys in the range of 4 to 10 wt% is shown in Figure 6.8. The undesirable S phase is decreases in number and size due to lower supersaturation, with increase in Zn composition as seen in Figure 6.8(a) and (b). However, the Zn-rich, V phase is precipitated in large volume fractions (Figure 6.8(c)) at high Zn contents which is still undesirable. Also, increase in Zn leads to higher Cu and Mg contents (Figure 6.8(d)) in the alloy due to lower S (Al_2CuMg) phase volume fractions. Although higher Zn contents seems to be a good proposition for lower S phase precipitation, the undesirable V phase and the high flow stresses are deleterious. An intermediate Zn composition of 6-8% have more η and Θ which are less harmful than the other phases.

Figure 6.7(b) clearly indicates the expansion of the α-Al+S phase region with increase in Cu content. Low Cu content stabilizes the Mg and Zn-rich T ($Al_2Mg_3Zn_3$) phase,

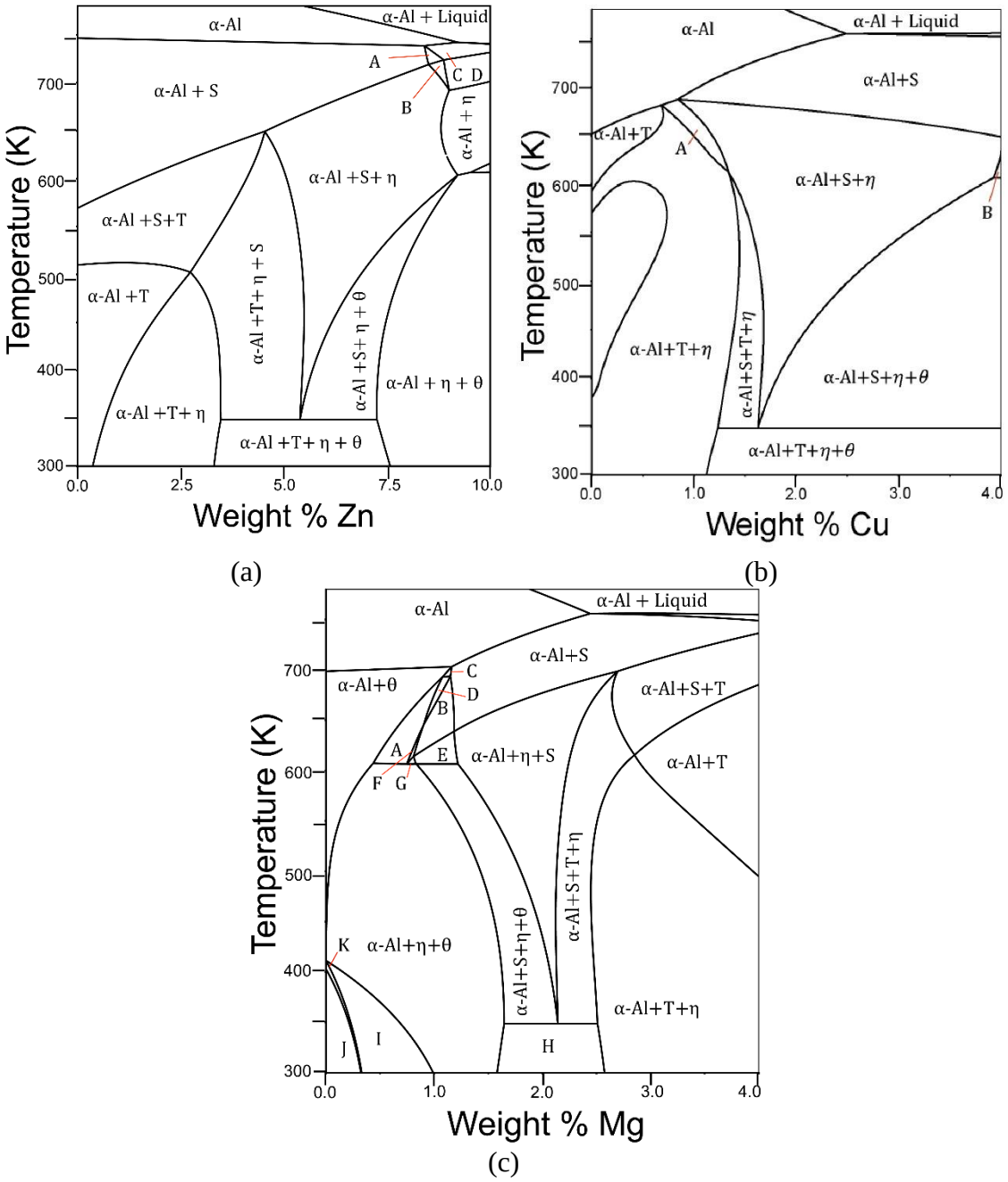

Figure 6.7: Phase diagrams corresponding to the Al rich corner of an Al-6Zn-2Cu-2Mg alloy showing the effect of (a) Zn (A: $\alpha - Al + S + V$;B: $\alpha - Al + S + \eta + V$; C: $\alpha - Al + V$; D: $\alpha - Al + \eta + V$); (b) Cu (A: $\alpha - Al + \eta$; B: $\alpha - Al + S + V + \eta$) and (c) Mg ($A$: $\alpha - Al + \theta + V$; B: $\alpha - Al + S + V$; C: $\alpha - Al + S + \theta$; D: $\alpha - Al + V$; E: $\alpha - Al + S + \theta + V$; F: $\alpha - Al + V$; G: $\alpha - Al + V + \eta$; H: $\alpha - Al + T + \theta + \eta$; I: $\alpha - Al + \eta + \theta + V$; J: $\alpha - Al + \eta$; K: $\alpha - Al + V + \theta$) on the stable phases at different temperatures.

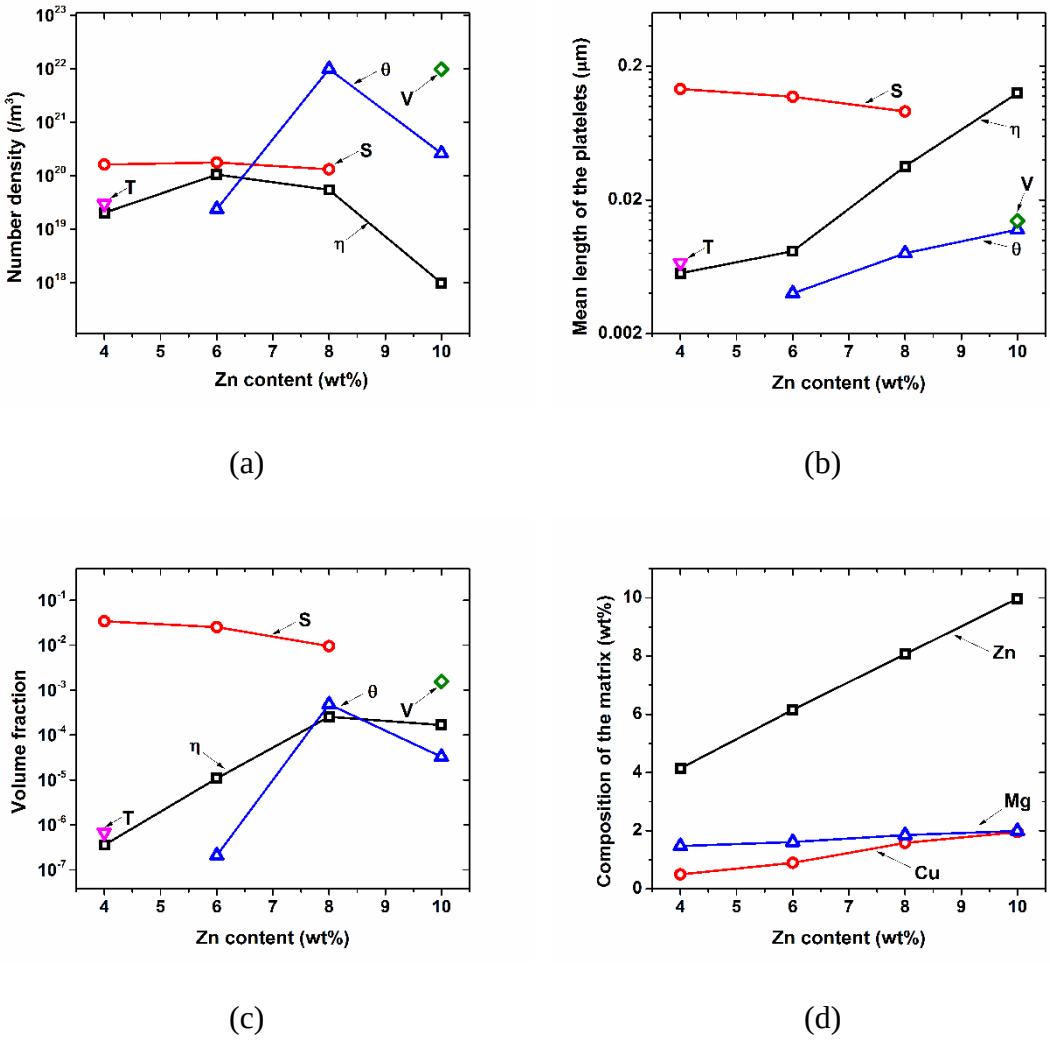

Figure 6.8: Effect of Zn content on (a) number density (b) Mean length of the platelets (c) volume fraction for different precipitated phases and (d) composition of the matrix.

which is replaced by the η phase, which has more Cu solubility than T. The Cu rich-Θ (Al_2Cu) phase appears at low temperatures for Cu >1%.

The effect of Cu content in a 7XXX alloy in the composition range of 1 to 4% is shown in Figure 6.9. The S phase number density increases sharply from 1% to 2% Cu content after which it is replaced by the Cu-rich Θ phase (Figure 6.9(a)). Also, higher Cu content leads to higher Zn content (Figure 6.9(d)) in the alloy due to lower η, with lower Mg due higher S phase volume fractions. Lower Mg leads to lower flow stresses during extrusion which is desired. However, the length of the S phase platelets and the volume fractions continue to increase due to higher availability of Cu (Figure 6.9(b) and (c)). The size of S phase reaches >0.6μm which is undesirable. Also at the other end, at very low Cu concentrations of 1%, the undesirable Mg-rich T phase exists which is again a nuisance. An Cu content of 1-1.5% (on the lower side) is therefore considered to be good for a precipitated microstructure with more η than S phase precipitates.

Figure 6.7(c) shows the effect of Mg content on the phases precipitated during cooling from the homogenization temperature of 480°C. High Mg stabilizes the η and T phases. At low Mg concentrations, Cu-rich Θ exists, which is replaced by the S and η phases with increased Mg solubility, as Mg content increases. At very high Mg contents, the Mg-rich T phase exists.

The effect of Mg content in the composition range of 1-4% in 7XXX series alloys has been shown in Figure 6.10. The number density of undesirable S phase decreases and η decreases, with increasing Mg content as seen in Figure 6.10(a). The trend reverses at higher Mg content of ~4%. However, the length of the S phase platelets increases with Mg and is the maximum for intermediate Mg contents of ~3% (Figure 6.10(b)) when the

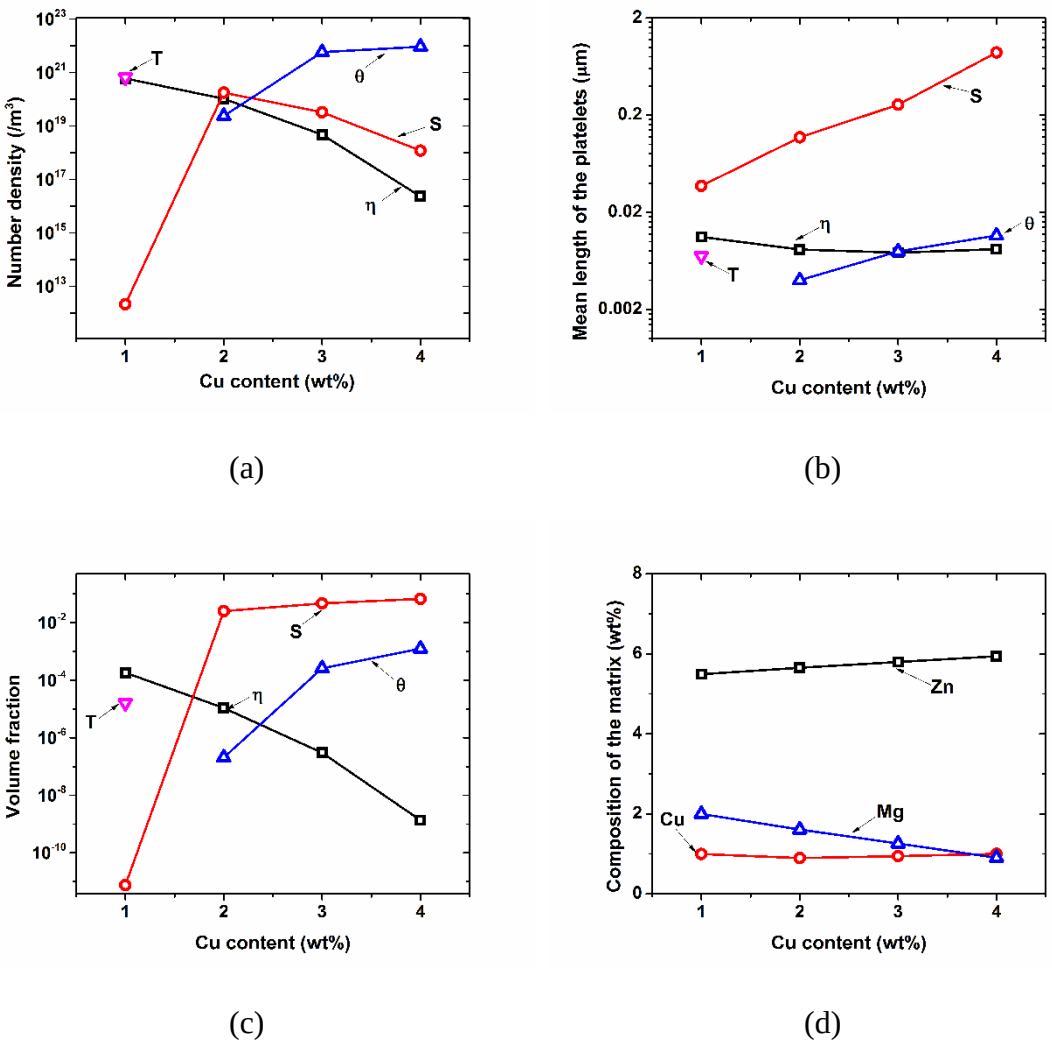

Figure 6.9: Effect of Cu content on (a) number density (b) Mean length of the platelets (c) volume fraction for different precipitated phases and (d) composition of the matrix.

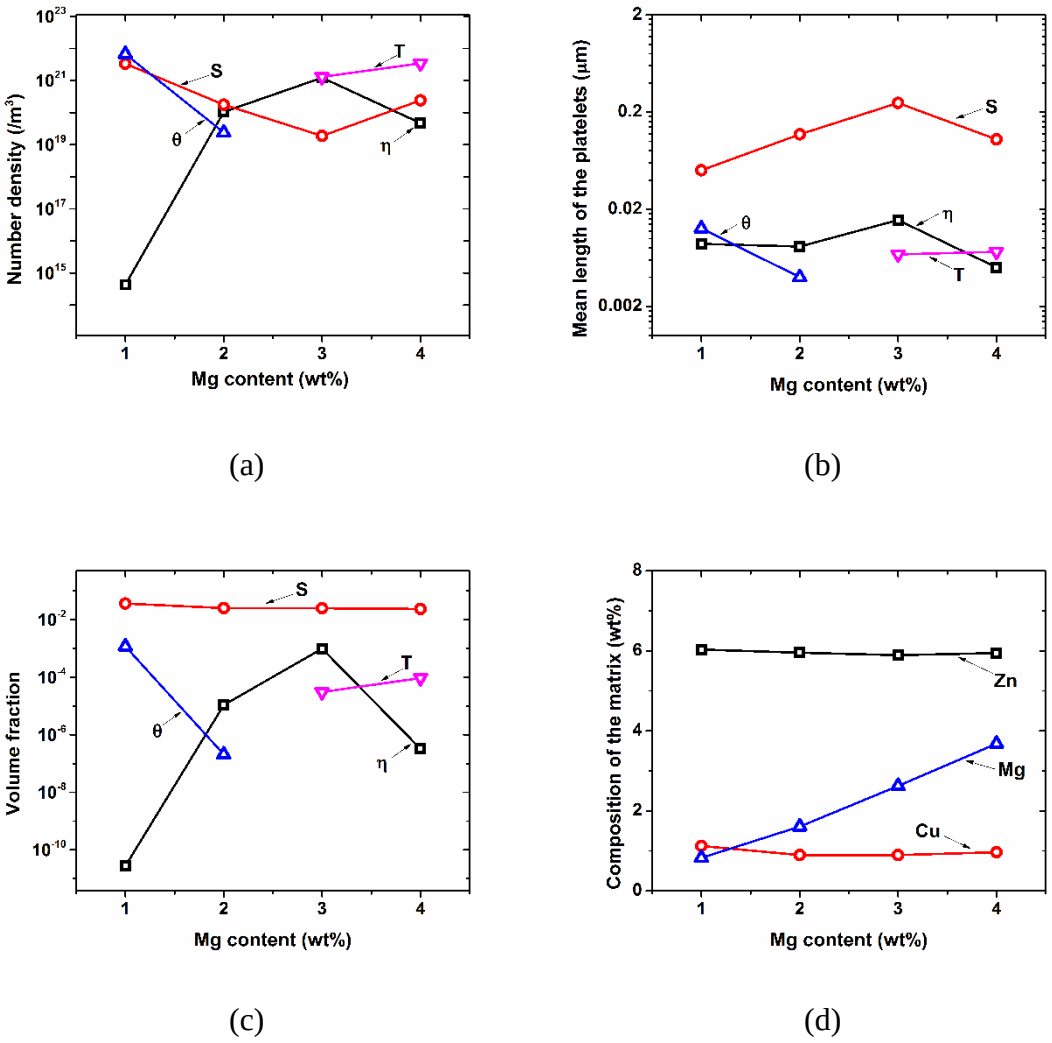

Figure 6.10: Effect of Mg content on (a) number density (b) Mean length of the platelets (c) volume fraction for different precipitated phases and (d) composition of the matrix.

number density of S phase is the lowest. The S phase volume fractions are also high. At high Mg contents, the undesirable low melting T phase appears which is deleterious during extrusion. Also, the flow stress for extrusion increases tremendously due to increase in Mg content which is undesirable. At lowest Mg contents, the S phase number densities are higher. Therefore, a composition of ~2% Mg is desirable for a microstructure with fewer S and η phase precipitates with no T phase.

6.5 Conclusion

A study of precipitation during post-homogenization cooling of 7XXX alloys is done. The initial numerical results for a furnace cooled sample are validated against experiments. The effect of cooling rates and compositions on the precipitation response are evaluated. A very high cooling rate of > 500°C/hr can lead to precipitates <0.6μm in size and lower volume fractions of all phases. A cooling rate of >10°C/s (36000°C/hr) would keep the S phase to minimum which is desirable after solution heat treatment. This is however, difficult to attain for thick sections. At high cooling rates, the precipitated phases are also fine in size so as to dissolve during pre-heat before extrusion. The composition range of 6-8% Zn, 1-1.5%Cu and ~2% Mg is found to reduce the amount of precipitated coarse S phase leading to easily extrudable microstructures with good age hardenability. The CCC and TTT curves for AA7050 have also been predicted by the numerical model.

CHAPTER 7. RADIAL VARIATION OF MICROSTRUCTURE IN A DIRECT CHILL CAST BILLET ON HOMOGENIZATION

7.1 Introduction

The work described in previous chapters is a part of the larger scale integrated study, from casting to evaluating the performance of aluminum extrusions after heat treatment and deformation. The various processes studied are casting, homogenization, and deformation. One process affects the ones downstream, here making the study complex and involving a wide range of length and time scales. There is a complex interplay of processing, microstructure and properties which has to be understood. This is what forms the basis for "Integrated Computational Materials Engineering" (ICME).

"Through process modeling" is not a new concept and has increasingly being used in different fields. Talking of metal processing, several researchers have attempted it in the past. Solidification and homogenization are two very closely related processes and have been done by many researchers. Early studies by Brooks et al.[111] involved evolution of the microsegregation during casting and homogenization of stainless steel welds. It essentially involved solving the mass diffusion equations in a cylindrical domain with a given temperature history with movement of the solid-liquid interface boundary based on phase equilibria equations. The DICTRA™ software, which is able to predict one dimensional diffusion induced phase transformations, has increasingly been used to predict solidification and homogenization microstructures in various alloy systems.

Lippard et al.[112] and Samaras and Haidemenopoulos[39] used DICTRA™ to predict microsegregation and phase fraction evolutions during casting and homogenization of AerMet100 steel and AA6061, respectively. The Pseudo-Front-Tracking method[113] was used by Gandin and Jacot[4] to model solidification and homogenization in AA3003 alloy which was coupled with a precipitation model to predict width of the precipitate-free zones. Warnken et al.[35] used phase-field methodology to study evolution of as-cast microstructure and homogenization in nickel-based alloys.

Some of the larger scale through process modelling studies include works by Neumann et al.[114] and Tin et al.[115] who modeled processing of aluminum sheets and Ni-based superalloy discs, respectively. Neumann et al.[114] modelled casting, homogenization and forming of the Al sheets, where the model in each step produced results which, along with some experimental results, were fed to the next model to create a through process model. For instance, the casting model predicted grain size and microsegregation which, along with the experimentally measured grain size distribution, was fed into the homogenization model. Tin et al.[115] described an integrated model to predict grain structure and defects during various processing stages of a gas turbine disc of INCONEL alloy 718. The process-stream that was studied were Vacuum Arc Remelting (VAR), homogenization, cogging, forging, and heat treatment.

The current study combines the numerical study of the first two processing stages of aluminum extrusions, namely casting and homogenization. These processes are studied for a DC-cast cylindrical billet of AA7050. The DC-casting solidification model in the continuum scale developed by Fezi et al.[22] feeds the radial microstructural and composition information to the meso-scale homogenization and precipitation models developed in this

work to determine the radial variation of microstructure after homogenization and cooling of the billet under industrial conditions. While the solidification model directly predicts the macrosegregation, giving the radial variation of compositions in the billet, the Secondary Dendrite Arms Spacing (SDAS) is indirectly estimated based on the predicted solidification times. This microstructural information helps us predict the microsegregation and volume fraction of the interdendritic phases from Thermo-Calc^{TM}, which can be used

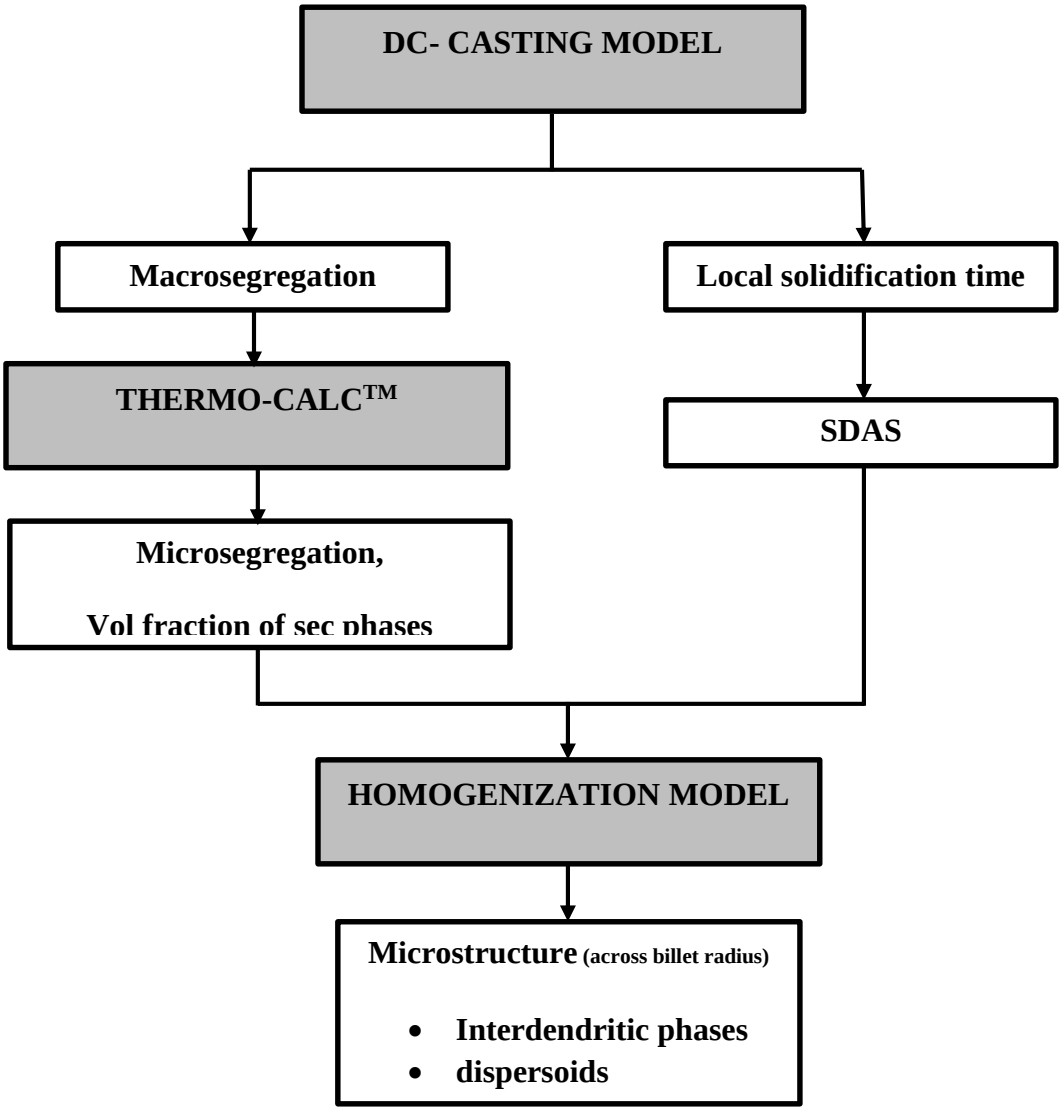

Figure 7.1: Schematic showing the inputs and outputs of the numerical models involved.

to study the microstructural evolution during homogenization and cooling. The flow of the simulations is illustrated in Figure 7.1.

The radial variation of the as-cast microstructure in a cylindrical billet causes a variation in microstructural evolution during homogenization. A radial variation of homogenization temperature history during industrial processing conditions is also considered. A homogenization schedule right for the entire cross section of the billet, without causing remelting of the secondary phases has been proposed.

7.2 Domain Description

The heat transfer in a cylindrical billet under industrial homogenization conditions is modeled. The domain is axisymmetric with radius of 0.35m and the boundary conditions shown in Figure 7.2. The conduction of heat in the billet is modeled through the heat conduction equation in cylindrical coordinates as:

$$\frac{1}{\alpha}\frac{\partial T}{\partial t} = \frac{1}{r}\frac{\partial}{\partial r}\left(r\frac{\partial T}{\partial r}\right) \tag{7.1}$$

where $\alpha = k_c/\rho c_p$. A symmetry conditions is applied at the centerline.

$$\frac{\partial T}{\partial r} = 0 \; at \; r = 0 \tag{7.2}$$

The convective and radiation heat losses at the boundary are considered at billet surface as

$$-\frac{\partial T}{\partial r} = \frac{h}{k_c}\left(T_{R_0} - T_\infty\right) + \varepsilon\sigma\left(T_{R_0}^4 - T_\infty^4\right) \; at \; r = R_0 \tag{7.3}$$

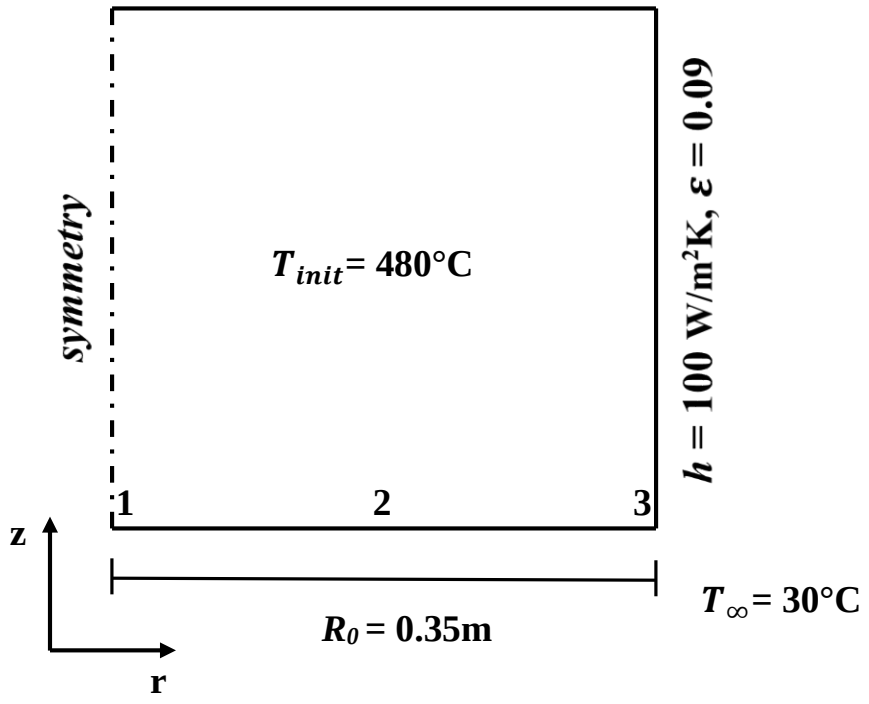

Figure 7.2: Schematic showing the axisymmetric domain and the boundary conditions during industrial cooling of the billet. The positions were microstructures are compared are numbered. The initial temperature is ambient temperature at the beginning of the heating cycle.

Table 7.1: Values of the heat transfer parameters used.

Parameters	Values[116]
α	6.24×10^{-5} m^2/s
k_c	153 W/Mk
h	10 W/m^{2}K (heating)
	100 W/m^{2}K (cooling by forced air)
ε	0.09
σ	5.67×10^{-8} W/m^{2}K^4

Eqn. 7.1 is discretized using implicit finite difference scheme and solved using TDMA[47]. The radial control volume size and time step are Δr=3.5mm and Δt=5s. The values of the various parameters used in the study are listed in Table 7.1. The heat transfer coefficients are the estimated values for air with free convection and air with forced convection during heating and cooling the billet, respectively[117] which is the case during industrial processing conditions. The microstructure at r=0, r=R/2 and r=R after (i) casting, (ii) homogenization, and (iii) post-homogenization cooling are compared in the study.

The temperature profile at the three positions during the proposed homogenization schedule for AA7050 (CHAPTER 4) are compared in Figure 7.3. The temperatures at the 3 positions (Figure 7.2) during heating, holding, and cooling does not vary much for a billet of radius 0.35m. The Biot number, $Bi(=hr/k_c)$ indicates the dominant heat transfer mode, is 0.023 and 0.23 during heating and cooling respectively. $Bi << 1$ indicates heat conduction in the billet offers little resistance to heat transfer and the temperature difference in the body is small compared to the external temperature difference as seen in the results. However, it would have made a difference for a larger sized billet.

7.3 Radial Variation in Microstructure

7.3.1 Initial As-cast Microstructure

The initial as-cast microstructure was based on the predictions by the DC-Cast solidification model for a AA7050 alloy of nominal composition Al-6.2Zn-2.3Cu-2.25Mg-0.115Zr. The mixture composition and local solidification time (LST) were taken at three different radial locations at an axial height of 1.5m from a billet of height 3m. Figure 7.4 shows the mixture composition for Zn, Cu, and Mg, the LST, and the calculated secondary dendrite arm spacing for the surface, mid-radius, and centerline. The LST was calculated

based on when the control volume started and finished solidification and does not take into consideration the movement of solid particles. To take account of solid motion, the LST is assumed to be within 10% of the value predicted by the model. The relationship between

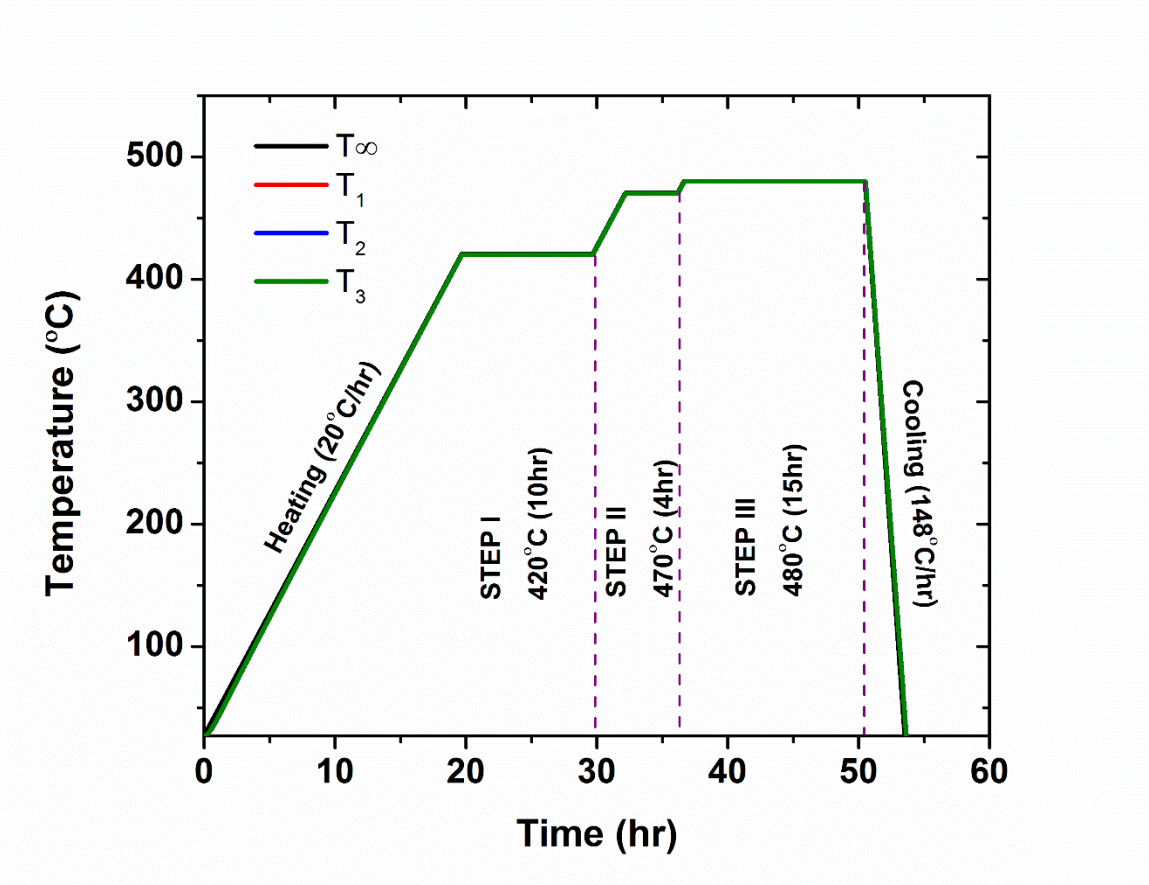

Figure 7.3: The homogenization heating, holding, and cooling cycle chosen in the study showing little variation in temperatures at the 3 positions studied.

LST and SDAS was taken from Dantzig and Rappaz[64], which is valid for Al alloys where 0.1 s < LST < 107 s.

$$\lambda_2 = K t_f^{1/3} \tag{6.4}$$

where, $K = 10^{-5} m/s^{1/3}$. For convection controlled growth the constant in the above expression is closer to 10^{-9} and the exponent for t_f is closer to ½.

Figure 7.4(a) shows the composition of the billet at the 3 positions studied: centerline, mid-radius and surface of the billet. Positive macrosegregation is at mid-radius and surface of the billet. Not much macrosegegation is observed for Zr which is present in trace amounts. Figure 7.4(a) shows the predicted LST and calculated SDAS at the three positions. The solidification time at the surface of the billet is low compared to that at the centerline due to heat transfer which is fast at the surface leading to smaller SDAS.

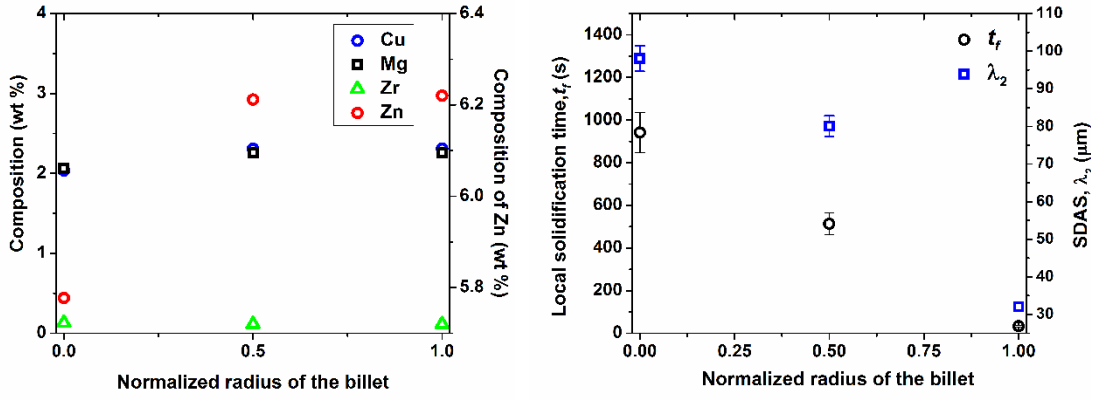

(a) (b)

Figure 7.4: The predicted (a) compositions and (b) LST and SDAS across the radius of the billet.

The predicted compositions and SDAS lengths are used to estimate the as-cast microstructures in the meso-scale for input to the homogenization model. Figure 7.5 (a) shows the as-cast secondary phase fractions as predicted by Thermo-Calc™ corresponding to compositions shown in Figure 7.4(a). The precipitation of Al_3Zr, S (Al_2CuMg), V

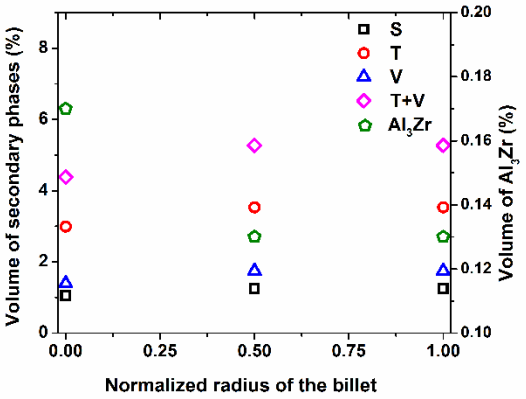

(a)

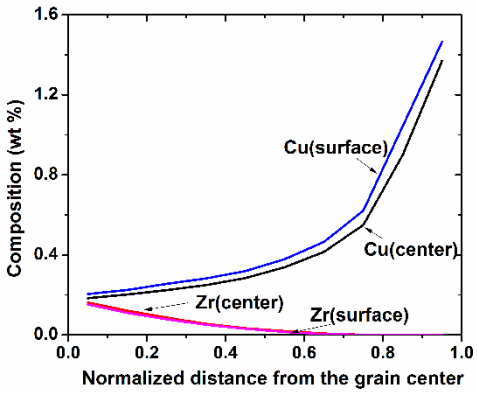

(b)

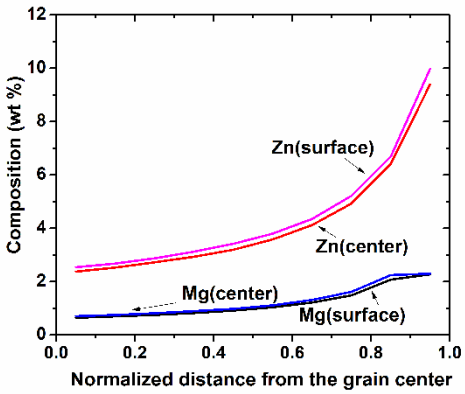

(c)

Figure 7.5: (a) Predicted as-cast volume fractions of secondary phases at different radial positions in the billet; The microsegregation across the grains for (b) Cu and Zr and (c) Zn and Mg.

(solution of Mg_2Zn_{11} and $Al_5Cu_6Mg_2$) and T($Al_2Mg_3Zn_3$) phases are predicted by Thermo-Calc™. As the compositions and temperatures of the mid-radius and surface positions are the same, the volume fraction of the secondary phases are the same. The secondary phases in general are more at the surface which has a higher composition. However, the primary Al_3Zr is higher at the centerline due to higher Zr composition at the centerline which follows a macrosegregartion pattern reverse of other elements.

The predicted compositions are also used in Figure 7.5(b) and (c) to show the microsegregation predicted by Thermo-Calc™ at the centerline and surface of the billet respectively. The amount of Zn, Cu and Mg is higher at the mid-radius and surface positions, leading to higher amounts of these elements across the grain, while Zr is higher at the centerline.

The initial microstructure for the homogenization model at each position is represented by the 1D half-grain domain described in Section 4.2 of CHAPTER 4 with the predicted microsegregation of elements and interdendritic phases in the interdendritic 1st cell. The T and V are taken as a single phase and they convert to the S phase.

7.3.2 Homogenized Microstructure

Microstructure changes at the grain boundaries and also across the grain during homogenization. The transformation and dissolution of the T, V and S phases occurs at the grain boundaries while nano-sized coherent metastable Al_3Zr are precipitated across the grain. Due to different compositions across the radius of the billet which leads to a difference in the as-cast interdendritic phase fractions, there is a variation in the transformation and dissolution kinetics as shown in Figure 7.6. The three homogenization

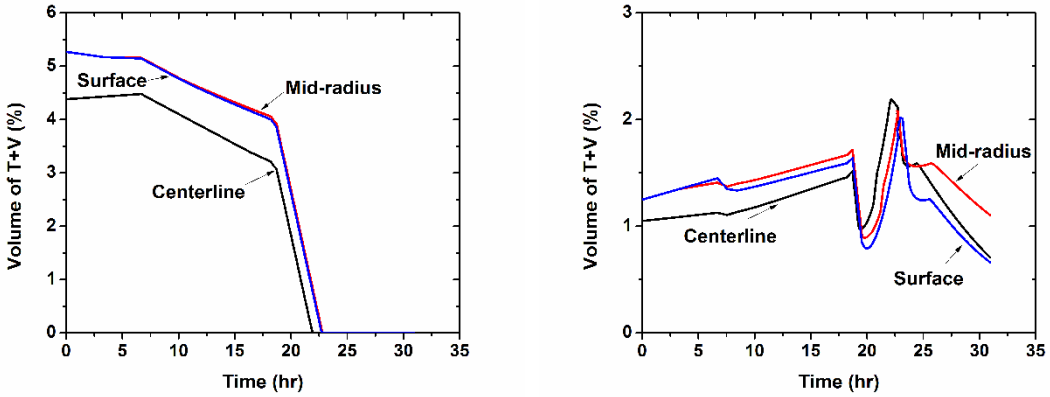

(a)

(b)

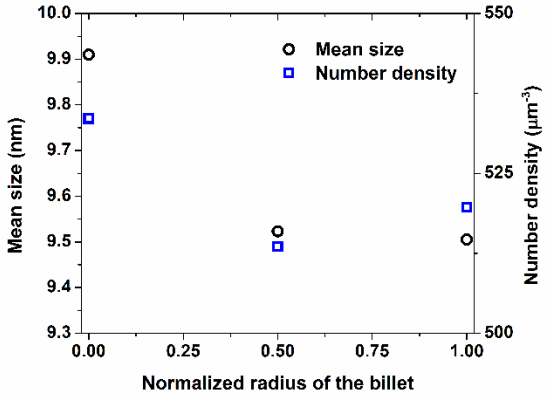

(c)

Figure 7.6: (a) Evolution of the T+V phases; (b) S phase during homogenization; (c) The number density and mean radii of the dispersoids across the radii of the billet after Step II of homogenization.

steps involving 10 hours at 420°C to precipitate dispersoids followed by a second step at 470°C to dissolve T+V and a third at 480°C to minimize S is provided.

During step I, the T+V transform to S. After step I, the amount of T+V and S at the centerline is less than that at the mid-radius and surface positions because of the lower as-cast volume fraction of T+V. During step II, the T+V completely dissolve at the centerline in 3.5 hrs while they do so for the surface and mid-radius positions in 4 hrs as seen in Figure 7.6(a). If we move on to the next step without allowing for complete dissolution of T+V across the entire cross section of the billet, these phase might melt. To ensure the T+V phases do not melt, we need to move on to the next step after 4 hours. Redissolution of some of the precipitated S phase is observed ('reversion') during heating from 420°C to 470°C and from 470°C to 480°C as seen in Figure 7.6(b). Step III involves dissolution of the S phase in which the billet has to be heated for more than 10 hours.

Dispersoids of Al_3Zr precipitate in the grains across the cross section of the billet. The centerline is Zn, Cu and Mg lean and Zr rich compared to the mid radius and the surface. Solute lean centerline has more primary Al_3Zr as seen in Figure 7.5(a) still leaving more Zr during microsegregation as seen in Figure 7.5(c). As seen in Figure 7.6(c), the number densities and mean radii of the dispersoids are both higher at the centerline than at the surface and mid-radius positions due to more nucleation and growth due to higher supersaturation of Zr at the centerline. This leads to higher probability of recrystallization at the periphery than at the center of the billet. This is also observed in industrial extrusions, where peripheral coarse grained microstructures[118] is a major problem.

7.3.3 Post-homogenization Cooled Microstructure

Industrial practice of cooling the billet involves forcing air over its surface after the furnace is switched off. As seen in Figure 7.3, this practice causes cooling at a rate of approximately 148°C/hr at all the three radial positions. The precipitation model is used to simulate the microstructural evolution during post-homogenization cooling. The precipitation of S (Al_2CuMg), η ($MgZn_2$), T ($Al_2Mg_3Zn_3$) and Θ(Al_2Cu), in the decreasing order of temperature, is predicted by the model at all the radial positions.

The number density of the η and T phases are more towards the surface than at the center while the undesirable S phase is more at the centerline, due to higher Zn at the mid-radius and surface positions as seen in Figure 7.7(a). The mean lengths of these platelets are longer and volume fractions are higher at the surface as seen in Figure 7.7(b) and (c) due to higher solute available for growth. As seen in Figure 7.7(d) the size of the S platelets at the surface exceeds 0.6μm and may not dissolve during pre-heat and may cause melting at the surface which may affect the surface finish[7]. Also larger precipitates at the surface may lead to particle stimulated nucleation of recrystallized grains[15] leading to inhomogeneous mechanical properties across the cross section of the billet. The solute remaining in the matrix is higher at the surface leading to more extrusion pressure required for extrusion[9]. The precipitation during cooling, in general produces inhomogeneous precipitation leading to inhomogeneous mechanical properties across the cross section of the billet.

7.4 Process Recommendations

Based on the study, a billet of radius 0.35m needs to be homogenized for 10 hrs at 420 °C to precipitate dispersoids, 4 hrs at 470°C to dissolve T+V and more than 10 hrs at

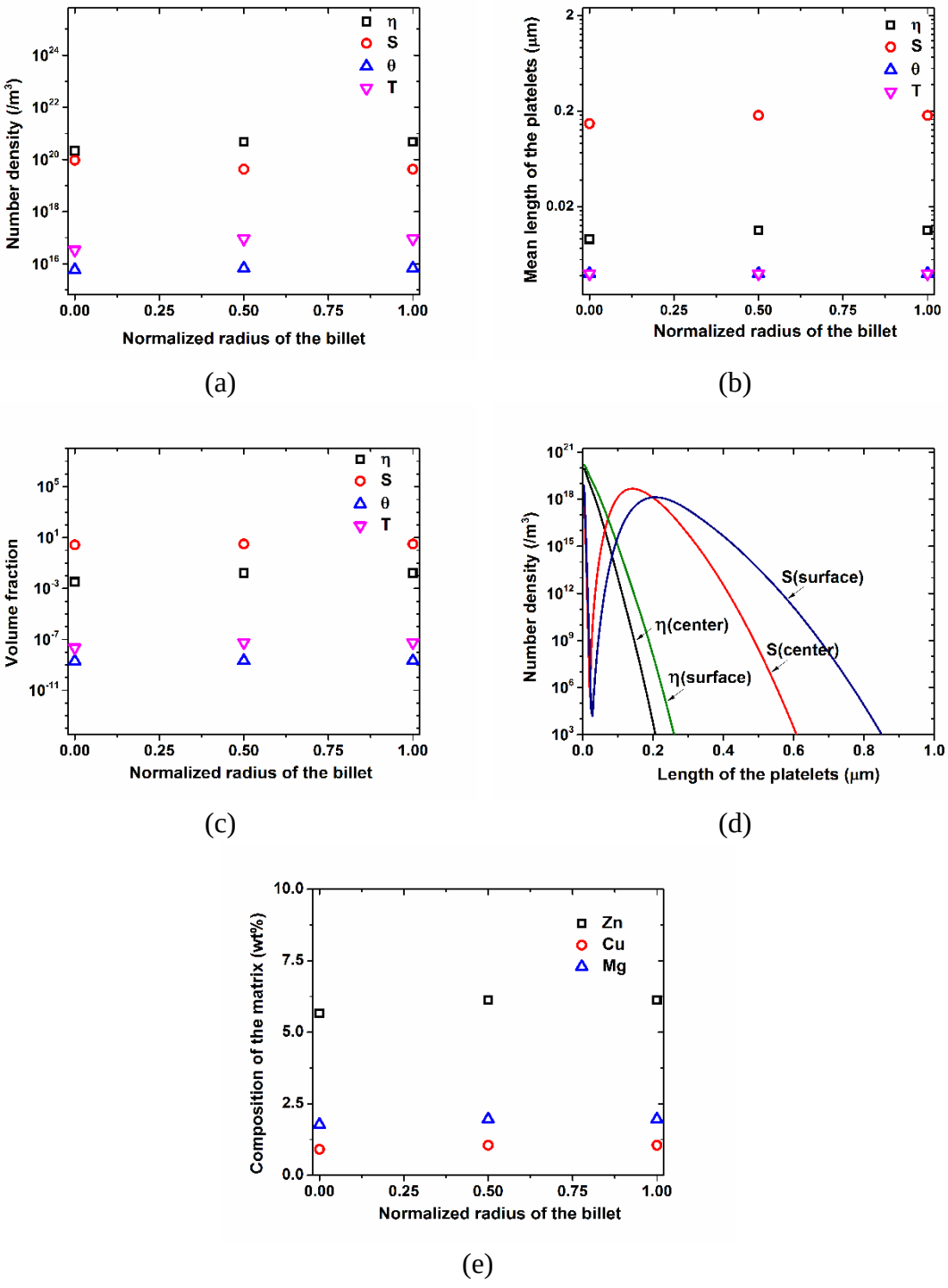

Figure 7.7: The radial variation of (a) number density, (b) mean length of the platelets, (c) volume fraction, (d) size distribution of the phases precipitated during cooling under industrial conditions and (e) radial variation of the composition of the matrix.

480°C to minimize S phase. Sampling at the mid-radius and surface is necessary to determine a proper homogenization schedule as they have a higher composition leading to higher volume fractions of secondary interdendritic phases which take longer to dissolve during step II. Increasing the temperature to 480°C before T dissolves in the entire cross-section may cause melting at the surface and mid-radius causing pores degrading the mechanical properties of the billet.

The Zr macrosegregation in the billet causes higher Zr at the centerline position leading to higher Al_3Zr dispersoid number density compared to the surface making the surface more prone to recrystallization. Addition of a trace element with a macrosegregation profile reverse of that of Zr would solve the problem both at the macro and the micro scale. Addition of Scandium, which has a partition coefficient less than 1 (whereas $k_{Zr}>1$) is a viable solution to the problem leading to macrosegregation and microsegregation patterns reverse of Zr[119]. A k_{Sc} <1 would lead to segregation reverse of Zr and precipitate L_{12} Al_3Sc and $Al_3(Sc,Zr)$ in regions lean in Zr. The $Al_3(Sc,Zr)$ dispersoids are nano-sized and coherent and more efficient than Al_3Zr in increasing the strength.[119] Thus, addition of Sc may not only lead to uniform mechanical properties across the cross section of the billet, but may also reduce dispersoid free zones by precipitating $Al_3(Sc,Zr)$ type precipitates close to the grain boundary. Sc in the range of 0.18-0.2% can be added to Zr (0.1-0.2%) containing 7XXX alloys.

Precipitation during cooling under industrial conditions, produces precipitates more in number and larger in size (>6 μm) at the surface than at the centerline position. The larger precipitates may induce particle stimulated nucleation of the recrystallization which can be inhibited by having more dispersoids at these positions. This is possible by having

Sc in the alloy as described above. The particles may also not dissolve affecting the surface finish for which a cooling rate higher than the general industrial practice is needed.

7.5 Conclusion

The radial variation of microstructure during DC-casting and homogenization of a cylindrical billet of radius 0.35m has been studied. The DC casting model by Fezi et al.[22] and homogenization model from the current work have been used to characterize the radial variation of microstructure. Macrosegregation causes difference in compositions across the cross section of the billet leading to higher compositions and interdendritic phases at the mid-radius and surface positions. 10 hrs at 420°C, 4 hrs at 470°C and more than 10hrs at 480°C leads to homogenization across the entire billet without remelting any of the interdendritic phases when taken to higher temperatures. This schedule matches the scheduled proposed for this alloy in CHAPTER 4. The lower Zr content at the surface leading to lower number densities of Al_3Zr dispersoids, so these regions are more prone to recrystallization. Addition of Sc in the range of 0.18-0.2%, might lead to more uniform microstructure and mechanical properties across the grains and also across the cross section of the billet. Post-homogenization cooling under industrial conditions leads to larger precipitates at the surface which may cause particle stimulated nucleation of recrystallization or may even remain undissolved during preheat causing melting. Using higher cooling rates can reduce the size of the precipitates as discussed in CHAPTER 5. Higher cooling rates are only possible for smaller sections.

CHAPTER 8. CONCLUSIONS AND RECOMMENDATIONS FOR FUTURE WORK

8.1 Conclusions

Numerical models have been developed to study the microstructural evolution at the SDAS and dispersoid length scales during homogenization and post-homogenization quenching of Al-Si-Mg-Fe-Mn (6XXX) and Al-Zn-Cu-Mg-Zr (7XXX) alloys. The models are able to predict microstructures which match experiments well. The effect of temperature, composition, cooling rates and initial microstructural features are studied. Recommendations for improvement of the homogenization schedule for improved extrudability and age-hardenability are suggested. The models developed have been applied to study the radial distribution of microstructure to devise a homogenization schedule for a DC-cast cylindrical billet of radius 0.35 m.

In Al-Si-Mg-Fe-Mn alloys, two models which simulate microstructural evolution at the SDAS and dispersoid length scales are loosely coupled with each other. The needle-like β-AlFeSi in the as-cast microstructure transform into globular α-Al(FeMn)Si during homogenization, while Mg_2Si dispersoids precipitate during post-homogenization cooling. These phase transformations are diffusion controlled processes, transfer of solute across the grains being the slowest step during phase transformation. While Fe and Mn composition differences between the matrix and phase interface drive the initial stage of

the homogenization phase transformation, only Fe composition differences influence the later stage. The Mg_2Si precipitation during quenching is driven by Mg supersaturation in the matrix.

Homogenization at a temperature of 580°C for 8 hrs and cooling at 250°C/hr are suggested for Al-0.83Si-0.7Mg-0.27Fe-0.18Mn alloy. For further improvement, this composition can be modified to $C^{Fe} < 0.17$, $C^{Mn} > 0.2$, and C^{Si} between 0.6 and 0.8, producing a microstructure with no β-AlFeSi needles after homogenization for 8 hrs at 580°C. The composition is still within the specification for 6XXX alloys. On the other hand, 0.5-0.7% Mg can produce Mg_2Si dispersoids which are <1 μm, with only a slight effect on extrusion flow stress. Finally, homogenization time can also be decreased by refining the as-cast structure by higher solidification rates and the use of grain refiners. Higher solidification rates can be achieved by "Fusible Metal Mold"[120] technique, in which a low melting metal is added on the surface of the mold which melts and fills in the air gap between the mold and the casting.

In 7XXX series alloys, a model of coupled phase transformations at two different length scales during homogenization of Al-Zn-Cu-Mg-Zr alloys has been developed. A CA-FV based model which simulates elemental diffusion in a grain and microstructural evolution of the interdendritic η and S phases has been linked to a PSD-based model which simulates precipitation of Al_3Zr dispersoids across the grain, providing a comprehensive picture of time evolution of microstructure. The sluggish nature of the η to S phase transformation is attributed to interface-controlled kinetics, where transfer of Cu atoms at the interface is the slowest step in phase transformation. This is included in the numerical model. During homogenization, η transforms to S phase after which S phase dissolves to

reach the equilibrium volume fraction. While this S phase dissolution occurs, the Al_3Zr dispersoids precipitate and grow throughout the grain, although they are mostly found near the grain center which has the highest Zr concentration in the as-cast microstructure.

Based on the sequence and rates of transformations, a three-stage homogenization schedule is suggested for this alloy. Homogenization at 420°C for 10 rs, followed by 470°C for 4 hrs and 480°C for 15 hrs, is seen to produce a microstructure consisting of uniform nanosized dispersoids with maximum pinning pressure and minimum secondary phases.

The overall composition affects the volume fraction of secondary particles and microsegregation during solidification, and this has a profound effect on the microstructural evolution during homogenization and subsequent processing. Higher Zn, Cu and Mg contents lead to higher amounts of interdendritic T, V and S phase particles and hence require more time to homogenize. Higher alloying content also leads to increased 'quench sensitivity' which makes it difficult to subdue precipitation even at high cooling rates. Higher alloy content also leads to decreased solid solubility of Zr, leading to higher driving force for nucleation of dispersoids. This is however, possible only when the cooling rate during solidification is fast enough to prevent primary Al_3Zr from nucleating in the as-cast structure. Those precipitates would be much coarser than those formed during homogenization with incoherent interface and would decrease the amount of Zr available for precipitation of dispersoids which is undesirable. For solidification under normal conditions, higher alloying content leads to lower number densities for dispersoids. Based on the present study an improved composition range of 6-8%Zn, 1-2%Cu, 1-2%Mg and 0.1-0.15%Zr has been suggested. The suggested composition has lesser Cu than AA7050 and lesser Zn compared to AA7075. Cu is added to AA7050 to increase corrosion

resistance and age hardenability whereas Zn leads to increase in strength in AA7075. The suggestions here are solely based on ease of homogenization and extrusion. Other factors have not been taken into account.

The effect of cooling rates and compositions on the precipitation response are evaluated. A very high cooling rate of >500°C /hr can lead to minimum precipitation with precipitates <0.6 μm which can easily dissolve during preheat. Cooling at >10°C/s (36000°C/hr) can lead to even lower precipitation which is desired after solution treatment for improved age-hardenability. The composition range of 6-8% Zn, 1-1.5%Cu and ~2% Mg is found to reduce the amount of precipitated coarse S phase leading to easily extrudable microstructures with good age hardenability. The CCC and TTT curves for AA7050 have also been predicted by the numerical model.

The radial variation of microstructure during DC-casting and homogenization of a cylindrical billet of radius 0.35 m has been studied. The DC casting model by Fezi et al.[22] and homogenization model from the current work have been used to characterize the radial variation of microstructure. Macrosegregation causes difference in compositions across the cross section of the billet leading to higher compositions and interdendritic phases at the mid-radius and surface positions. A heat treatment of 10 hrs at 420°C, 4 hrs at 470°C and more than 10 hrs at 480°C leads to homogenization across the entire billet without remelting any of the interdendritic phases. This matches the homogenization schedule for AA7050 proposed in CHAPTER 4. Due to lower Zr content at the surface leading to lower number densities of Al_3Zr dispersoids, these regions are more prone to recrystallization. Addition of Sc might lead to more uniform microstructure and mechanical properties across the grain and across the cross section of the billet. Industrial cooling practice leads

to precipitation of the undesirable phases larger than 0.6 μm at the surface which might not dissolve and affect the surface finish of the extrudate. Quenching at higher cooling rates is therefore, desired.

8.2 Future Work

This work studies the homogenization heat treatment in Al-Si-Mg-Fe-Mn and Al-Zn-Cu-Mg-Zr alloys in detail. The phase transformation kinetics is predicted and process recommendations are made. There are, however, other related areas where additional work must be done. The predictive ability of the numerical model developed can be increased and extended to other processes.

8.2.1 Experimental Verification of Interface Reaction-controlled Phase Transformations

The η to S phase transformation has been discussed in CHAPTER 4 and is predicted to be interface reaction rate-controlled, unlike the other important reactions which are diffusion controlled. The transfer of Cu atoms across the interface is slower than its diffusion across the grain. This aspect of the phase transformation can to be investigated further.

One way of finding whether a transformation is interface reaction controlled is by finding the Avrami exponent, *n* as in eqn. 3.1. The values of *n* in the range of 3 or above indicates an interface reaction rate control[70]. However, the transformation of η to S is accompanied with other transformations of dissolution of η and S, making it difficult to find out experimentally.

Another method would be to monitor the interface mobility with time. For interface reaction rate control the interface velocity should be constant[121] leading to a linear dependence of transformed volume fraction on time. This method, although possible, has

to be conducted in very controlled environments so that the measurements are not affected by other transformations occurring.

An experimental verification of the kinetics would involve observation of the η/S interface. The ratio of the ledge lengths to the ledge heights seen on the interfaces are indicative of the kinetic rate controlling step for plate like precipitates[122]. Larger ledge length to height ratios indicate inhibition of interface movement related to interface reaction rate control. Numerical study by Wang et al.[123] propose interface reaction rate control for ledge length to height ratio greater than 128 is no longer diffusion controlled transformation. Such an experimental verification through Transmission Electron Microscopy (TEM) would be advantages to better understand the kinetics.

8.2.2 Computationally Efficient 2D Microstructural Model

CHAPTER 2 describes the 2D CA-FV based diffusion-based numerical model used to study the microstructural evolution in Al-Si-Mg-Fe-Mn alloys during homogenization. The study is later discussed in detail in CHAPTER 3. This growth algorithm from this model has been used by the numerical model to study microstructure in Al-Zn-Cu-Mg-Zr alloys. However, the Al-Zn-Cu-Mg-Zr alloy model is 1D and couples the precipitation model for modeling the simulataneous precipitation of dispersoids. The interface reaction rate controlled growth algorithm in this model has been developed for a 1D domain and can be extended to 2D.

The 2D extension of the 1D model for Al-Zn-Cu-Mg-Zr alloys requires piecewise linear "interface reconstruction"[52,124,125]. As the normal of the interface is already calculated for finding the curvature, interface reconstruction should be easy and straight-forward. The normal can be used to create a linear interface perpendicular to it depending

on the precipitate volume fraction of the cell. The length of this interface and the calculated velocity of the interface can be used to calculate the change in volume fraction perpendicular to the interface as shown in Figure 8.1. The boundary AB is the reconstructed interface perpendicular to the normal which moves by $v\Delta t$ perpendicular to the interface in time period Δt. If CD is the position of the new interface, the area ABDC gives the volume fraction increase in the precipitate phase. Geometry can assist in such calculations.

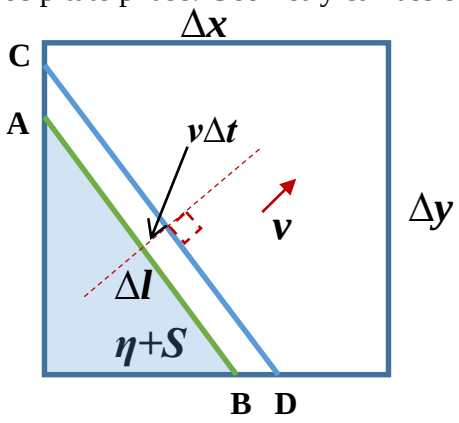

Figure 8.1: Geometry of the interface cell showing the reconstructed interface and its movement perpendicular to the normal

In the current study the dispersoid precipitation model has been included in each cell of the 1D domain. Doing so for the 2D model can make it computationally expensive. However, this may be useful as it helps us get a reasonable estimation of the width of the dispersoid free zones close to the grain boundaries. A computationally efficient precipitation model by not having a fixed number of control volumes and creating the control volumes on the go with nucleation in each time step might make it computationally less expensive. The control volume would have to be created on nucleation of a set of dispersoids and destroyed in the next time step when it grows. This would keep the number of control volume limited to make the calculations for limited decreasing the computation time.

8.2.3 Modeling Thermo-Calc™ based Solidification Microstructure

Cellular Automata have been used by researchers[45,126,127] in the past for predicting solidification microstructures. However, most of these studies were on binary alloys involving only a liquid and one solid phase. Also, the thermodynamic data was used from previous literature through partition coefficients and empirical relationships. The current model predicts microstructure during phase transformations involving 3 phases for a 4 component alloy system. The model extracts thermodynamic data from Thermo-Calc™ through TQ-Interface. This model can be modified to predict Thermo-Calc based solidification microstructure in a multicomponent alloy.

As the model can handle 3 phases, the nucleation of the primary α matrix can easily be modelled with the third phase being the eutectic mixture. The curvature model can be used to calculate undercooling which leads to the dendritic morphology. The major modification would be the thermodynamic model and use of the TQ-Interface based on the alloy being studied. The model can also be extended to more number of alloying elements by modification of the growth algorithm.

8.2.4 Modeling Homogenization during Post-solidification Cooling

Homogenization is a post-solidification heat treatment and can start during the cooling from solidification. Solidification involves cooling from very high temperatures typically 650°C for aluminum alloys. The models developed in this study can be used to study the evolution of microstructure in alloys during post-solidification cooling. The change in microstructure is considerable given that the high temperatures reached and time taken by the casting to cool. This makes a difference in alloys which take comparatively less time to homogenize, such as the 6XXX alloys.

Considering the geometry and dimensions of the casting, the initial microstructure may have a spatial variation which can be modeled as a heat transfer problem similar to CHAPTER 6. While the surface which cools faster may "homogenize" less, the center may remain comparatively more "homogenized". Also, depending on the cooling rate the precipitation response, which depends on the Mg concentrations and cooling rates, would also be different which can be tracked using the precipitation model. The transformation of interdendritic particles, precipitation of spherical and plate-like precipitates can be modeled easily.

8.2.5 Experimental Verification of Composition Effects in 7XXX Alloys

The effect of compositional variations on the evolution of interdendritic and dispersoid phases has been discussed in CHAPTER 5. Some of the results involving dispersoid number density and mean radius and their variation on varying the Zn, Cu and Mg compositions differ from those predicted by numerical model by Robson and Pragnell.[18] The reason behind this discrepancy is the precipitation of DO_{23} Al_3Zr during solidification which reduces the amount of Zr available for precipitation of dispersoids during homogenization which was not considered by Robson and Prangnell[18]. This finding from Thermo-Calc predictions has to be verified experimentally.

The Al_3Zr formed during casting can be studied through microscopic observation of as-cast microstructures of alloys of various compositions. The number densities predicted after homogenization can also be compared to that of experimentally homogenized samples. It should however take into consideration the dispersoids which were formed during casting. The primary Al_3Zr are mostly petal-like as found by Knipling et al.[119] in Al-Sc-Zr alloys.

REFERENCES

REFERENCES

1. Mrówka-Nowotnik G, Sieniawski J, Wierzbińska M. Analysis of intermetallic particles in AlSi1MgMn aluminium alloy. *J Achiev Mater Manuf Eng*. 2007;20:7-8.
2. Deng Y, Yin Z, Cong F. Intermetallic phase evolution of 7050 aluminum alloy during homogenization. *Intermetallics*. 2012;26:114-121. doi:10.1016/j.intermet.2012.03.006.
3. Zajac S, Hutchinson B, Johansson A, Gullman LO. Microstructure control and extrudability of Al–Mg–Si alloys microalloyed with manganese. *Mater Sci Technol*. 1994;10(4):323-333. doi:10.1179/mst.1994.10.4.323.
4. Gandin C-A, Jacot A. Modeling of precipitate-free zone formed upon homogenization in a multi-component alloy. *Acta Mater*. 2007;55(7):2539-2553. doi:10.1016/j.actamat.2006.11.047.
5. Robson JD. Optimizing the homogenization of zirconium containing commercial aluminium alloys using a novel process model. *Mater Sci Eng*. 2002;338:219-229.
6. Lassance D, Schmitz M, Delannay F, Pardoen T. Linking microstructure and high temperature ductility in aluminium alloys AA6xxx. *15th Eur Conf Fract Adv Fract Mech Life Saf Assess*. 2004.
7. Minoda T, Hayakawa H, Yoshida H. A mechanism of pick-up formation on 6063 aluminum alloy extrusions. *Keikinzoku/Journal Japan Inst Light Met*. 1999;49(6):253-257.
8. Milkereit B, Wanderka N, Schick C, Kessler O. Continuous cooling precipitation diagrams of Al–Mg–Si alloys. *Mater Sci Eng A*. 2012;550:87-96. doi:10.1016/j.msea.2012.04.033.

9. McQueen HJ, Spigarelli S, Kassner ME, Evangelista E. *Hot Deformation and Processing of Aluminum Alloys*. CRC Press; 2011.
10. Wang H, Xu J, Kang Y, Tang M, Zhang Z. Study on inhomogeneous characteristics and optimize homogenization treatment parameter for large size DC ingots of Al–Zn–Mg–Cu alloys. *J Alloys Compd*. 2014;585:19-24. doi:10.1016/j.jallcom.2013.09.139.
11. Fan X, Jiang D, Meng Q, Zhang BY, Wang T. Evolution of eutectic structures in Al-Zn-Mg-Cu alloys during heat treatment. *Trans Nonferrous Met Soc China*. 2006:577-581.
12. Jia P, Cao Y, Geng Y, He L, Xiao N, Cui J. Studies on the microstructures and properties in phase transformation of homogenized 7050 alloy. *Mater Sci Eng A*. 2014;612:335-342. doi:10.1016/j.msea.2014.06.027.
13. Lim ST, Eun IS, Nam SW. Control of equilibrium phases (M, T, S) in the modified aluminum alloy 7175 for thick foriging applications. *Mater Trans*. 2003;44(1):181-187.
14. Godard D, Archambault P, Aeby-Gautier E, Lapasset G. Precipitation sequences during quenching of the AA 7010 alloy. In: *Acta Materialia*. Vol 50. ; 2002:2319-2329. doi:10.1016/S1359-6454(02)00063-0.
15. F. J. Humphreys, Hatherly M. *Recrystallization and Related Annealing Phenomena*. Oxford, UK: Pergamon Press; 1996.
16. Wu L-M, Wang W-H, Hsu Y-F, Trong S. Effects of homogenization treatment on recrystallization behavior and dispersoid distribution in an Al–Zn–Mg–Sc–Zr alloy. *J Alloys Compd*. 2008;456(1-2):163-169. doi:10.1016/j.jallcom.2007.02.054.
17. Kuijpers NCW, Vermolen FJ, Vuik K, Zwaag S Van Der. A Model of the β-AlFeSi to α-Al (FeMn) Si Transformation in Al – Mg – Si Alloys. *Mater Trans*. 2003;44(7):1448-1456.
18. Robson J., Prangnell P. Modelling Al3Zr dispersoid precipitation in multicomponent aluminium alloys. *Mater Sci Eng A*. 2003;352(1-2):240-250. doi:10.1016/S0921-5093(02)00894-8.

19. Cavazos JL, Colas R. Quench sensitivity of a heat treatable aluminum alloy. *Mater Sci Eng A*. 2003;363(1-2):171-178. doi:10.1016/S0921-5093(03)00616-6.
20. Allison J, Li M, Wolverton C, Su XM. Virtual aluminum castings: An industrial application of ICME. *JOM*. 2006;58(11):28-35. doi:10.1007/s11837-006-0224-4.
21. Allison J. Integrated computational materials engineering: A perspective on progress and future steps. *JOM*. 2011;63(4):15-18. doi:10.1007/s11837-011-0053-y.
22. Fezi K, Coleman J, Krane MJM. Macrosegregation during Direct Chill Casting of Aluminum Alloy 7050. In: *Light Metals 2015*. Hoboken, NJ, USA: John Wiley & Sons, Inc.; 2015:871-875. doi:10.1002/9781119093435.ch146.
23. Aaron HB. On the Kinetics of Precipitate Dissolution. *Met Sci J*. 1968;2(1):192-193. doi:10.1179/030634568790443170.
24. Whelan MJ. On the Kinetics of Precipitate Dissolution. *Met Sci*. 1969;3(4):95-97. doi:10.1179/030634568790443170.
25. Tanzilli RA, Heckel RW. Numerical Solutions to the Finite, Diffusion-Controlled, Two-Phase, Moving-Interface Problem (with Planar, Cylindrical, and Spherical Interfaces). *Trans Metall Soc AIME*. 1968;242(November):2313-2321.
26. Aaron HB, Kotler GR. Second phase dissolution. *Metall Trans*. 1971;2(2):393-408. doi:10.1007/BF02663326.
27. Nolfi F V, Shewmon PG, Foster JS. The Dissolution and Growth Kinetics of Spherical Precipitates. 1969;245(July):1427-1433.
28. Tundal UH, Ryum N. Dissolution of particles in binary alloys: part I. computer simulations. *Metall Trans A*. 1992;23(2):433-444. doi:10.1007/BF02801160.
29. Nojiri N, Enomoto M. Diffusion-controlled dissolution of a spherical precipitate in an infinite binary alloy. *Scr Metall Mater*. 1995;32(5):787-791. doi:10.1016/0956-716X(95)91604-N.
30. Enomoto M. Influence of interfacial curvature on the growth and dissolution kinetics of a spherical precipitate. *Scr Mater*. 1997;36(6):625-632. doi:10.1016/S1359-6462(96)00432-0.

31. Sinder M, Pelleg J. On homogenization of a binary alloy after dissolution of planar and spherical precipitates. *Metall Mater Trans A*. 2000;31(June):1525-1530. doi:10.1007/s11661-000-0163-6.

32. Vermolen F, Vuik K, Zwaag S Van Der. A mathematical model for the dissolution kinetics of Mg 2 Si-phases in Al – Mg – Si alloys during homogenisation under industrial conditions. 1998;254:13-32.

33. Dons AL. The Alstruc homogenization model for industrial Al alloys. *J Light Met*. 2001;1:133-149.

34. Das SK, Kang D-H, Jung I-H. Experimental and Diffusion Simulation for the Homogenization of As-cast Mg-Al, Mg-Zn, and Mg-Al-Zn Alloys. *Metall Mater Trans A*. 2014;45(11):5212-5225. doi:10.1007/s11661-014-2443-6.

35. Warnken N, Ma D, Drevermann a., Reed RC, Fries SG, Steinbach I. Phase-field modelling of as-cast microstructure evolution in nickel-based superalloys. *Acta Mater*. 2009;57(19):5862-5875. doi:10.1016/j.actamat.2009.08.013.

36. Böttger B, Carré A, Eiken J. Simulation of microstructure formation in technical aluminum alloys using the multiphase-field method. *Trans Indian …*. 2009;62(October):299-304. http://link.springer.com/article/10.1007/s12666-009-0046-5.

37. Eivani a. R, Ahmed H, Zhou J, Duszczyk J. Evolution of Grain Boundary Phases during the Homogenization of AA7020 Aluminum Alloy. *Metall Mater Trans A*. 2009;40(3):717-728. doi:10.1007/s11661-008-9741-9.

38. Eivani a. R, Ahmed H, Zhou J, Duszczyk J. An experimental and theoretical investigation of the formation of Zr-containing dispersoids in Al–4.5Zn–1Mg aluminum alloy. *Mater Sci Eng A*. 2010;527(9):2418-2430. doi:10.1016/j.msea.2010.01.012.

39. Samaras SN, Haidemenopoulos GN. Modelling of microsegregation and homogenization of 6061 extrudable Al-alloy. *J Mater Process Technol*. 2007;193(1-3):63-73. doi:10.1016/j.jmatprotec.2007.03.126.

40. Haidemenopoulos GN, Kamoutsi H, Zervaki a. D. Simulation of the transformation of iron intermetallics during homogenization of 6xxx series extrudable aluminum alloys. *J Mater Process Technol*. 2012;212(11):2255-2260. doi:10.1016/j.jmatprotec.2012.06.026.
41. Robson J. A new model for prediction of dispersoid precipitation in aluminium alloys containing zirconium and scandium. *Acta Mater*. 2004;52(6):1409-1421. doi:10.1016/j.actamat.2003.11.023.
42. Du Q, Poole WJ, Wells M a., Parson NC. Microstructure evolution during homogenization of Al–Mn–Fe–Si alloys: Modeling and experimental results. *Acta Mater*. 2013;61(13):4961-4973. doi:10.1016/j.actamat.2013.04.050.
43. Wagner R, Kampmann R, Voorhees PW. Homogeneous Second-Phase Precipitation. In: *Phase Transformations in Materials*. Weinheim, FRG: Wiley-VCH Verlag GmbH & Co. KGaA; 2005:309-407. doi:10.1002/352760264X.ch5.
44. Pope SB. Computationally efficient implementation of combustion chemistry using in situ adaptive tabulation. *Combust Theory Model*. 1997;1(1):41-63. doi:10.1088/1364-7830/1/1/006.
45. Krane MJM, Johnson DR, Raghavan S. The development of a cellular automaton-finite volume model for dendritic growth. *Appl Math Model*. 2009;33(5):2234-2247. doi:10.1016/j.apm.2008.06.007.
46. Shao R, Trumble K, Krane M. Effects of geometric constrains on alloy solidification in metal-matrix composites. In: *Modeling of Casting, Welding and Advanced Solidifcation Processes - XII.* ; 2009:495-503.
47. Patankar S. *Numerical Heat Transfer and Fluid Flow*. Taylor & Francis; 1980.
48. Hillert M. Solute drag , solute trapping and diffusional dissipation of Gibbs energy. *Acta Mater*. 1999;47(18):4481-4505.
49. Thévoz P, Desbiolles JL, Rappaz M. Modeling of equiaxed microstructure formation in casting. *Metall Trans A*. 1989;20(2):311-322. doi:10.1007/BF02670257.
50. Swalin RA. *Thermodynamics of Solids*. Wiley; 1972.

51. Cummins SJ, Francois MM, Kothe DB. Estimating curvature from volume fractions. *Comput Struct*. 2005;83(6-7):425-434. doi:10.1016/j.compstruc.2004.08.017.

52. Yanke J, Fezi K, Trice RW, Krane MJM. Simulation of Slag-Skin Formation in Electroslag Remelting Using a Volume-of-Fluid Method. *Numer Heat Transf Part A Appl*. 2015;67(3):268-292. doi:10.1080/10407782.2014.937208.

53. Morillon T. Prediction of secondary phase dissolution during heat treatment of a Ni-Cr-Mo alloy. 2004;(December).

54. Cai M, Robson JD, Lorimer GW, Parson NC. Simulation of the Casting and Homogenization of Two 6xxx Series Alloys. *Mater Sci Forum*. 2002;396-402:209-214. doi:10.4028/www.scientific.net/MSF.396-402.209.

55. Myhr OR, Grong Ø. Modelling of non-isothermal transformations in alloys containing a particle distribution. *Acta Mater*. 2000;48(7):1605-1615. doi:10.1016/S1359-6454(99)00435-8.

56. Liu G, Zhang GJ, Ding XD, Sun J, Chen KH. Modeling the strengthening response to aging process of heat-treatable aluminum alloys containing plate/disc- or rod/needle-shaped precipitates. *Mater Sci Eng A*. 2003;344(1–2):113-124. doi:10.1016/S0921-5093(02)00398-2.

57. Ferrante M, Doherty RD. Influence of interfacial properties on the kinetics of precipitation and precipitate coarsening in aluminium-silver alloys. *Acta Metall*. 1979;27(10):1603-1614. doi:10.1016/0001-6160(79)90043-9.

58. Rougier L, Jacot A, Gandin C-A, et al. Numerical simulation of precipitation in multicomponent Ni-base alloys. *Acta Mater*. 2013;61(17):6396-6405. doi:10.1016/j.actamat.2013.07.018.

59. Sun Y, Johnson DR, Trumble K, Priya P, Krane MJM. Effect of Mg2Si Phase on Extrusion of AA 6005 Aluminum Alloy. *Light Met 2014*. 2014:429-433.

60. Birol Y. The effect of homogenization practice on the microstructure of AA6063 billets. *J Mater Process Technol*. 2004;148(2):250-258. doi:10.1016/j.jmatprotec.2004.01.056.

61. Birol Y. Optimization of homogenization for a low alloyed AlMgSi alloy. *Mater Charact*. 2013;80(Table 1):69-75. doi:10.1016/j.matchar.2013.03.013.

62. Birol Y. Homogenization of en AW 6005A Alloy for Improved Extrudability. *Metall Mater Trans A*. 2013;44(1):504-511. doi:10.1007/s11661-012-1379-y.
63. Kuijpers NCW. Kinetics of the β-AlFeSi to α-Al (FeMn) Si transformation in Al-Mg-Si alloys. 2004.
64. Dantzig J, Rappaz M. *Solidification*. EPFL press; 2009.
65. *Int Alloy Des Chem Compos Limits Wrought Alum Wrought Alum Alloy 2015 Alum Assoc Arlington*.
66. Sha G, O'Reilly K, Cantor B, Worth J, Hamerton R. Growth related metastable phase selection in a 6xxx series wrought Al alloy. *Mater Sci Eng A*. 2001;304-306:612-616. doi:10.1016/S0921-5093(00)01545-8.
67. Mondolfo LF. *Aluminum Alloys: Structure and Properties*. Elsevier; 2013.
68. Avrami M. Kinetics of phase change. III. Granulation, phase change, and microstructure. *J Chem Phys*. 1941;9(2):177-184.
69. Johnson WA, Mehl RF. Reaction kinetics in processes of nucleation and growth. *Trans Aime*. 1939;135(8):396-415.
70. Christian JW. *The Theory of Transformations in Metals and Alloys*. Pergamon Press, Oxford; 1977.
71. Tanihata H, Matsuda K, Ikeno S. High Resolution Transmission Electron Microscope Observation of the Metastable Phase in an Aged Commercial AA6063. *Mater Sci Forum*. 1996;217-222:809-814. doi:10.4028/www.scientific.net/MSF.217-222.809.
72. Skjerpe P. Intermetallic phases formed during DC-casting of an Al−0.25 Wt Pct Fe−0.13 Wt Pct Si alloy. *Metall Trans A*. 1987;18(2):189-200. doi:10.1007/BF02825700.
73. Gorny A, Manickaraj J, Cai Z, Shankar S. Evolution of Fe based intermetallic phases in Al-Si hypoeutectic casting alloys: Influence of the Si and Fe concentrations, and solidification rate. *J Alloys Compd*. 2013;577:103-124. doi:10.1016/j.jallcom.2013.04.139.
74. Bahadur A. Intermetallic phases in Al-Mn alloys. *J Mater Sci*. 1988;23(1):48-54. doi:10.1007/BF01174033.

75. Verma A, Kumar S, Grant PS, O'Reilly K a. Q. Influence of cooling rate on the Fe intermetallic formation in an AA6063 Al alloy. *J Alloys Compd*. 2013;555:274-282. doi:10.1016/j.jallcom.2012.12.077.

76. Hsu C, O'Reilly K A. Q, Cantor B, Hamerton R. Non-equilibrium reactions in 6xxx series Al alloys. *Mater Sci Eng A*. 2001;304-306:119-124. doi:10.1016/S0921-5093(00)01467-2.

77. Meredith MW, Worth J, Hamerton R. Intermetallic Phase Selection during Solidification of Al-Fe-Si(-Mg) Alloys. *Mater Sci Forum*. 2002;396-402:107-112. doi:10.4028/www.scientific.net/MSF.396-402.107.

78. Sha G, O'Reilly K, Cantor B, Hamerton R, Worth J. Effect of Grain Refiner on Intermetallic Phase Formation in Directional Solidification of 6xxx Series Wrought Al Alloys. *Mater Sci Forum*. 2000;331-337:253-258. doi:10.4028/www.scientific.net/MSF.331-337.253.

79. Edwards GA, Stiller K, Dunlop GL, Couper MJ. The precipitation sequence in Al–Mg–Si alloys. *Acta Mater*. 1998;46(11):3893-3904. doi:10.1016/S1359-6454(98)00059-7.

80. Birol Y. Effect of cooling rate on precipitation during homogenization cooling in an excess silicon AlMgSi alloy. *Mater Charact*. 2012;73:37-42. doi:10.1016/j.matchar.2012.07.015.

81. Johannes VI, Jowett CW. Temperature distribution in aluminum extrsuion billets. *Six Int Alum Extrus Technol Semin*. 1996.

82. Asensio-Lozano J, Suarez-Pena B, Voort GF Vander. Effect of processing steps on the mechanical properties and surface appearance of 6063 aluminium extruded products. *Materials (Basel)*. 2014;7(6):4224-4242. doi:10.3390/ma7064224.

83. Williams JC, Starke EA. Progress in structural materials for aerospace systems. *Acta Mater*. 2003;51(19):5775-5799. doi:10.1016/j.actamat.2003.08.023.

84. Hunsicker HY. Developement of Al-Zn-Cu-Mg alloys. *Philos Trans R Soc London*. 1976;282(1307):359-376.

85. Morere B, Shahani R, Maurice C, Driver J. The influence of Al3Zr dispersoids on the recrystallization of hot-deformed AA 7010 alloys. *Metall Mater Trans A*. 2001;32(3):625-632. doi:10.1007/s11661-001-0079-9.

86. Fan X, Jiang D, Meng Q, Zhong L. The microstructural evolution of an Al–Zn–Mg–Cu alloy during homogenization. *Mater Lett*. 2006;60(12):1475-1479. doi:10.1016/j.matlet.2005.11.049.

87. Underwood EE. *Quantitative Stereology*. Addison-Wesley Pub. Co.; 1970. https://books.google.com/books?id=Epg1AAAAIAAJ.

88. Doherty RD, Srolovitz DJ, Rollett AD, Anderson MP. On the volume fraction dependence of particle limited grain growth. *Scr Metall*. 1987;21:675-679. doi:http://dx.doi.org/10.1016/0036-9748(87)90383-8.

89. Robson J. Optimizing the homogenization of zirconium containing commercial aluminium alloys using a novel process model. *Mater Sci Eng A*. 2002;338(1-2):219-229. doi:10.1016/S0921-5093(02)00061-8.

90. Li XM, Starink M. J. The effect of compositional variations on characteristics of coarse intermetallic particles in overaged 7000 aluminium alloys. *Mater Sci Technol*. 2001;17:1324-1328. doi:10.1179/026708301101509449.

91. Li XM, Starink MJ. DSC Study on Phase Transitions and Their Correlation with Properties of Overaged Al-Zn-Mg-Cu Alloys. *J Mater Eng Perform*. 2011;21(June):977-984. doi:10.1007/s11665-011-9973-5.

92. Sharma MM, Ziemian CW, Eden TJ. Processing and Composition Effects on the Fracture Behavior of Spray-Formed 7XXX Series Al Alloys. *J Mater Eng Perform*. 2010;19(9):1344-1351. doi:10.1007/s11665-010-9624-2.

93. Sharma MM. Microstructural and mechanical characterization of various modified 7XXX series spray formed alloys. *Mater Charact*. 2008;59(1):91-99. doi:10.1016/j.matchar.2007.01.013.

94. Salamci E. Mechanical properties of spray cast 7xxx series aluminium alloys. *Turkish J Eng Environ Sci*. 2002;26(4):345-352. http://www.scopus.com/scopus/inward/record.url?eid=2-s2.0-0036309869&partnerID=40&rel=R8.0.0.

95. Robson J., Prangnell P. Modelling Al3Zr dispersoid precipitation in multicomponent aluminium alloys. *Mater Sci Eng A*. 2003;352(1-2):240-250. doi:10.1016/S0921-5093(02)00894-8.

96. Li X, Starink MJ. Analysis of Precipitation and Dissolution in Overaged 7xxx Aluminium Alloys Using DSC. *Mater Sci Forum*. 2000;331:1071-1076.

97. Kamp N, Sinclair I, Starink MJ. Toughness-Strength Relations in the Overaged 7449 Al-Based Alloy. *Metall Mater Trans A*. 2002;33(April).

98. Morris AJ, Robey RF, Couch PD, De los Rios E. A Comparison of the Damage Tolerance of 7010 T7451 and 7050 T7451. *Mater Sci Forum*. 1997;242:181-186. doi:10.4028/www.scientific.net/MSF.242.181.

99. Deschamps A, Brechet Y. Nature and distribution of quench-induced precipitation in an Al-Zn-Mg-Cu alloy. *Scr Mater*. 1998;39(11):1517-1522.

100. Tanner DA, Robinson JS. Residual stress prediction and determination in 7010 aluminum alloy forgings. *Exp Mech*. 2000;40(1):75-82. doi:10.1007/BF02327551.

101. Shu WX, Hou LG, Zhang C, et al. Tailored Mg and Cu contents affecting the microstructures and mechanical properties of high-strength Al-Zn-Mg-Cu alloys. *Mater Sci Eng A*. 2016;657:269-283. doi:10.1016/j.msea.2016.01.039.

102. Sun Y. et al. unpublished work (2016).

103. Liao Y G, Han X Q, Zeng M X, Jin M. Influence of Cu on microstructure and tensile properties of 7XXX series aluminum alloy. *Mater Des*. 2015;66(PB):581-586. doi:10.1016/j.matdes.2014.05.003.

104. Wang M, Lu MS. *Handbook of Light Metal Material Processing: Part I*. Metallurgical Industry Press, Beijing, China; 1979.

105. Archambault P, Godard D. High temperature precipitation kinetics and TTT curve of a 7xxx alloy by in-situ electrical resistivity measurements and differential calorimetry. *Scr Mater*. 2000;42(7):675-680. doi:10.1016/S1359-6462(99)00419-4.

106. Zhang YH, Yang SC, Ji HZ. Microstructure evolution in cooling process of Al-Zn-Mg-Cu alloy and kinetics description. *Trans Nonferrous Met Soc China (English Ed*. 2012;22(9):2087-2091. doi:10.1016/S1003-6326(11)61432-5.

107. Robson JD. Microstructural evolution in aluminium alloy 7050 during processing. *Mater Sci Eng A*. 2004;382(1-2):112-121. doi:10.1016/j.msea.2004.05.006.

108. McQueen HJ, Celliers OC. Application of hot workability studies to extrusion processing. Part III: Physical and mechanical metallurgy of Al-Mg-Si and Al-Zn-Mg alloys. *Can Metall Q*. 1997;36(2):73-86. doi:10.1016/S0008-4433(97)00003-7.

109. Zhang Y, Milkereit B, Kessler O, Schick C, Rometsch PA. Development of continuous cooling precipitation diagrams for aluminium alloys AA7150 and AA7020. *J Alloys Compd*. 2014;584:581-589. doi:10.1016/j.jallcom.2013.09.014.

110. Tanner DA, Robinson JS. Reducing residual stress in 2014 aluminium alloy die forgings. *Mater Des*. 2008;29(7):1489-1496. doi:10.1016/j.matdes.2007.07.002.

111. Brooks JA, Baskes MI, Greulich FA. Solidification modeling and solid-state transformations in high-energy density stainless steel welds. *Metall Trans A*. 1991;22(4):915-926. doi:10.1007/BF02659001.

112. Lippard HE, Campbell CE, Dravid VP, et al. Microsegregation behavior during solidification and homogenization of AerMet100 steel. *Metall Mater Trans B*. 1998;29(1):205-210. doi:10.1007/s11663-998-0023-0.

113. Juric D, Tryggvason G. A Front-Tracking Method for Dendritic Solidification. *J Comput Phys*. 1996;123(1):127-148. doi:10.1006/jcph.1996.0011.

114. Neumann L, Kopp R, Ludwig a, et al. Simulation of casting, homogenization, and hot rolling: consecutive process and microstructure modelling for aluminium sheet production. *Model Simul Mater Sci Eng*. 2004;12(1):S19-S31. doi:10.1088/0965-0393/12/1/S02.

115. Tin S, Lee PD, Kermanpur A, Rist M, McLean M. Integrated modeling for the. manufacture of Ni-based superalloy discs from solidification to final heat treatment. *Metall Mater Trans A*. 2005;36A(9):2493-2504. doi:10.1007/s11661-005-0123-2.

116. Bird RB, Stewart WE, Lightfoot EN. *Transport Phenomena*. 2nd ed. John Wiley & Sons, Inc.; 1960.

117. Hui YH. *Handbook of Food Science, Technology, and Engineering*. Vol 149. CRC press; 2006.

118. Jensrud O. High Strength Aluminium Alloys Extrusions - A Review of the Thermo-Mechanical-Process in High Performance Profile Manufacturing. *Key Eng Mater*. 2011;491:11-18. doi:10.4028/www.scientific.net/KEM.491.11.

119. Knipling KE, Karnesky RA, Lee CP, Dunand DC, Seidman DN. Precipitation evolution in Al-0.1Sc, Al-0.1Zr and Al-0.1Sc-0.1Zr (at.%) alloys during isochronal aging. *Acta Mater*. 2010;58(15):5184-5195. doi:10.1016/j.actamat.2010.05.054.

120. Ji Y-L, Zhang W, Chen X-Y, Li J-G. Increasing Solidification Rate of M2 High-Speed Steel Ingot by Fusible Metal Mold. *Acta Metall Sin (English Lett*. 2016;29(4):382-387. doi:10.1007/s40195-016-0398-x.

121. Locker LD, Capio CD. Reaction kinetics of tungsten thin films on silicon (100) surfaces. *J Appl Phys*. 1973;44(10):4366-4369. doi:10.1063/1.1661965.

122. Doherty RD, Ferrante M, Chen YH. On the growth kinetics of plate-shaped precipitates. *Scr Metall*. 1978;12(3):885-891.

123. Wang W, Murray JL, Hu SY, Chen LQ, Weiland H. Modeling of Plate-like Precipitates in Aluminum Alloys—Comparison between Phase Field and Cellular Automaton Methods. *J Phase Equilibria Diffus*. 2007;28(3):258-264. doi:10.1007/s11669-007-9021-1.

124. Rudman M. A volume-tracking method for incompressible multifluid flows with large density variations. *Int J Numer Methods Fluids*. 1998;28(2):357-378. doi:10.1002/(SICI)1097-0363(19980815)28:2<357::AID-FLD750>3.0.CO;2-D.

125. Rider WJ, Kothe DB. Reconstructing Volume Tracking. *J Comput Phys*. 1998;141(2):112-152. doi:10.1006/jcph.1998.5906.

126. Shao R, Krane M, Trumble K. Infiltration and directional solidification of CMSX-4 through a particulate ceramic preform. *Metall Mater …*. 2005;36(September):2461-2469. doi:10.1007/s11661-005-0120-5.

127. Zhang S, Krane MJM, Johnson DR. Effects of Geometric Constraint on Solidification Microstructural Development of Peritectic TiAl Alloys. *Mater Sci Forum*. 2014;783-786:1147-1152. doi:10.4028/www.scientific.net/MSF.783-786.1147.

128. Wolverton C. Crystal structure and stability of complex precipitate phases in Al-Cu-Mg-(Si) and Al-Zn-Mg alloys. *Acta Mater*. 2001;49(16):3129-3142. doi:10.1016/S1359-6454(01)00229-4.

129. Wang SC, Starink MJ. Precipitates and intermetallic phases in precipitation hardening Al–Cu–Mg–(Li) based alloys. *Int Mater Rev*. 2005;50(4):193-215. doi:10.1179/174328005X14357.

130. Dubost B, Audier M, Jeanmart P, Lang J, Sainfort P. Structure of stable intemetallic compounds in the Al-Li-Cu-(Mg) and Al-Li-Zn-(Cu) systems. *J Phys Colloq*. 1987;48(C3):497-504.

APPENDIX

APPENDIX A

Diffusion Coefficients

Table A.1: Diffusion constant (D_o) and activation energy (Q_d) in equation (2.11) for elements in the α-Al matrix in the presence of other elements for Al-Si-Mg-Fe-Mn alloy system.

	D_0(m^2/s)	Q_d(kJ/mole)		D_0(m^2/s)	Q_d(kJ/mole)
D_{SiSi}^{Al}	1.4×10^{-5}	118	D_{FeSi}^{Al}	-2.6×10^{-7}	137
D_{SiMg}^{Al}	-6.1×10^{-8}	109	D_{FeMg}^{Al}	-5.3×10^{-12}	68
D_{SiFe}^{Al}	-1.7×10^{-7}	106	D_{FeFe}^{Al}	2.7×10^{-1}	213
D_{SiMn}^{Al}	-2.5×10^{-7}	109	D_{FeMn}^{Al}	6.8×10^{-14}	46
D_{MgSi}^{Al}	-1.3×10^{-7}	114	D_{MnSi}^{Al}	-8.6×10^{-9}	118
D_{MgMg}^{Al}	2.1×10^{-5}	121	D_{MnMg}^{Al}	-7.2×10^{-9}	118
D_{MgFe}^{Al}	5.4×10^{-7}	113	D_{MnFe}^{Al}	1.1×10^{-9}	111
D_{MgMn}^{Al}	8.1×10^{-7}	113	D_{MnMn}^{Al}	2.6×10^{-3}	199

Table A.2: Diffusion constant (D_o) and activation energy (Q_d) in equation (2.11) for elements in the α-Al matrix in the presence of other elements for Al-Zn-Cu-Mg-Zr alloy system.

	D_0(m^2/s)	Q_d(kJ/mole)		D_0(m^2/s)	Q_d(kJ/mole)
D_{ZnZn}^{Al}	1.2×10^{-5}	116	D_{MgZn}^{Al}	-2.1×10^{-6}	118
D_{ZnCu}^{Al}	-2.7×10^{-10}	102	D_{MgCu}^{Al}	1.8×10^{-6}	123
D_{ZnMg}^{Al}	-9.1×10^{-9}	110	D_{MgMg}^{Al}	2.5×10^{-5}	120
D_{ZnZr}^{Al}	-1.2×10^{-8}	108	D_{MgZr}^{Al}	1.6×10^{-5}	119
D_{CuZn}^{Al}	-6.2×10^{-7}	120	D_{ZrZn}^{Al}	-6.2×10^{-18}	114
D_{CuCu}^{Al}	3.6×10^{-5}	135	D_{ZrCu}^{Al}	-6.8×10^{-17}	142
D_{CuMg}^{Al}	-3.7×10^{-7}	120	D_{ZrMg}^{Al}	-1.8×10^{-17}	119
D_{CuZr}^{Al}	1.34×10^{-5}	135	D_{ZrZr}^{Al}	4.7×10^{-9}	115

APPENDIX B

List of abbreviations for phases

Table B.1: List of used phase abbreviations for Al-Si-Mg-Fe-Mn alloy system.

Phase	Formula	Crystal structure[63]
α-Al(Fe,Mn)Si	$Al_{12}(FeMn)_3Si$, $Al_{12}(FeMn)_3Si$	cubic
β-AlFeSi	Al_5FeSi, $Al_{4.5}FeSi$	monoclinic
β'	Mg_2Si	monoclinic

Table B.2: List of used phases abbreviations for Al-Zn-Cu-Mg-Zr alloy system.

Phases	Formula	Crystal structure[128–130]
η/M	$MgZn_2$	orthorhombic
η'	$MgZn_2$ (precursor of η)	orthorhombic
S	Al_2CuMg	orthorhombic
S’	Al_2CuMg (precursor of S)	orthorhombic
T	$Al_2Mg_3Zn_3$, $Mg_{32}(Al,Cu,Zn)_{49}$	cubic
V/Z	$Mg_2Zn_{11} + Al_5Cu_6Mg_2$	hexagonal
Θ	Al_2Cu	tetragonal

VITA

VITA

Pikee Priya

Graduate School, Purdue University

Pikee Priya was born in Deoghar, India and lived with her parents, brother and sister until secondary school after which she joined senior secondary school at DAV Jawahar Vidya Mandir in Ranchi. She graduated from DAV in 2001. She started her engineering studies at National Institute of Technology, Jamshedpur from which she graduated in year 2006. She was awarded an Alumni Gold Medal for her academic performance. She worked for a software firm as a Programmer Analyst after which she returned to academia for her Master's in 2009. She had an all India Graduate Aptitude Test in Engineering ranking of 1 in Metallurgical engineering. She worked on first principle Density Functional Theory calculations for her Master's Thesis. She started school at Purdue University under Prof. Matthew Krane and Prof. David Johnson in Spring, 2012 where she worked on meso-scale microstructural modeling, heat treatment experiments and microstructural characterization.